Review Article

ADVANCED PHOTONICS

Quantum sensing with spin defects: principles, progress, and prospects for use cases

Kihwan Kim,[a,†] Jong Sung Moon,[b,c,†] Dongkwon Lee,[a,†] Jin Hee Lee,[b] Yuhan Lee,[a] Chanhu Park,[a] Jugyeong Chung,[a] Donghun Lee,[a,*] and Je-Hyung Kim[b,*]

[a]Korea University, Department of Physics, Seoul, Republic of Korea
[b]Ulsan National Institute of Science and Technology (UNIST), Department of Physics, Ulsan, Republic of Korea
[c]Electronics and Telecommunications Research Institute, Quantum Technology Research Division, Daejeon, Republic of Korea

Abstract. Quantum sensing aims to detect signals with unparalleled sensitivity, potentially surpassing classical limitations. Solid-state spin defects, particularly nitrogen-vacancy centers in diamond, have emerged as promising platforms due to their long coherence time, optical addressability, high field sensitivity, and spatial and spectral resolution, making them ideal for sensing and imaging applications. Their compact size and robust performance under room temperature and ambient conditions further enhance their suitability for real-world applications. We provide an overview of quantum sensing principles and explore efforts to improve sensor functionality, including advanced sensing protocols, spatial imaging techniques, and integration with optical systems to enhance detection efficiency. We also highlight recent progress in the applications of these sensors across various use cases, including biomedical diagnostics, semiconductor device inspection, and industrial and military applications.

Keywords: quantum sensing; quantum defects; quantum imaging; spin qubits; quantum materials.

Received May 9, 2025; revised manuscript received Jul. 23, 2025; accepted for publication Aug. 14, 2025; published online Sep. 24, 2025.

[DOI: 10.1117/1.AP.7.6.064002]

1 Introduction

Quantum sensing is a cutting-edge technology that leverages quantum properties, such as quantum coherence, superposition, and entanglement, to detect minuscule signals that are challenging to measure with classical counterparts. This technology enables the detection of physical parameters, such as magnetic fields, temperature, pressure, and gravity, with exceptional sensitivity and precision, surpassing classical limits.[1,2]

Among the various quantum sensing platforms, solid-state spin defects have emerged as a promising candidate due to their long spin coherence, compatibility with optical and microwave (MW) control, and ability to operate under ambient conditions.[3] The nitrogen-vacancy (NV) center in diamond, one of the most extensively studied spin defects, was first observed in 1965 and further investigated in the late 1970s through electron paramagnetic resonance studies.[4,5] Groundbreaking research in the early 2000s demonstrated optical initialization and readout of the NV's spin states, highlighting its potential as both a defect-based qubit and a sensitive quantum sensor.[6] Since then, a variety of spin defects in diverse host materials, such as silicon carbide (SiC), hexagonal boron nitride (hBN), gallium nitride (GaN), and silicon (Si), have been thoroughly explored,[7,8] each offering unique advantages for quantum sensing applications.

Unlike cold atom and superconducting qubits, which often require cryogenic temperatures or vacuum environments,[9,10] spin defects in wide-bandgap hosting materials, such as NV centers in diamond, operate robustly at room temperature and ambient conditions, facilitating practical and compact sensor implementations.[11,12] The combination of high field sensitivity and atomic-scale sensor size makes them ideal for high-precision magnetometry[13,14] and nanoscale imaging of temperature, magnetic, electric, and strain fields.[15,16] Furthermore, the advancements in crystal growth, ion implantation, optical manipulation, and device integration technologies have significantly improved the performance of the spin defects, rapidly expanding their potential for practical applications.

*Address all correspondence to Donghun Lee, donghun@korea.ac.kr; Je-Hyung Kim, jehyungkim@unist.ac.kr

†These authors contributed equally to this work.

Although previous reviews have introduced defect-based quantum materials, sensing principles, and performance metrics,[3,17–19] a comprehensive overview of quantum sensing based on spin defects from fundamental quantum sensing science to technologies for real-world applications based on spin defects remains lacking. In this review, we provide an up-to-date perspective spanning diverse spin defect platforms, recent advances in quantum control and photonic engineering, and application-driven quantum sensors, as depicted in Fig. 1. In Sec. 2, we begin with the basic working principles of solid-state spin defects, with a particular focus on diamond NV centers. We then discuss various quantum sensing protocols, including optically detected magnetic resonance (ODMR) in continuous and pulsed control techniques, as well as advanced protocols leveraging quantum coherence and entanglement. In addition, we present two imaging techniques using spin defects: scanning probe and wide-field optical imaging methods. In Sec. 3, we introduce novel methods that integrate spin defects with various optical platforms, such as nanostructured devices, micro-lenses, and photonic cavities, to enhance optical readout efficiency and light–matter interaction. Finally, in Sec. 4, we highlight recent progress in applying these techniques to practical quantum sensors, bridging the gap between laboratory research and real-world applications across a range of fields, including biomedical diagnostics, semiconductor device inspection, industrial sensing, and aerospace and military applications.

2 Quantum Sensing and Imaging Protocols Based on Spin Defects

Solid-state defects offer several advantages for quantum sensing applications. The defect energy levels are located well within the wide bandgap of crystals, effectively decoupling them from the electrical band structures of the host materials, which helps maintain high coherence properties even within solid-state environments. The defects can also operate under practical conditions at room temperature without the need for vacuum systems. When combined with imaging techniques, they enable high-sensitivity and high-resolution mapping of various physical quantities, such as magnetic, electric, and strain fields. In addition, the electronic spin states of these defects can be initialized, manipulated, and detected optically via fluorescence,[20] making integration with optical platforms an attractive option for enhanced readout and versatile control of the spin states. The optical transitions manifest in the color of the host crystals, and the defects are often referred to as "color centers," as shown in Fig. 2.

In this section, we begin with a brief overview of the fundamental working principles of quantum sensors based on color centers, focusing on how their spin states interact with external optical and MW fields. We then explore various sensing protocols aimed at enhancing sensing performance. In addition, we discuss scanning and wide-field optical techniques that enable spatially resolved imaging implementations of these sensors. Finally, we compare a range of quantum materials that host different color centers, highlighting their distinct optical and spin properties.

2.1 Basics of Spin Defects

Here, we discuss the basics of spin defects, with a particular focus on diamond NV centers. The NV center has been extensively studied in the field of quantum sensing due to its high sensitivity on a wide range of physical quantities, including temperature,[21–28] stress/strain,[29–31] electric field/charge,[32–34] magnetic

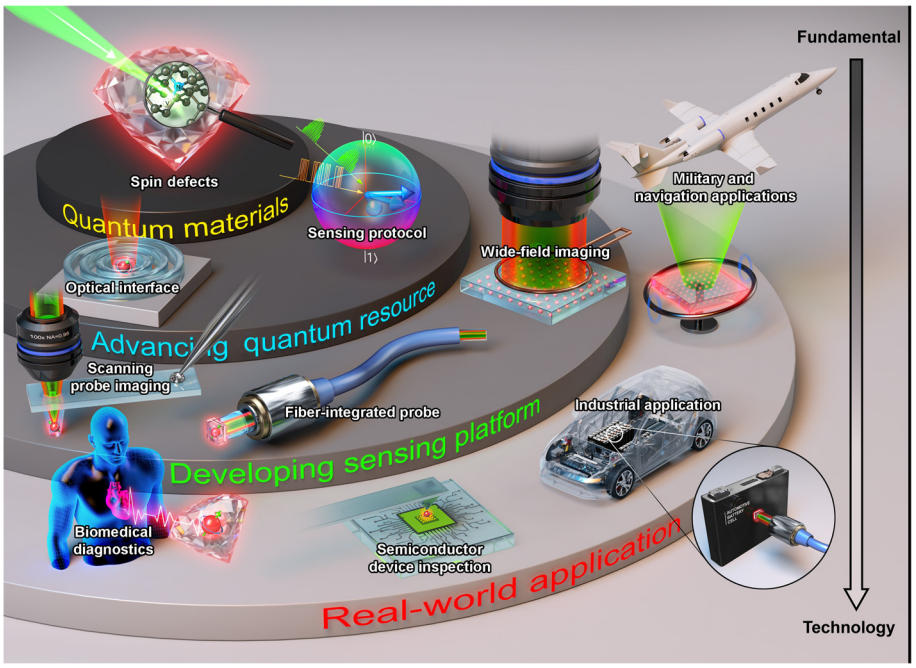

Fig. 1 Overview of this review: the quantum sensing landscape using spin defects, tracing the progression from fundamental research to technological developments aimed at enabling real-world applications. A directional bar is included to illustrate this trajectory—from foundational studies to advanced technological implementations—highlighting the increasing complexity and maturity of each stage.

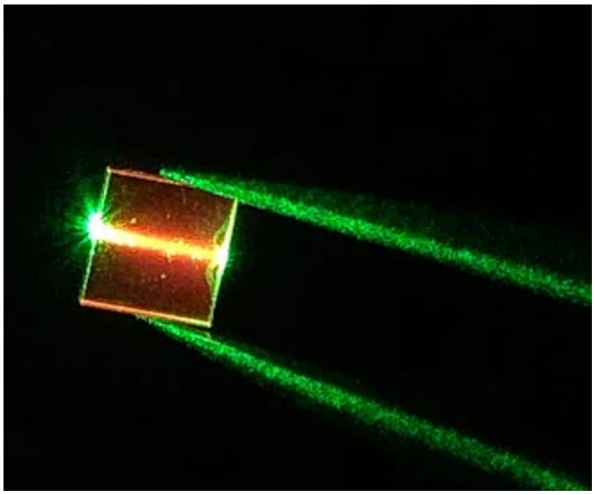

Fig. 2 Example of a fluorescence image of the color centers. When ensemble NV centers in diamond are illuminated by a green laser at 532 nm, they emit red fluorescence around 620 to 800 nm.

field,[35–62] pressure,[63] and rotation (using its intrinsic nuclear spin resource),[64–67] across a broad range of temperatures (mK to 1000 K)[68–71] and pressures (up to hundreds of GPa).[63,72–76] A detailed summary of the NV center Hamiltonian, coupling coefficients, and typical sensitivities for these physical properties is available in Ref. 77.

2.1.1 Electronic structures of the diamond NV center

The NV center consists of three carbon atoms, a nitrogen substitutional atom, and a vacancy within a diamond lattice. A total of six electrons (three from the carbon atoms, two from the nitrogen atom, and one from the host materials' electronic bands) occupy the ground energy levels of the NV center. Two unpaired electrons at the highest energy levels form an $S = 1$ spin system, with sub-spin states of $m_s = 0$, $m_s = -1$, and $m_s = +1$. In the presence of an external magnetic field, $\vec{B}$, the NV Hamiltonian can be written as follows ($\hbar = 1$):

$$H = DS_z^2 + \gamma_{\mathrm{NV}}\vec{B}\cdot\hat{S}, \tag{1}$$

where D is the zero-field splitting (ZFS), γ_{NV} is the NV's gyragnetic ratio (2.803 MHz/G),[78] and $\hat{S}$ is the electron spin operator of the NV center.

In the ground state, the ZFS between $m_s = 0$ and the degenerated $m_s = \pm 1$ states is 2.87 GHz at room temperature.[27] The ZFS varies with temperature at a rate of 75.0(6) kHz/K,[22] making the NV center suitable for sensitive thermometry. By contrast, the degenerated spin states $m_s = \pm 1$ can be split by the Zeeman effect in the presence of an external magnetic field. Monitoring the Zeeman splitting is the underlying mechanism of the NV magnetometry. Typically, one of the $m_s = \pm 1$ states is chosen to define a two-level system, and these states can act as a qubit. Therefore, developing techniques for properly reading out and manipulating these qubits is important in several quantum sensing protocols based on spin defects.

The energy levels and optical transitions associated with the NV center are illustrated in Fig. 3(a). Upon illumination with a green laser ($\lambda = 532$ nm), an electron in the $^3A_2$ ground electronic state is excited to the ^3E doublet state, followed by a rapid photon decay on the order of tens of nanoseconds.[79,80] The resulting fluorescence spans ~620–800 nm, with the zero-phonon line (ZPL) at 637 nm, and its intensity varies between the $m_s = 0$ (bright) and $m_s = \pm 1$ (dark) states due to the spin-selective intersystem crossing (ISC) and transition via metastable singlet states. During the optical transition, mixed ground spin states can also be initialized into the $m_s = 0$ state through the spin-flipping process. This unique property is the key to the spin-dependent optical readout and initialization of the spin qubit. Note that manipulation between the $m_s = 0$ and $m_s = \pm 1$ states is achieved by applying MW fields with a frequency that matches the spin transition energies.

2.1.2 Confocal fluorescence microscopy

As shown in Fig. 3(b), a confocal fluorescence microscope is commonly used to address single NV centers. The microscope consists of "confocal" optical components: an objective lens and an eyepiece lens (detector), with a pinhole acting as a spatial filter. In addition, a scanning system—either a scanning laser beam or a sample stage—is incorporated into the microscope to spatially map the fluorescence signals. The scanning confocal fluorescence microscope serves as a fundamental tool for characterizing the optical and spin properties of spin defects. An example confocal image of NV centers in Fig. 3(c) clearly shows individual NV centers. The identification of single NV centers can be further confirmed through $g^{(2)}(t)$ measurements.[81]

To improve the spatial resolution and photon collection efficiency of individual NV centers, an objective lens with a high numerical aperture (NA) is typically used. However, the high refractive index of diamond (2.42) results in reduced collection efficiency, which decreases the number of readout photons and sensitivity. In general, the shot-noise-limited sensitivity (η_{shot}) is related to the average photon number (N_{photon}) as follows:[82]

$$\eta_{\mathrm{shot}}(N_{\mathrm{photon}}) \propto \frac{1}{\sqrt{N_{\mathrm{photon}}}}. \tag{2}$$

Therefore, various efforts have been made to enhance collection efficiency by engineering optical interfaces or incorporating optical devices, which will be discussed in detail in Sec. 3.

2.1.3 Optically detected magnetic resonance

Once a single NV center is identified from the confocal image, the next step is to determine the spin energy levels through electron spin resonance (ESR) spectroscopy. This is achieved by continuously applying the green laser and MW fields while collecting fluorescence signals as a function of the MW frequency [Fig. 4(a)]. This technique is referred to as continuous wave ESR (CW-ESR) spectroscopy. Continuous laser excitation and fluorescence detection enable spin initialization to $m_s = 0$ and real-time readout of the spin states. When the MW frequency matches the NV center resonance, the NV center undergoes continuous Rabi oscillations. As the probability of the spin being in the $m_s = \pm 1$ states increases, the fluorescence intensity decreases, resulting in dark dips in the spectrum [Figs. 4(b) and 4(c)]. Without an applied DC magnetic field, the CW-ESR spectrum shows a single dip at the frequency of ZFS, i.e., 2.87 GHz at room temperature. However, when a DC magnetic field is applied, two split resonances appear, corresponding to the two transitions $m_s = 0 \leftrightarrow m_s = -1$ and $m_s = 0 \leftrightarrow m_s = +1$,

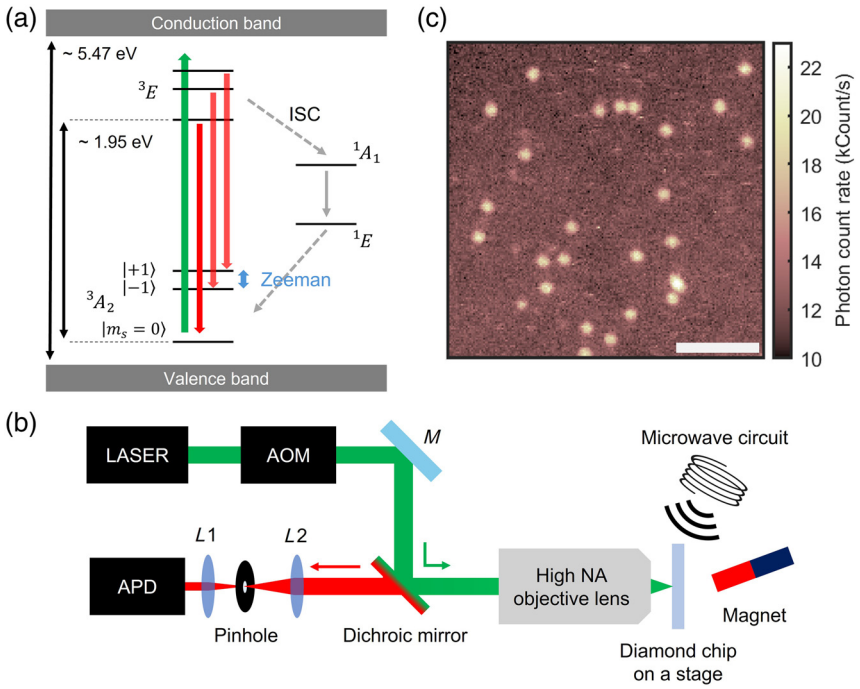

Fig. 3 Basics of NV center. (a) Schematic of NV's energy levels and optical transitions. The energy levels of the NV center reside within the bandgap (~5.47 eV) of diamond and are well separated from the diamond's conduction and valence bands. A green laser at $\lambda = 532$ nm excites the NV center from its electronic ground state ($^3A_2$) to the excited state (^3E). Subsequent optical decay produces broad fluorescence in the range of $\lambda \sim 620$ to 800 nm (ZPL: 637 nm). During the optical transitions, the NV center experiences a spin-dependent decay process through the ISC and metastable singlet states. As a result, the fluorescence intensity for $m_s = \pm 1$ is up to 30% lower than that of $m_s = 0$, enabling optical readout of the spin states. Moreover, the spin-flipping process that occurs during the optical transition allows initialization of the spin states into $m_s = 0$. (b) Schematic of a confocal fluorescence microscope typically used for the NV experiment. In the optical excitation path, a green laser, an acousto-optic modulator (AOM), a scannable mirror (M), a dichroic mirror, and a high numerical aperture (NA) objective lens are used to focus the laser onto a single NV center in a diamond plate. The resulting fluorescence is collected by the objective lens, with eyepiece lenses (L1 and L2) and a pinhole, and detected by an avalanche photodiode (APD). MW circuitry near the diamond plate provides MW fields for spin transitions. A permanent magnet is occasionally used to break the degeneracy of $m_s = \pm 1$ prior to sensing experiments. (c) An example of an NV fluorescence image obtained by the confocal setup in (b). Individual NV centers can be clearly identified in the image. The scale bar is 5 μm.

respectively. ESR spectroscopy through optical readout is referred to as ODMR.

2.2 Quantum Sensing Protocols

As shown in Figs. 4(b) and 4(c), ODMR spectroscopy offers the simplest method for DC magnetometry. However, continuous driving of laser and MW fields can induce power broadening, which reduces the signal contrast and increases the linewidth of ESR resonances, ultimately degrading sensitivity.[84] In this section, we discuss quantum sensing protocols based on both continuous wave and pulsed schemes of laser and MW fields. These protocols can be categorized into four different types: relaxometry, Rabi, Ramsey, and correlation protocols.

2.2.1 Relaxometry

Quantum coherence is a valuable resource in quantum sensing,[85,86] playing a crucial role in sensitivity.[82] Quantum coherence time can be categorized into two types: longitudinal (spin-lattice) relaxation time T_1 and transverse (spin-spin) relaxation time T_2. The T_1 time is governed by energy exchange processes between the spin and energy-matched levels in the surrounding environment, such as a thermal bath or spin bath.[87] Through these interactions, the spin dissipates energy, and the corresponding relaxation rate is determined by the strength of the interaction.

T_1 relaxometry utilizes changes in the T_1 time due to interactions with environmental noise, especially when the relevant energy scale matches the spin two levels, typically in the GHz range for spin defects. As the electron's precession frequency falls within this range, T_1 relaxometry has been used to probe GHz stochastic signals from ionic samples such as Gd^{3+}. Figure 5(a) illustrates the pulse sequences used for NV's T_1 relaxometry. The NV center is initialized and prepared in a specific state (e.g., the excited state $|1\rangle$) using laser and/or MW pulses. Note that we assume that after initialization, the qubit is prepared in its ground state, taking into account the depopulation from the metastable state. After a finite evolution time τ, qubit readout is

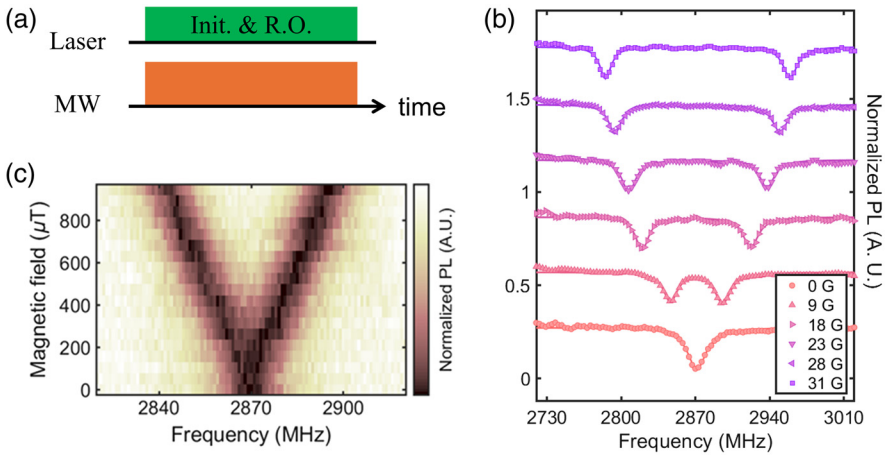

Fig. 4 ODMR spectroscopy. (a) Continuous laser and MW excitations for ODMR spectroscopy. "Init." and "R.O." refer to the initialization and readout of the spin qubit. (b) ODMR spectra with varying magnitudes of the DC magnetic field. Normalized photoluminescence (PL) is plotted as a function of MW frequency. The plots are offset for clarity. (c) Two-dimensional (2D) intensity map of the ODMR spectra. The amount of frequency splitting, i.e., Zeeman splitting, is used to detect DC magnetic fields that are parallel to the NV center axis in the low field regime. Panel (c) is adapted with permission from Ref. 83; © 2020 The Authors.

performed with a laser pulse. By repeating the procedure with varying τ, the NV's photoluminescence (or contrast) is plotted as a function of τ, and the T_1 time is obtained from the decay constant.

2.2.2 Rabi-type sensing protocols

Although T_1 relaxometry measures changes in the T_1 time due to interactions with stochastic signals or noise at the spin resonance frequency, the Rabi protocol measures changes in the rate of population inversion between the ground state $|0\rangle$ and excited state $|1\rangle$ due to coherent driving at the spin resonance frequency. Figure 5(b) illustrates the pulse sequence and the resulting Rabi oscillations. After initialization, the qubit undergoes coherent transitions between $|0\rangle$ and $|1\rangle$ due to continuous MW. The magnitude of the MW field determines the oscillation period, known as the Rabi frequency. Changes in the Rabi frequency due to external coherent signals are used to detect GHz AC signals.[88,89]

The Rabi frequency Ω_{AC}, which varies according to the amplitude of the AC signal, can be calculated using the following equation:

$$P_{|0\rangle\to|1\rangle} = \frac{\Omega_{\mathrm{AC}}^2}{\Omega_{\mathrm{AC}}^2+\delta^2}\sin^2\left(\frac{\sqrt{\Omega_{\mathrm{AC}}^2+\delta^2}}{2}t\right), \tag{3}$$

where $P_{|0\rangle\to|1\rangle}$ is the transition probability between $|0\rangle$ and $|1\rangle$ after time t, and δ is the detuning, the difference between the spin resonance frequency ω_{q} and the AC signal frequency ω_{AC}.

Sometimes, pulsed and continuous protocols are distinguished by whether the qubit undergoes free evolution between initialization and readout. Although the Rabi protocol uses pulsed MWs, it can be classified as a continuous driving protocol because the qubit is continuously driven during the evolution period. Continuous MW driving, as used in the Rabi-type protocol, offers several advantages over pulse-based protocols. For instance, Rabi-type magnetometry has been demonstrated using continuous dynamical decoupling (CDD) methods.[90–94] CDD enables tunable control over the spin transition energy by transforming the bare spin states into dressed states, serving as an effective noise filter to suppress background noise outside the dressed state's frequency. This approach allows for wide-bandwidth AC magnetometry with improved sensitivity. Note that typical CDD protocols resemble Rabi-type protocols when detecting coherent signals, whereas for randomly phased, incoherent signals, they become more like relaxometry techniques.

Recently, more advanced CDD methods have been developed. For example, concatenated CDD has successfully demonstrated prolonged coherence time, reduced noise floors, and extended spectral ranges toward both low-frequency (sub-MHz)[95] and high-frequency (GHz) regimes.[96] In addition, a phase-modulated CDD technique, known as phase-modulated Hartmann–Hahn double resonance, has demonstrated a four-order power reduction, resulting in spectral narrowing.[97] Although pulse-based sensing protocols are still predominantly used in quantum sensing experiments, the Rabi-type protocol is emerging as a promising alternative methodology for quantum sensing.

2.2.3 Ramsey-type sensing protocols

Ramsey interferometry is the most basic pulse-based sensing protocol for detecting DC and low-frequency magnetic signals (typically less than tens of kHz). Its sensitivity is fundamentally limited by the T_2 time; however, due to non-zero inhomogeneous low-frequency noise, the sensitivity is instead determined by the effective T_2 time, known as T_2^*. Figure 5(c) illustrates the pulse sequence and an example result of Ramsey interferometry. After initialization, the spin qubit is transformed into a maximally superposed state of $|0\rangle$ and $|1\rangle$, e.g., $(|0\rangle+|1\rangle)/\sqrt{2}$, with a $\pi/2$ pulse. During the free evolution period τ, the qubit acquires a spin-dependent phase, resulting in a phase difference given by

$$\phi(\tau) = \int_0^\tau \Delta m_{\mathrm{s}}\gamma_{\mathrm{NV}}B_z(t)\mathrm{d}t, \tag{4}$$

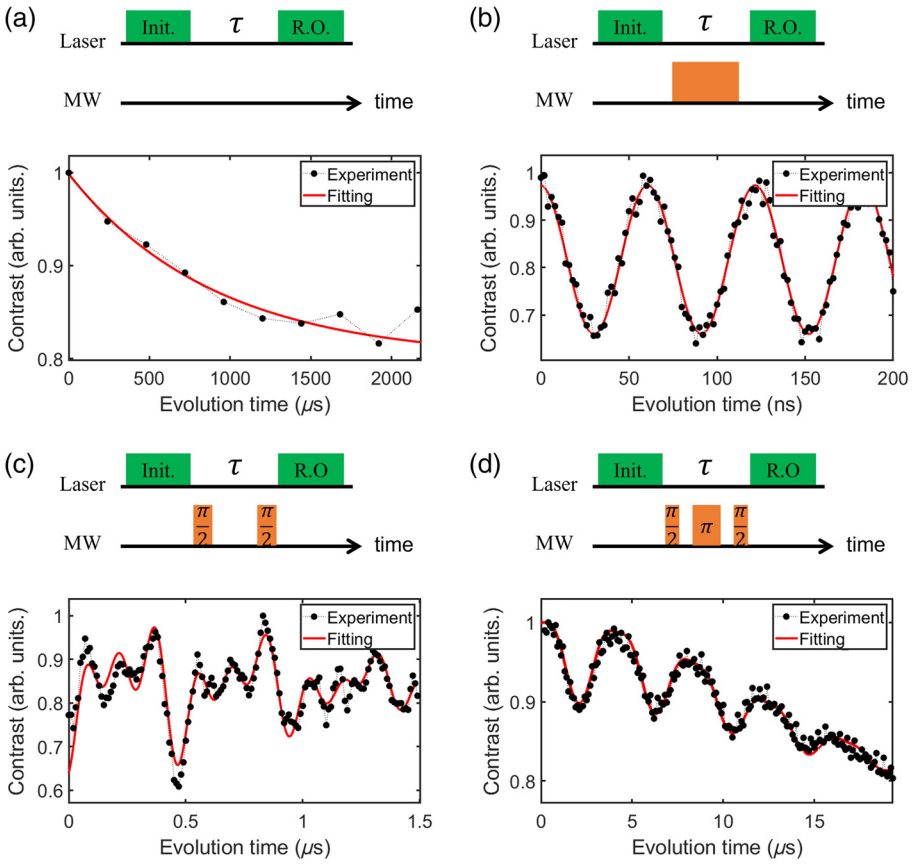

Fig. 5 Basic quantum sensing protocols with diamond NV centers. Laser and MW pulse sequences and measurement results for (a) T_1 relaxometry, (b) Rabi oscillation, (c) Ramsey interferometry, and (d) spin Hahn echo. "Init." and "R.O." refer to qubit initialization and readout. We assume that after initialization, the qubit is prepared in its ground state, taking into account the depopulation from the metastable state. The evolution time τ corresponds to the time interval between the "Init." and "R.O." pulses. (b) A continuous MW field is applied, and the oscillation frequency corresponds to the Rabi frequency. (c) The oscillations in Ramsey measurement are related to the NV's hyperfine triplet, which arises from the interaction with the ^{14}N nuclear spin. (d) The periodic contrast suppressions occur at the Larmor frequency of the ^{13}C nuclear spin bath and its higher-frequency replicas.

where Δm_s is the difference in the magnetic quantum number between the superposed states, and $B_z(t)$ is the magnetic field along the z-axis (i.e., spin's quantization axis). After the free evolution period, a second $\pi/2$ pulse is applied to project the accumulated phase difference into a population difference, which is then measured by the readout pulse.

Although Ramsey interferometry is sensitive to detecting phase differences induced by DC signals, adding additional π pulses in between the Ramsey sequence enables the detection of AC signals up to several tens of MHz. These pulse-based sensing protocols are known as pulsed dynamical decoupling (PDD) protocols. Figure 5(d) shows an example of the PDD protocol with a single π pulse,[98] known as the Hahn echo. The detection of AC magnetic signals from neighboring ^{13}C nuclear spins has been clearly demonstrated using the method [Fig. 5(d)]. Besides the Hahn echo, various PDD protocols have been developed by incorporating additional π pulses, including Carr–Purcell–Meiboom–Gill (CPMG), the XY family (XY4, XY8, etc.), and Knill dynamical decoupling. Each protocol is designed to address specific challenges, such as mitigating phase errors or pulse imperfections.[99–101] PDD protocols have become fundamental building blocks both for conventional and NV-based nuclear magnetic resonance (NMR) spectroscopy.[44–62]

The effects of π pulses can be understood through filter functions in the toggling frame. Without π pulses, as in Ramsey interferometry, the calculated filter function acts as a low-pass filter, allowing only DC and low-frequency signals to pass through. By contrast, π pulses create a band-pass filter, where the central frequency shifts toward higher frequencies, and the filter's bandwidth becomes narrower as the number of π pulses, N, increases, as depicted in Fig. 6(a). A higher central frequency and a narrower bandwidth enable the detection of AC signals, protect the qubit from band-mismatched noise, enhance coherence time, and improve both spectral resolution and sensitivity [Fig. 6(b)].[13,35,102–104] However, the performance is limited by the Rabi frequency (or the pulse width) and the T_2 time (which itself is limited to $T_2 \approx 2T_1$). As a result, the highest AC frequency detectable using PDD protocols is typically limited to several tens of MHz. For AC sensing at higher frequencies

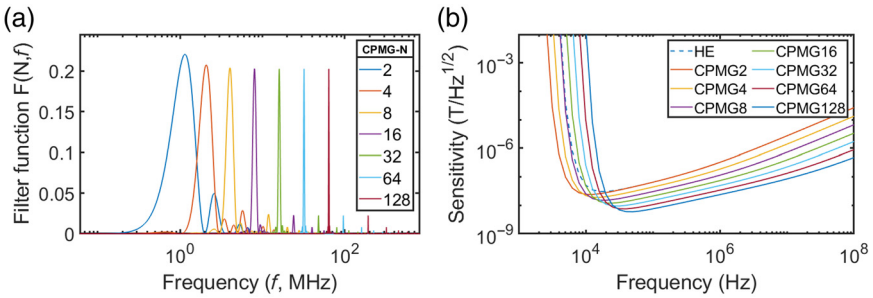

Fig. 6 Performance of PDD with π pulses. (a) Noise filter functions of the CPMG-N protocol for a 1 μs sensing time. N denotes the number of π pulses. As N increases, the filter band shifts to higher frequencies, and the bandwidth becomes narrower. (b) Simulated magnetic field sensitivity to compare various PDD protocols. The calculations assume $T_2 = 100$ μs and an NV's ESR contrast of 0.3. In addition, it is assumed that the T_2 time of an N-pulse sequence is enhanced by a factor of $N^{2/3}$.

(~100 MHz to GHz), T_1 relaxometry and Rabi-type protocols can be used, as discussed previously.

Although PDD protocols are typically vulnerable to pulse errors, various mitigation methods have been developed over the decades. For instance, under the assumption of only 0th-order terms in average Hamiltonian theory,[99–101] the XY4 sequence is more robust to qubit rotation errors than the CPMG sequence. Pulse errors can also be mitigated by designing composite pulse sequences, such as the M. Levitt pulse and BB1, or by employing optimal control techniques.[105–107] To avoid inherent spurious effects caused by the symmetries of pulse sequences, appropriate pulse sequences can be selected, as each sequence exhibits a different spurious response. In addition, this issue can be fundamentally alleviated by utilizing correlation measurements or implementing pulse sequences with a correlated random phase scheme, which will be discussed in detail in Sec. 2.2.4.[108,109]

2.2.4 Correlation-type sensing protocols

In addition to sensitivity, spectral resolution is also an important metric, particularly for NMR spectroscopy. Spectral resolution is typically limited by the spin coherence, which is on the order of a few milliseconds. In this section, we discuss how this challenge has been addressed, focusing on two sensing protocols: correlation measurement and quantum heterodyne measurement.

The spectral resolution of a sensing protocol is closely related to sampling theory: the longer the sampling time, the better the spectral resolution. In basic PDD protocols, the sampling time is limited by the T_2 coherence time, which for NV centers is typically less than 1 ms, resulting in a spectral resolution worse than 1 kHz. In nano-NMR spectroscopy, this resolution is insufficient to resolve chemical shifts (which depend on the applied magnetic field and are on the order of Hz for hydrogen NMR under a few teslas) or J-couplings (also on the order of Hz). The primary approach to overcoming this limitation is to utilize the correlation of sequential measurements, which effectively extends the sampling time beyond the T_2 limit, enabling significantly higher spectral resolution.

For instance, time correlations between two sequential phase measurements have demonstrated extended spectral resolution limited by T_1,[54] which can be further enhanced with the quantum memory, as shown in Fig. 7. The phase information from the first sensing period is stored in the qubit population during the correlation time, which is related to T_1, and then correlated with the phase acquired from the second sensing period. The spectral resolution can be improved further by a few orders of magnitude through the use of a nuclear memory qubit, with T_1 time that is much longer than that of the electron sensing qubit.[54,110,111]

The correlation measurement can be further improved by synchronizing the sequential measurements with an external clock, a technique known as quantum heterodyne (Qdyne) measurements, or, equivalently, coherently averaged synchronized readout (CASR). These methods have demonstrated sub-Hz spectral resolution, limited by stability of the clock and coherence time of the sample.[52,112,113] Achieving sub-Hz resolution enables chemical shift-resolved NMR spectroscopy at relatively low magnetic fields (<1 T).

One of the challenges of conventional PDD techniques for NMR studies is their difficulty in operating under high magnetic fields (>1 T), as the nuclear Larmor frequency becomes too high for MW drives to track. This issue is critical in NMR spectroscopy because samples often require high magnetic fields to ensure long coherence time or high sample polarization. This challenge has been addressed by several methods, such as direct quantum memory access,[110,111,114] electron nuclear double resonance quantum heterodyne,[115] and amplitude-encoded radio-induced signal.[116]

Moreover, time correlation protocols, which have been used for a single NV (or a single group of ensemble NV centers), have recently been applied to spatial correlation measurements between more than two NV centers, demonstrating enhanced bandwidth and improved signal-to-noise ratio (SNR).[37–41]

2.3 Toward Quantum Advantage

One of the long-term goals of "quantum" sensing is to achieve quantum advantage over classical sensors by surpassing the standard quantum limit (SQL) of sensitivity or spectral resolution. Although many theoretical proposals exist to realize this advantage, only a few experimental demonstrations have been made in quantum sensing research based on solid-state spin defects. In this section, we focus on recent experimental demonstrations aimed at achieving this goal.

2.3.1 Weak measurement

Investigating the fast-varying dynamics of a sample is an important objective of quantum spin sensors. However, conventional

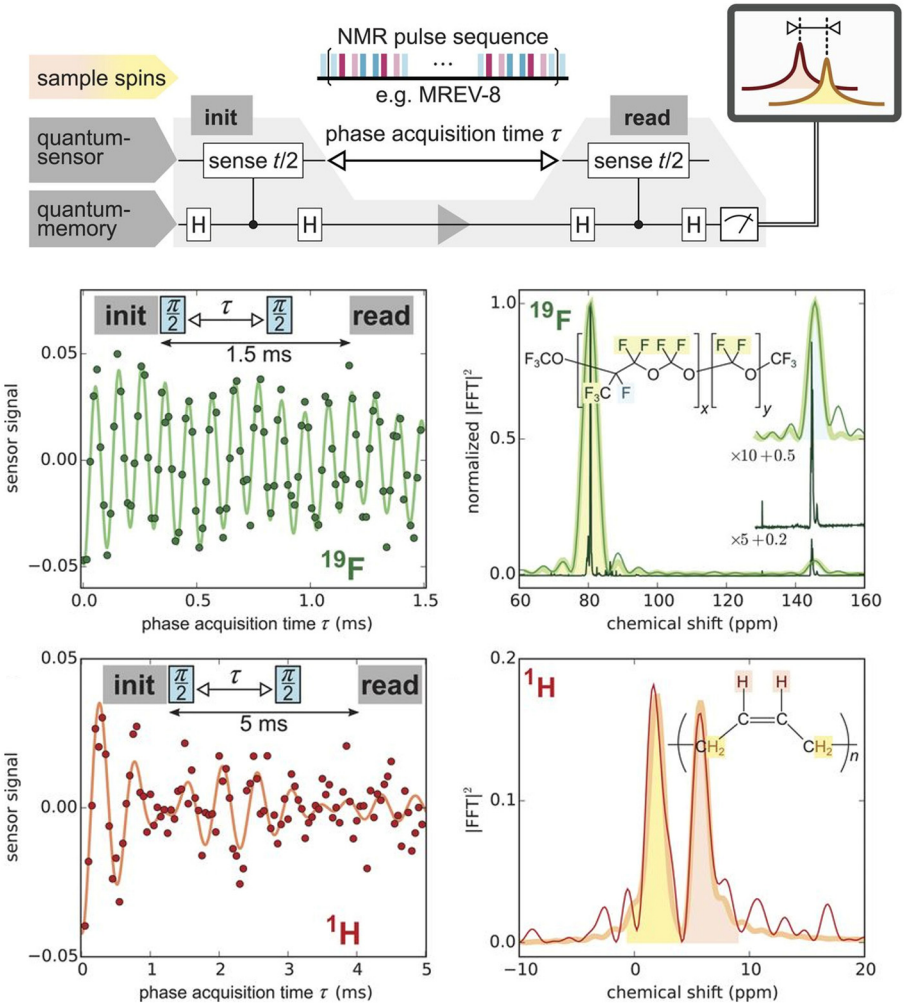

Fig. 7 Time correlation protocol for NMR spectroscopy. NV center (electron spin) serves as a sensing qubit, while a ^{14}N nuclear spin serves as a memory qubit. The MREV-8 NMR pulse can be used to reduce the spectral broadening from the sample dynamics. Chemical shifts of both ^{19}F and ^{1}H nuclear spins on the order of Hz are resolved with the quantum memory assisted correlation measurements. Images are adapted and modified with permission from Ref. 110; © 2017 The Authors, some rights reserved; exclusive licensee American Association for the Advancement of Science.

sensing protocols based on strong measurements inherently limit such studies by significantly perturbing the sample due to measurement backaction. By contrast, weak measurements harness the sequential detection of target dynamics using a weak probe. These relatively unperturbed measurements preserve the quantum properties of the target and allow for the tracking of nuclear spin dynamics, as illustrated in Fig. 8.[117] Similar to the Qdyne measurement, however, the spectral resolution of the weak measurement is also limited by the sampling time and the target sample's lifetime, resulting in a spectral linewidth on the order of Hz.

2.3.2 Quantum Fisher information scaling

Increasing the number of sensing qubits (N_{sensor}) or expanding the dimension of the Hilbert space is one of the most straightforward approaches to increasing sensitivity or quantum Fisher information.[118–123] Entangled sensing qubits can coherently accumulate signals, allowing the quantum Fisher information to scale proportionally to N_{sensor}^2, known as the Heisenberg scaling. By contrast, the Fisher information of classic sensors scales linearly with N_{sensor}, which is eventually limited by the SQL. With robust quantum memory,[124] it has been demonstrated that with an optimal phase mapping basis, the Fourier basis, the quantum Fisher information scales as $4^{N_{\text{sensor}}}$ (Fig. 9). This represents a state-of-the-art demonstration that combines quantum sensing and the quantum Fourier transform (QFT) technique, where the electron sensor detects the signal, and the nuclear memory spin stores and processes it. Note that additional energy levels in a larger spin system, known as a "qudit," can be advantageous, as demonstrated in Ref. 124. These extra levels enlarge the Hilbert space, which in principle leads to a more condensed quantum resource with a limited physical system. Furthermore, utilizing multiquantum coherence is expected to provide a quantum advantage,[82,125–130] benefiting from the large Hilbert space.

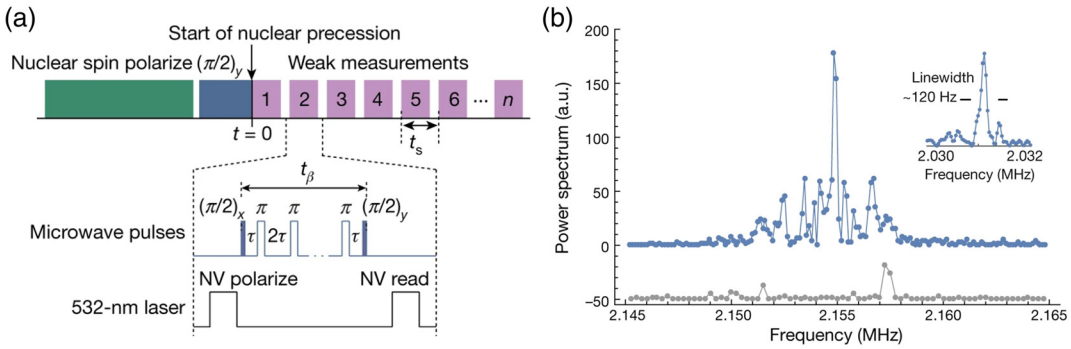

Fig. 8 Quantum sensing with the weak measurement. (a) Schematic of sequential weak measurements, which enable the tracking of nuclear spin dynamics. (b) An example NMR spectrum acquired using weak measurements, showing a single ^{13}C nuclear spin with ~120 Hz spectral resolution. Images are adapted with permission from Ref. 117; © 2019 The Authors, under exclusive license to Springer Nature Limited.

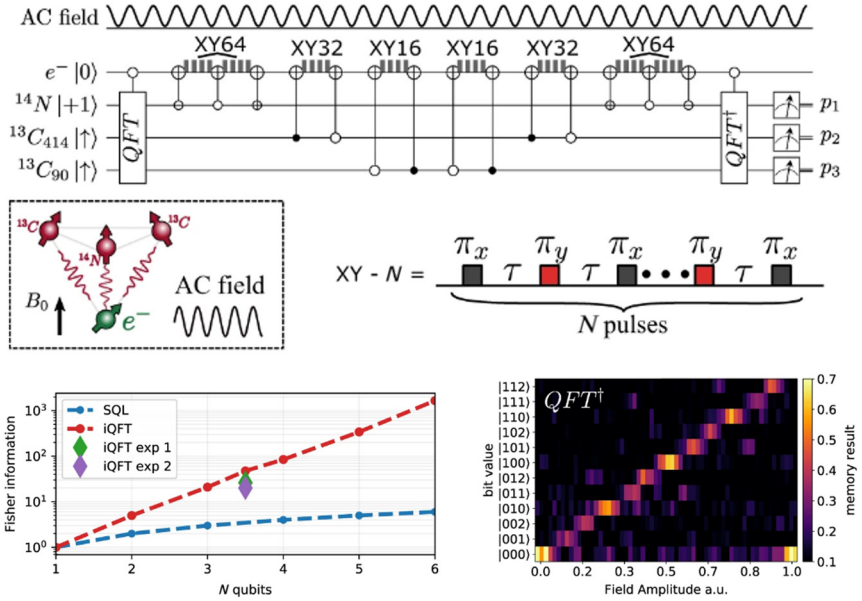

Fig. 9 Quantum phase estimation algorithm with QFT. A hybrid diamond quantum register is used to demonstrate beating the SQL. The register consists of an NV center as the sensor qubit and three nuclear spins as memory qubits. One of the nuclear spins is a spin triplet ($S = 1$), while the other two are spin doublet ($S = 1/2$), resulting in a total computational Hilbert space dimension of 12, corresponding to ~3.6-qubits system. In this experiment, the electron spin qubit "reads" the signal from the target and "writes" it to the nuclear memory qubits, where the quantum information is processed. Images are adapted and modified with permission from Ref. 124; © 2021 The Authors.

2.3.3 Entanglement-enabled noise filtering

A recent study[131] demonstrated that quantum entanglement can be leveraged to distinguish pure quantum signals from classical noise (Fig. 10). As previously discussed, typical sensing information is acquired in the form of the accumulated phase. In this study, the base protocol is a simple correlation measurement, where the phase information is lost due to the decoherence process. However, if the signal originates from a quantum target, the entanglement backaction maps information in the qubit population, allowing it to survive against the decoherence process and effectively filtering out the classical noises. Another example of a quantum filter has been demonstrated with higher-order correlation measurements,[132] which distinguishes quantum signals from classical ones by exploring the noncommuting nature of quantum signals. Similarly, other types of quantum correlations or quantum discord could serve as potential resources for quantum sensing.

2.4 Combination with Imaging Techniques

Solid-state spin defects can be integrated with imaging systems, extending the capabilities of quantum sensing to spatially

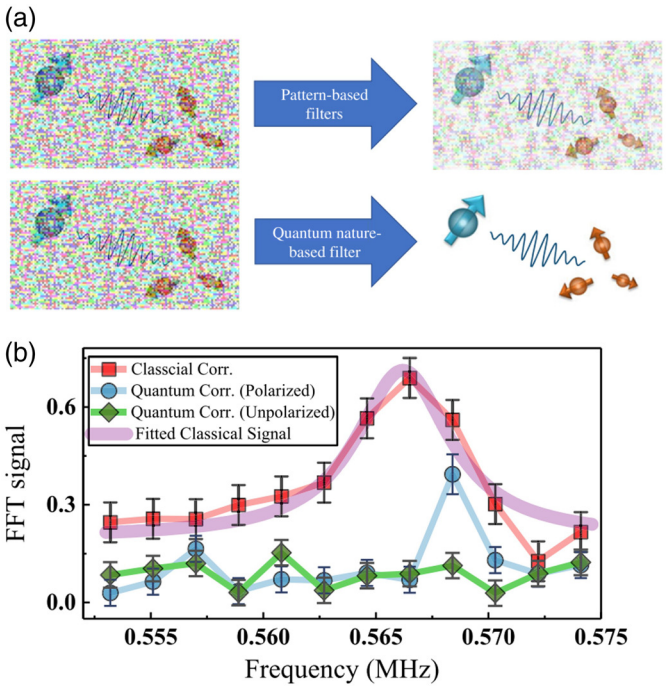

Fig. 10 Quantum filter based on entanglement. (a) Classical noise is filtered out due to the decoherence process, while quantum signals remain in the qubit population through entanglement backaction. (b) Demonstration of classical noise-free detection of quantum signals. Images are adapted with permission from Ref. 131; © 2023 American Physical Society.

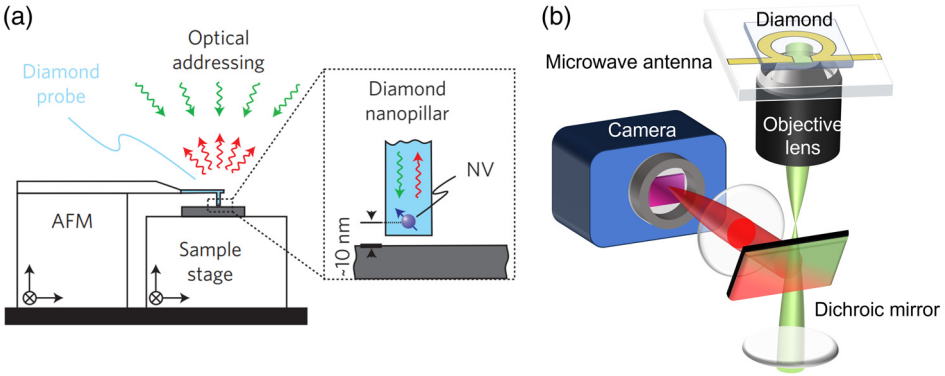

Fig. 11 Schematics of the two imaging techniques. (a) Schematic of single-spin scanning magnetometry. A single spin defect, e.g., NV center, is integrated at the tip of a fabricated diamond atomic force microscope (AFM). Confocal optics are employed to excite the NV center and collect the resulting fluorescence, while a sample beneath the AFM tip is scanned with the assistance of a three-dimensional scanning stage. Image is adapted with permission from Ref. 16; © 2012 Springer Nature Limited. (b) Schematic of wide-field quantum microscopy. Ensemble NV centers embedded in a diamond plate are used to detect magnetic fields from a sample on the diamond surface. Laser excitation occurs over the field-of-view of an objective lens, e.g., ~100 μm^2 to mm^2, and the fluorescence signals from the NV ensemble are captured using a photosensitive camera, such as a complementary metal oxide semiconductor (CMOS) camera.

resolved imaging. There are two main types of imaging based on spin defects: single-spin scanning magnetometry and wide-field quantum microscopy, as illustrated in Fig. 11. These imaging methods are applied to different target samples, depending on the required spatial resolution, imaging speed, and operating environments. For instance, single-spin scanning magnetometry has been used to study intriguing magnetic phenomena in condensed matter systems and to characterize current profiles in transport devices by providing high spatial resolution on the order of tens of nanometers.[133–136] This method offers high spatial resolution, but the overall slow scanning process limits the imaging time. By contrast, wide-field quantum microscopy has been used to image biological samples, magnetic materials, and current transport devices by providing imaging

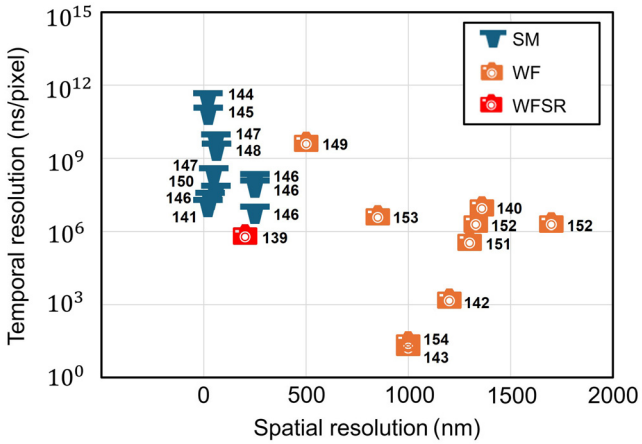

Fig. 12 Comparison of spatial and temporal resolutions for the two imaging methods: single-spin scanning magnetometry (SM) and wide-field quantum microscopy (WF). WFSR refers to wide-field imaging using super-resolution techniques. Although single-spin scanning magnetometry offers higher spatial resolution but lower temporal resolution (defined as the inverse of the pixel rate), wide-field quantum microscopy provides the opposite—lower spatial resolution but higher temporal resolution. The numbers assigned in the figure correspond to Refs. 139–154.

over a larger area with faster imaging speed but at the cost of reduced spatial resolution on the order of micrometers.[85,137,138] Although this method allows relatively fast imaging, the spatial resolution is limited by the diffraction limit of the excitation light rather than the size of the sensing qubit, i.e., spin defect.

Figure 12 compares the spatial resolution and temporal resolution of the two imaging methods. Given a fixed ability to extract information, there is an inherent trade-off between spatial and temporal resolutions. For example, super-resolution imaging techniques have been implemented in wide-field quantum microscopy, achieving higher spatial resolution at the cost of reduced temporal resolution. Xu et al.[139] used nine images to reconstruct a finer image for each pixel, resulting in a nine times slower imaging process. Conversely, pixel binning in an $n \times n$ configuration can enhance sensitivity and, consequently, temporal resolution while sacrificing spatial resolution.[140] Considering this relationship, the appropriate imaging technique should be selected based on the target sample and its dynamic properties.

2.4.1 Single-spin scanning magnetometry

Single-spin scanning magnetometry has been implemented for various magnetic materials and current transport devices, operating in environments from room temperature down to cryogenic temperatures. Figure 13 presents imaging examples of magnetic domain walls,[37] a single vortex in $YBa_2Cu_3O_{7-x}$ (YBCO) superconductor,[148] CrI_3 2D ferromagnets,[39] spin waves in yttrium iron garnet (YIG),[135] $BiFeO_3$ multiferroic materials,[150] current flows in graphene devices,[155] and super current in Josephson junctions.[156] This method has proven to be a powerful tool for investigating interesting magnetic phenomena in exotic materials, spintronics, magnonics, and transport devices.

In addition to the image applications, ongoing efforts are focused on enhancing its performance. For example, the atomic force microscope (AFM) tip with a parabolically designed diamond nanopillar has demonstrated improved photon collection efficiency and directionality of emitted photons, achieving saturation photon count rate of 2.1 million counts per second (Mcps).[157] Recently, the gradiometry technique has been introduced, which converts DC to AC magnetic fields by utilizing periodic driving of the AFM tip and the strong gradient of magnetic fields from the sample. This method enables the detection of DC signals using more sensitive AC sensing protocols.[158] Furthermore, the use of multiple NV centers for imaging has been proposed to improve sensitivity through correlated signal measurements.[159] These advancements continue to pave the way for further improvements and applications of defect-based scanning magnetometry.

2.4.2 Wide-field quantum microscopy

By replacing a single-point photodetector with a multipixel array camera, wide-field quantum microscopy enables the simultaneous acquisition of fluorescence signals from spatially distributed NV centers within the field of view. This provides the advantage of short imaging times (seconds to minutes) and large imaging areas (100 μm^2 to mm^2).[105,160,161]

Wide-field quantum microscopy has been applied to imaging magnetic materials, current transport devices, geological rocks, and biological samples. Particularly, the nontoxic and biofriendly nature of diamond makes this imaging method a powerful tool for studying cells, tissues, neurons, etc. Figure 14 illustrates imaging examples of magnetotactic bacteria,[162] Fe nanowires,[138] spin waves in YIG,[163] magnetized eucrite ALHA81001,[160] current flows in graphene ribbons,[149] and magnetic steganography.[164]

To improve diffraction-limited spatial resolution, super-resolution imaging techniques have been introduced. These include stochastic reconstruction microscopy,[165] structured light illumination microscopy,[139,166] aberration correction through image deconvolution with an applied point spread function,[167] and leveraging magnetic field phase changes under field gradients for super-resolution imaging.[168,169]

In addition, nanofabricated pillar arrays have been implemented to improve optical collection efficiency and increase photon signals.[170] For example, an improvement in sensitivity by ~5 times with nano-pillar arrays has been demonstrated.[170] Double-etched multicone structures have also been studied, narrowing the far-field angle and enabling coupling with low-NA objective lenses. These structures also improve spatial resolution due to the sharp apex of the pillar tips.[171] These advancements in photon collection over a wide imaging area promote increased SNR and faster imaging acquisition rates.

2.5 Emerging Materials and Defects for Quantum Sensing

Despite the advantages of NV centers in quantum sensing, their host material, diamond, presents several challenges, such as high cost, difficulties in growing large-sized single crystals, and challenges in nano-fabrication. In addition, the optical properties of NV centers, e.g., a small portion of ZPL and broad phonon sidebands, pose further barriers to their application and optical interfacing. To overcome these limitations, alternative types of defects and host materials have recently been explored through both theoretical and experimental research.

In diamonds, group IV defects with inversion symmetry, such as silicon vacancy (SiV), germanium vacancy (GeV), and tin vacancy (SnV) centers, have garnered increasing attention.

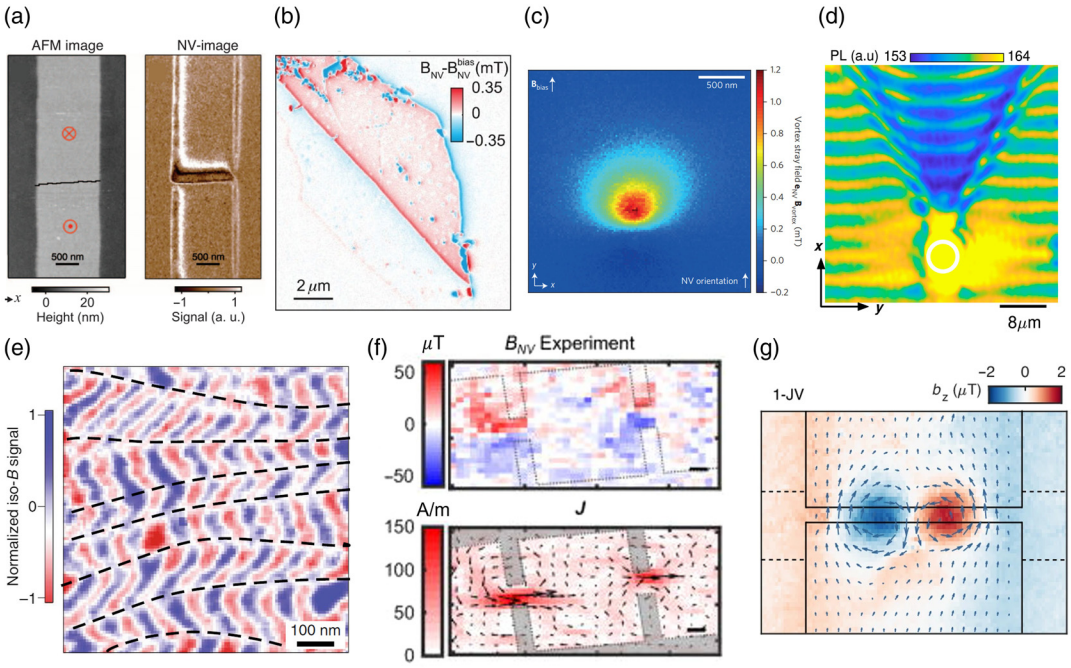

Fig. 13 Imaging examples using single-spin scanning magnetometry. (a) Magnetic images of magnetic domains (left) and a domain wall (right). Adapted and modified with permission from Ref. 37; © 2014 American Association for the Advancement of Science. (b) CrI_3 2D van der Waals ferromagnets. Adapted and modified with permission from Ref. 148; © 2019 The Authors, some rights reserved; exclusive licensee American Association for the Advancement of Science. (c) Single vortex in YBCO superconductors. Adapted and modified with permission from Ref. 39. © 2016 Springer Nature Limited. (d) Spin waves propagating on YIG surface. Adapted and modified with permission from Ref. 135; © 2021 The Authors. (e) $BiFeO_3$ multiferroic materials. Adapted and modified with permission from Ref. 150; © 2017 Macmillan Publishers Limited, part of Springer Nature. (f) Current flows in graphene devices. Adapted and modified with permission from Ref. 155; © 2021 The Authors. (g) Super currents in Josephson junctions. Adapted and modified with permission from Ref. 156; © 2024 The Authors.

These defects are notable for their large ZPL percentages and narrow emission linewidths. These properties enable all-optical coherent addressing of the electronic spin, showing potential for single-spin quantum sensing in tesla-range magnetic fields.[172]

Among other host materials, SiC has emerged as a promising alternative to diamond. With ∼250 polytypes, SiC supports a diverse set of spin defects, such as silicon vacancies, divacancies, and nitrogen vacancies, with emissions spanning the near-infrared (NIR) to infrared (IR) range.[173–177] This makes SiC highly suitable for bio-sensing and imaging, as NIR and IR wavelengths minimize cellular damage and allow for deeper tissue penetration. Notably, the V2 defect among silicon vacancies ($\lambda =$ 900 to 1100 nm) has demonstrated magnetic fields sensing with a sensitivity of 100 $\mathrm{nT/Hz^{1/2}}$ at room temperature, leveraging sharp photoluminescence variations near level anti-crossing without the need of an RF system.[178] In addition, purified 4H-SiC hosts V2 defects with outstanding ODMR sensitivities,[179] exhibiting a magnetic sensitivity of 4 $\mathrm{nT/Hz^{1/2}}$. On the other hand, divacancies ($\lambda = 1000$ to 1400 nm) have achieved thermal sensitivity of 13.7 $\mathrm{mK/Hz^{1/2}}$ using the thermal CPMG (TCMPG) protocol.[180] Similarly, nitrogen vacancies in 4H-SiC ($\lambda = 1150$ to 1400 nm) enable room temperature quantum sensing of AC fields with a spectral resolution of 10 kHz using XY8-2 correlation spectroscopy.[181] The near-telecom wavelength fluorescence in SiC not only facilitates practical applications in medical, chemical, and biological analysis but also improves its compatibility with fiber optics. A fiber-integrated SiC magnetometer using a 100 μm diameter sample achieved sensitivities of 12.3 $\mu\mathrm{T/Hz^{1/2}}$ for silicon vacancies and 3.9 $\mu\mathrm{T/Hz^{1/2}}$ for divacancies in 4H-SiC,[182,183] highlighting their potential for portable and practical quantum sensors.

Hexagonal boron nitride has also drawn attention as a new candidate host material for defect-based quantum sensing. As a van der Waals 2D material, hBN possesses great potential in flexibility,[184] integrability,[185] and compatibility with existing fabrication techniques.[186] Moreover, hBN hosts a variety of spin defects, including negatively charged boron vacancies (V_B^-)[187–189] and carbon-related (C-related) defects.[190,191] For instance, V_B^- has a longitudinal (transverse) ZFS of 3.48 GHz (∼50 MHz) at room temperature. The magnetic response in the ODMR spectrum indicates V_B^- as an $S = 1$ spin system, with the calculated sensitivity expected to reach up to 2.55 $\mu\mathrm{T/Hz^{1/2}}$. Although this sensitivity is somewhat moderate compared with diamond NV centers, the low-dimensional characteristics of hBN significantly enhance its potential as a versatile quantum sensing platform. Leveraging the thin film nature of hBN, spin defects can be deterministically integrated onto photonic integrated circuits[192] or fiber optics.[193] They can also be transferred in close

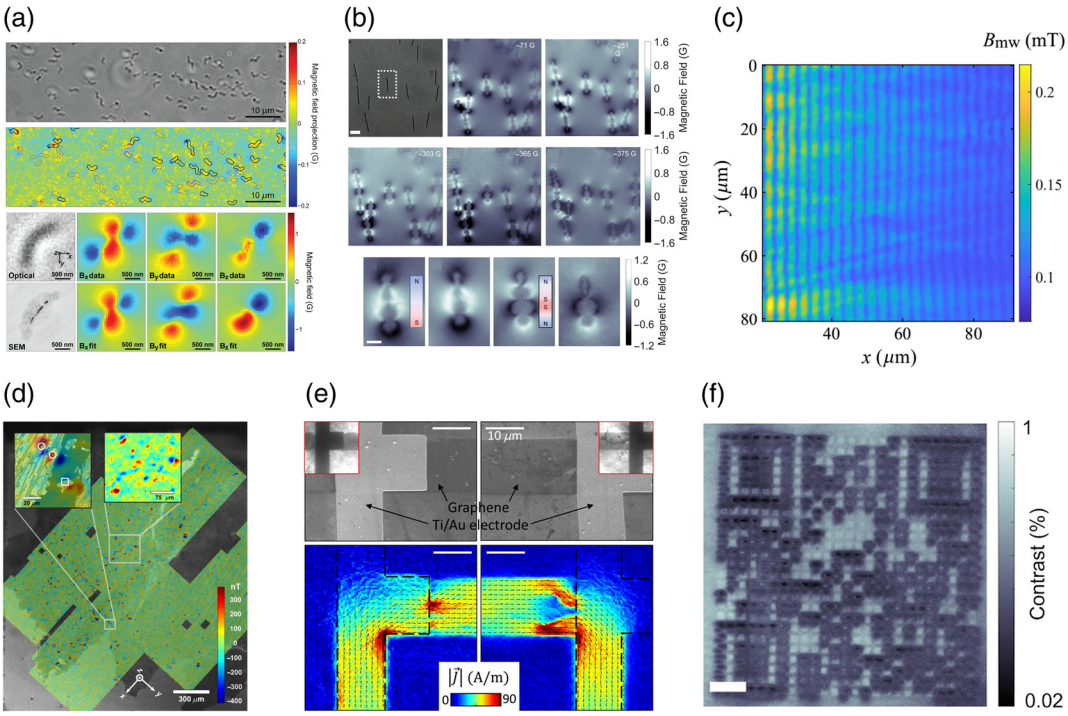

Fig. 14 Imaging examples using wide-field quantum microscopy. (a)–(f) Magnetic images. (a) Individual magnetotactic bacteria. Adapted and modified with permission from Ref. 162; © 2013 Springer Nature Limited. (b) Fe nanowires. Adapted and modified with permission from Ref. 138; © 2023 Wiley-VCH GmbH. (c) Spin waves propagating on YIG surface. Adapted and modified with permission from Ref. 163. (d) Weakly magnetized eucrite ALHA81001. Adapted and modified with permission from Ref. 160; © 2017 American Geophysical Union. (e) Current flows in graphene ribbons. Adapted and modified with permission from Ref. 149; © 2017 The Authors. (f) Magnetic steganography (imaging hidden magnetic features). Adapted and modified with permission from Ref. 164; © 2025 The Authors.

proximity to the sensing target. This has enabled magnetic imaging of van der Waals ferromagnets,[194,195] temperature sensing via Joule heating from laser absorption,[195] and strain sensing on nanostructured substrates.[196,197] This versatility highlights the potential of hBN-based spin defects for a wide range of quantum sensing applications.

In addition to the host materials discussed so far, numerous other candidates are capable of hosting spin defects. For instance, recent studies have explored new defects in GaN, investigating their optical and spin properties. Room temperature ODMR measurements have been successfully carried out in the wavelength range from visible[198] to telecom.[199] Although the exact origin of these defects remains unclear, angle-resolved and magnetic field-dependent ODMR measurements have been used to deduce their spin quantization axis and spin quantum number. With GaN's established presence in the light-emitting diode (LED) industry, it is positioned as a promising platform for spin defects.

Silicon, another representative semiconductor material, also shows great promise for quantum sensing. Spin defects such as T-centers and G-centers in Si are attracting attention due to their compatibility with complementary metal oxide semiconductor (CMOS) technology and emission at telecom wavelengths.[200,201] This compatibility presents a unique opportunity to leverage established photonic platforms, such as photonic-integrated circuits and fiber optics. However, the primary challenge of using defects in Si lies in the host material's relatively small bandgap, which restricts spin defect activation at cryogenic temperatures. Despite this limitation, Si remains a strong candidate for integrated quantum sensing platforms, as its solid-state architecture is easier to construct compared with other host materials.

In Table 1, we summarize and compare the optical properties (wavelength range, Debye–Waller factor, and lifetime) and spin properties (ZFS, spin quantum number, and spin coherence time) of the spin defects in the discussed host materials.

3 Advancing Optical Interfaces for Spin Defects

Quantum sensing based on spin defects involves optical initialization, manipulation, and readout of spin states. Therefore, having an optimal optical interface between spin defects and optical systems is crucial for enhancing sensing capabilities, such as sensitivity, accuracy, and speed. Conventional confocal scanning microscopy with bulk host material limits these sensing capabilities in several points. The spatial resolution is mostly restricted by the diffraction limitation of the optical systems, which is defined as $d \sim \frac{\lambda}{2\mathrm{NA}}$, referred to as the Abbe diffraction limit. In the case of sensitivity, following the equation $\Delta f \sim \frac{\Delta\nu}{\gamma_e C\sqrt{I}}$,[19]

Table 1 Summary of optical and spin properties of spin defects in diamond, SiC, hBN, Si, and GaN.

	Optical properties			Spin properties		
Defect kinds	Wavelength (nm)	$F_{\text{Debye–Waller}}$	Lifetime	Zero-field splitting (D_{ZFS}, E_{ZFS})	Spin quantum number (S)	Spin coherence (T_1, T_2^*, T_2)
Diamond						
NV^-	~620 to 800 nm[202,203] (ZPL: 637 nm)	0.044[204]	$m_s = 0$: 12 ns[81] $m_s = \pm 1$: 7.8 ns[81]	$D_{\text{ZFS}} = 2.87$ GHz[71,202] $E_{\text{ZFS}} = 1.423$ GHz[206]	$S = 1$	$T_1 = 3.6 \times 10^3$ s[205] $T_2^* = 470$ μs[207] $T_2 = 1.58$ s[205]
SiV^-	ZPL: 737 nm[208,209] (weak phonon sideband)	0.76 to 0.88[208]	1 to 2 ns[210,211]	$D_{\text{ZFS}} = 46.7$ GHz (ground state), 258.1 GHz (excited state)[210]	$S = 1/2$	$T_1 = 350$ ns[212] $T_2^* = 115$ ns[212]
SiV^0	946 nm[213]	0.9[214]	1.8 ns[214]	$D_{\text{ZFS}} = 942$ MHz[214]	$S = 1$[214]	
SnV	ZPL: 619 nm[215,216]	0.57[217]	~5 ns[216]	$D_{\text{ZFS}} = 820$ GHz (ground state), 3 THz (excited state)[218]	$S = 1/2$	$T_2^* = 5(1)$ μs[219] $T_2 = 10$ ms[218]
GeV	ZPL: 602.7 nm[220]	0.6[221]	1.4 to 5.5 ns,[220] 6.0 ns[221]	$D_{\text{ZFS}} = 152$ GHz (ground state), 981 GHz (excited state)[222]	$S = 1/2$[222]	$T_2^* = 1.43$ μs[223] $T_2 = 24.1 \pm 0.9$ ms[223]
4H-SiC						
V1	ZPL: 862 nm[224] 861 nm[227,228]	8%[225] 40%[228]	5.03 to 6.26 ns[226]	$D_{\text{ZFS}} = 5$ MHz (ground state), ~1 GHz (excited state)[225]	$S = 3/2$[224]	$T_2^* = 30 \pm 2$ μs[227] $T_2 = 0.8 \pm 0.12$ ms[227]
V2	ZPL: 916 nm[224]	9%[225]	6.1 to 11.3 ns[224] 7.08 ± 0.06 ns[229]	$D_{\text{ZFS}} = 70$ MHz (ground state), ~1 GHz (excited state)[225]	$S = 3/2$[226]	$T_1 = \sim 500$ μs[179] $T_2^* = 34$ μs[229] $T_2 = 1.39$ ms[229]
hBN						
V_B^-	~700 to 900 nm (ZPL: 773 nm)[230]	—	1.2 ns[187]	$D_{\text{ZFS}} = 3.48$ GHz $E_{\text{ZFS}} = 50$ MHz[231,232]	$S = 1$	$T_1 = 18$ μs[189] $T_2^* = 100$ ns[232] $T_2 = 100$ ns[189]
Carbon-related	540 to 620 nm[233]	0.8[233]	4.4 ns[233]	$D_{\text{ZFS}} = 25$ MHz, $E_{\text{ZFS}} = 5$ MHz ($S = 1$) [190] $D_{\text{ZFS}} = 7$ MHz, $E_{\text{ZFS}} = 2$ MHz ($S = 3/2$)[190]	$S = 1/2$[234] $S = 3/2$, 1[190]	$T_1 = 100$ μs[191] $T_2 = 2.45$ μs[235]
Silicon						
T-center[201]	935 meV (1326 nm)	0.23	0.94 μs			$T_1 > 16$ s $T_2 = 2.1$ ms
G-center[200]	ZPL: 1278 nm	0.2				
GaN						
Ref. 198	667 nm	>0.5		$D_{\text{ZFS}} \sim E_{\text{ZFS}} \sim 389$ MHz ($S = 1$) $D_{\text{ZFS}} = 368$ MHz, $E_{\text{ZFS}} = 0$ ($S = 3/2$)	$S = 1$, 3/2	
Ref. 199	1325 nm			$D_{\text{ZFS}} = 0.2$ GHz, $E \ll 2$ GHz	$S = 1$	

ZPL, zero-phonon line; $F_{\text{Debye–Waller}}$, Debye–Waller factor; D_{ZFS} and E_{ZFS}, ground and excited state zero-field splittings; S, defect's spin quantum number; T_1, T_2, and T_2^*, relaxation, coherence, and effective coherence times.

the sensitivity of spin defects-based quantum sensing (Δf: detectable frequency shift of ODMR spectrum) is strongly affected by the brightness (I) of spin defects as well as the linewidth ($\Delta\nu$) and contrast (C) of the ODMR spectrum. Furthermore, non-optimal excitation and collection conditions of spin defects degrade fidelity and extend integration time, which restricts the implementation of advanced quantum sensing protocols and limits their practical use. The spatial resolution and brightness can be further improved through advancements in the optical interface. In this section, we introduce several strategies to enhance the optical performances of spin defects: (1) nanostructure fabrication for improving light extraction, (2) micro- and nano-scale optical lenses for improving light collection, and (3) cavity coupling for enhancing light–matter interaction. The strengths and potential of each approach are discussed in detail below.

3.1 Low-Dimensional Nanostructure

As the high refractive index of host crystals hinders the extraction of fluorescence from spin defects, low-dimensional structures, such as nanoparticles, nanowires, and atomic-thin films, are getting great attention by serving significantly enhanced light extraction from defects.[69,235,236] Moreover, these structures can efficiently interface with various sensing platforms, including scanning tips,[16,145,146,237] fiber optics,[238–241] microfluid chips,[242] and photonic chips.[243–245] There are numerous nanofabrication techniques available for creating such structures, broadly categorized into bottom-up growth and top-down fabrication.

3.1.1 Zero-dimensional nanoparticle

Nanoparticles, as shown in Fig. 15(a), are a widely used form of nanostructures. These nanocrystals exhibit high optical

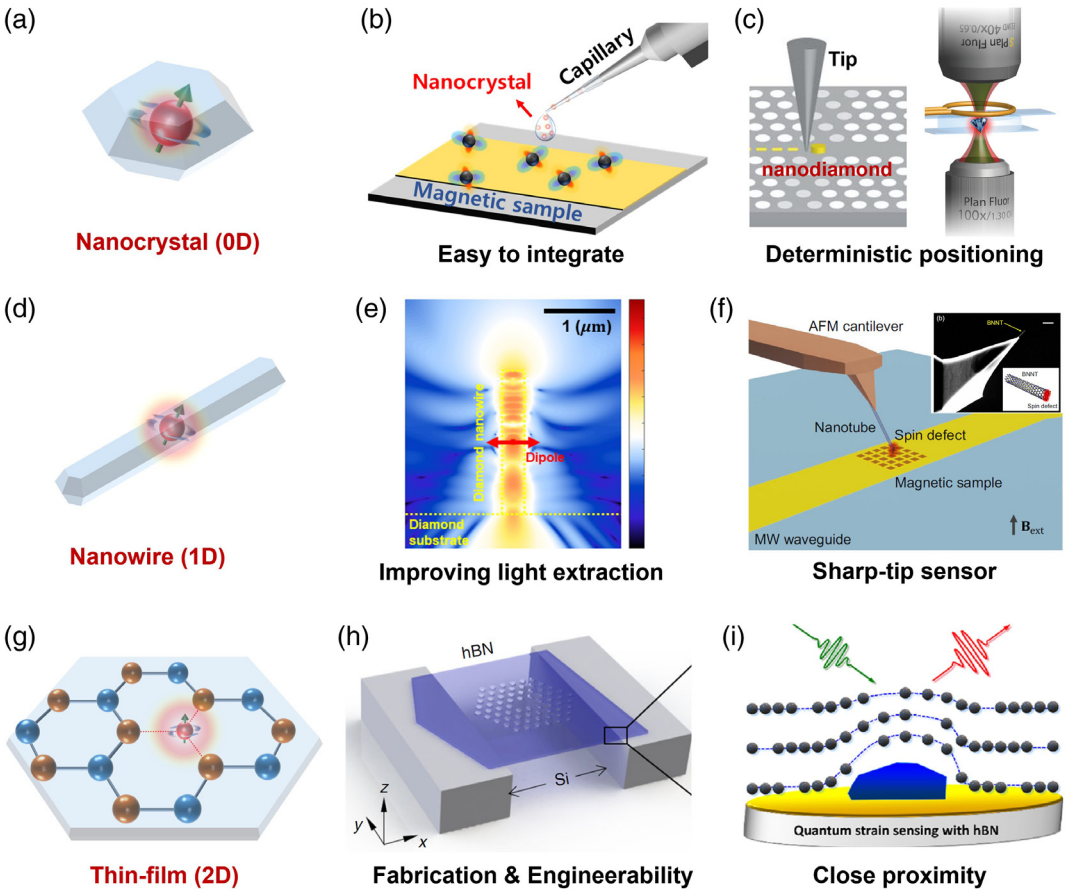

Fig. 15 Examples of low-dimensional nanostructures. (a) Schematic of spin defect in 0D nanocrystal and properties: (b) great integrability using a drop-casting method and (c) deterministic nanopositioning via mechanical tip and optical tweezer. (b) Adapted and modified with permission from Ref. 243; © Optica Publishing Group. (c) Adapted and modified with permission from Ref. 246; © 2021 American Chemical Society. (d) Schematic of spin defect in 1D nanowire and representative properties: (e) improved light extraction efficiency through optical guiding via one-dimensional nanostructure and (f) improved spatial resolution and spin addressing abilities via sharp-tip configuration. Adapted and modified with permission from Ref. 234 under CC-BY-NC-ND license. (g) Schematic of spin defect in 2D thin-film and its properties: (h) compatibility with nanofabrication. Adapted and modified with permission from Ref. 247 under CC-BY license. (i) Giant response to external mechanical deformation. Adapted and modified with permission from Ref. 196; © 2022 American Chemical Society.

brightness by minimizing total internal reflection,[69,235,236] and they offer an excellent integrability with various platforms. Figure 15(b) describes how nanodiamonds can be easily integrated with sensing targets using a drop-casting method, a technique also applicable for practical platforms such as optical fibers.[240] Moreover, their nanoscale size allows for precise positioning using a mechanical tip[243,248] or optical trapping technique,[246,249] as depicted in Fig. 15(c). These advantages of enhanced light extraction, integrability, and controllability make nanocrystals ideal for implementing efficient, deterministic, and potentially scalable quantum sensing through the arrangement of nanocrystal arrays.[235]

One prominent example of such utility is a tip-attached quantum sensing probe capable of single-defect operation for nanoscale resolution. Various host materials support spin defect emission in nanoparticle structures, including diamond,[69,250,251] SiC,[252] and hBN.[235,253] For high-resolution sensing, sub-10 nm nanocrystals are preferred due to their proximity to the target samples.[236] However, shallow defects in such small crystals often suffer from poor optical stability, including brightness fluctuation, bleaching, or quenching caused by surface-bound states.[254]

To mitigate these issues, several approaches have been explored, including highly purified nanocrystals using chemical vapor deposition (CVD), slow-growth techniques at high-pressure high-temperature,[255–257] or mechanical milling of high-quality bulk crystals.[258,259] Another approach involves post-growth treatments, such as surface modification via aerobic oxidation[250,260,261] or post-annealing process at prolonged high temperature at 1600°C.[262] In addition, scaling up the nanocrystal size, while keeping them below 100 nm, can help maintain optical and spin properties for nanoscale quantum sensing.[69]

3.1.2 One-dimensional nanowire

Recently, one-dimensional (1D) nanostructures, such as nanotubes and nanowires [Fig. 15(d)], have gained significant attention for their utility and compatibility with scanning probe systems and integrated photonic platforms for wide-field imaging. Fabricated diamond nanowires, for instance, exhibit enhanced photon extraction through optical routing along the nanowire axis, demonstrating up to a 10-fold improvement compared with unstructured NV and SiV centers.[263,264] Figure 15(e) displays a corresponding numerical simulation highlighting the enhanced light extraction via waveguiding effects in nanowire geometries.

Owing to these properties, ultra-bright wide-field imaging has been demonstrated using nanowire, nanopillar, and nanocone arrays fabricated on bulk diamond substrates.[170,171,265] In addition, the directional light guiding enabled by these nanostructures allows for efficient collection of PL, particularly from sharp-tip scanning probes. For example, PL collection from a single NV center has reached up to 2.1 Mcps due to improved optical coupling to the objective lens.[16,157] Beyond brightness enhancement, these 1D nanostructures also improve spatial resolution. Figure 15(f) illustrates a single C-related spin in a BN nanotube (~50 nm diameter) attached to an AFM cantilever, demonstrating high spatial resolution and strong photon collection for nanoscale sensing.[234]

Moreover, 1D elongated nanostructures can efficiently interface with mechanical forces, enabling ultra-sensitive force-sensing applications.[266,267] Mechanical modes induced by external forces can couple to spin sublevels, forming hybrid spin-nanomechanical sensing platforms.[29,268,269] Mechanical strain coupling, in particular, can modulate the spin qubit coherence, thereby enhancing spin coherence time and, in turn, improving sensitivity.[270]

Although the growth and synthesis of diamond-based nanowire architectures remain challenging, promising strategies involve the use of carbon nanotube[271] or silicon nanowire templates.[272] In addition, spin defects embedded in different stacking interfaces have attracted interest due to their unique optical properties, such as nontrivial optical performances in brightness and phonon dynamics. For example, recent studies on SiC nanowires have explored point defect-stacking fault complexes.[273] These systems exhibit enhanced brightness and suppressed electron-phonon coupling due to the proximity of stacking faults to point defects. As a result, strong ZPL emission from V_{si} is observed even at room temperature, with minimized phonon sidebands. Such features are highly advantageous for integration with photonic platforms, providing low-loss and low-dispersion optical interfaces.

3.1.3 Two-dimensional thin film

The utilization of thin film structures [Fig. 15(g)] is also an attractive candidate for quantum sensing, offering excellent integrability with targets and engineerability through established fabrication techniques. Such thin films can be prepared by CVD growth,[274–276] epitaxial layer growth (especially for SiC or GaN),[277,278] or by mechanical thinning and polishing of bulk crystals.[279–281] Among these, hBN, a van der Waals material, can be easily exfoliated down to atomic layers without requiring complex growth processes. This two-dimensional (2D) nature makes hBN compatible with nanofabrication, enabling precise engineering of the optical environment around spin defects.

These thin-film platforms are ideal for integrating photonic structures that tailor light–matter interactions. For example, Fig. 15(h) shows a photonic crystal cavity fabricated in an hBN membrane, where the coupling between spin defects and cavity photons enhances optical interfacing efficiency with external optical systems.[247] In addition, the mechanical flexibility of thin film materials allows them to respond strongly to external strain, making them suitable for wide-area sensing applications. As illustrated in Fig. 15(i), hBN atomic layers have been used to probe nanobubble morphologies on deposited metal films through their strain sensitivity.[196]

Beyond hBN, emerging spin-hosting materials such as Si and GaN offer significant advantages due to their compatibility with existing industrial infrastructure. Thin film growth of these materials supports scalable and wide-area sensor fabrication, which is essential for translating quantum sensing technologies into real-world applications. Thus, the development and integration of 2D thin films in spin-hosting materials are critical steps toward commercialization and practical deployment of quantum sensing platforms.

3.2 Micro- and Nano-Scale Optical Lenses

The aforementioned low-dimensional nanostructures offer excellent light extraction; however, their nanostructured surfaces often introduce optical instabilities, such as brightness fluctuations and blinking, as well as degraded spin coherence.[254,282–284] To mitigate these adverse effects, the use of micro- and nano-scale optical lenses for addressing spin defects has been extensively studied. These optical elements significantly enhance light extraction and photon collection efficiency without compromising

the optical or spin properties of the emitters. By employing such lenses, the NA of the optical interface is effectively increased, and the far-field emission profile of spin defects can be optimized for improved signal collection.[285–287]

Moreover, these modulated optical interfaces not only boost photon collection efficiency but also enable subwavelength spatial resolution.[288–291] Micro-optical lenses can be implemented either by fabricating the optical structures directly onto the host crystal, forming a monolithic platform,[292–294] or by integrating dielectric lenses onto the surface of spin-hosting materials.[295–299] More recently, the emerging field of meta-optics has been applied to quantum optics applications.[300–304] In particular, metalenses have demonstrated exceptional performance in photon collection, surpassing the limits of conventional diffractive optics. These improvements in brightness and optical resolution are critical for advancing the performance and reliability of quantum sensors.

3.2.1 Solid immersion lens

A solid immersion lens (SIL) is a widely used microlens for defect characterization, whose schematic is illustrated in Fig. 16(a). The first reported SIL was fabricated using focused ion beam milling (FIB) to create a hemispherical solid immersion lens centered around single diamond NV centers.[295] In this configuration, the NV center is precisely positioned at the focal point of the hemispherical SIL, enhancing the NA of the optical interface and significantly increasing the collimation angle of the emitted light. This improvement leads to a substantial boost in photon collection efficiency, with reported brightness enhancements exceeding an order of magnitude, as illustrated in Fig. 16(b). State-of-the-art implementations have achieved a saturated photon collection rate of up to 2.4 Mcps from a single NV center.[305]

Recent advancements in SIL fabrication include the development of Fresnel-type SILs,[306] which significantly reduce FIB milling time by more than 2/3 compared with hemispherical designs, thereby lowering fabrication costs. Beyond monolithic fabrication, alternative methods involve heterogeneous integration of commercially available SILs made from high-refractive-index materials such as gallium phosphide (GaP)[285] and gallium nitride (GaN).[298] These hybrid approaches preserve the structural integrity of the host crystal while still achieving considerable brightness enhancement without degrading the spin or optical properties of the defects. In addition, the lens material and dimensions can be tailored to optimize performance for specific types of spin defects and application requirements.

3.2.2 Microsphere

Microsphere-type lenses, as depicted in Fig. 16(c), offer distinct advantages over hemispherical SILs, particularly due to their unique ability to generate a spatially localized excitation spot known as a photonic nanojet,[289,307] and to efficiently convert evanescent waves into propagating waves.[308] These advantages in excitation and collection enable highly magnified, super-resolution imaging that surpasses the diffraction limit, achieving

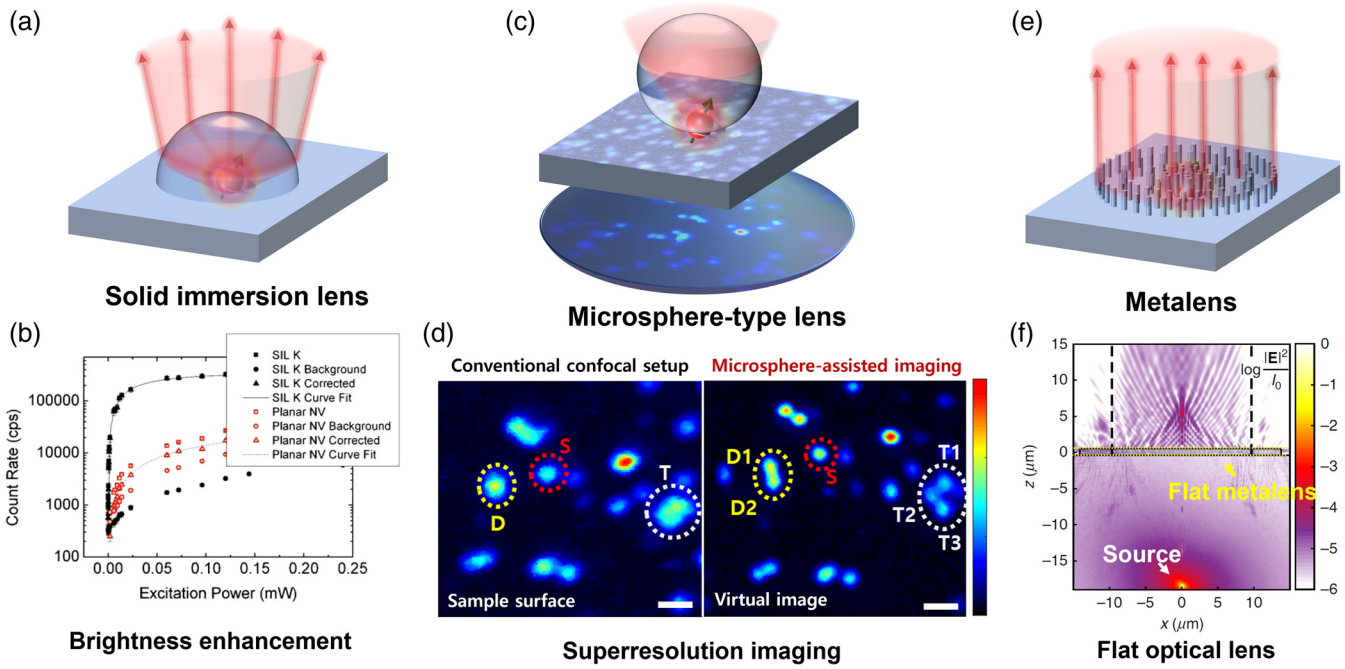

Fig. 16 Examples of micro- and nano-scale optical lenses. (a) Schematic of a solid-immersion lens and (b) brightness enhancement showing collected PL counts as a function of excitation power, with and without the lens. Adapted and modified from Ref. 295, with the permission of AIP Publishing. (c) Schematic of microsphere-assisted microscopy and (d) super-resolution imaging capability presenting confocal scanning images with and without the microsphere. The scale bars are 500 nm. Adapted and modified with permission from Ref. 296 under CC BY-NC-ND license. (e) Schematic of metalens featuring near-unity numerical aperture and (f) simulated optical emission profile achieved using the flat metalens structure. Adapted and modified with permission from Ref. 300 under CC-BY license.

spatial resolution as small as $\sim\lambda/17$ through a virtual image plane formed beneath the microsphere.[288,309]

When applied to spin defect characterization, microsphere-assisted confocal scanning microscopy facilitates the optical addressing of individual photons and spin states from closely spaced defects that are otherwise indistinguishable in conventional confocal microscopy.[296] As shown in Fig. 16(d), NV centers that appear spatially unresolved in standard confocal imaging (labeled D and T) can be distinctly resolved into subcomponents (D1-2 and T1-3) using a microsphere lens. In addition, this virtual imaging configuration significantly enhances SNR, with reported improvements of up to fourfold compared with direct imaging at the sample surface.

Microspheres are readily available as off-the-shelf micro-optics and can be easily deployed onto host materials via simple drop-casting methods. For precise alignment, microspheres can be positioned deterministically using micro-manipulation tools such as microtips[310] or optical tweezers.[296] Importantly, this method requires no complex fabrication, making it a versatile and noninvasive strategy compatible with a wide range of bulk materials and standard optical microscopy setups. Therefore, microspheres provide a relocatable, low-cost, and effective optical interface for enhancing the performance of solid-state quantum emitters.

3.2.3 Metalens

The introduction of meta-optics offers a powerful pathway to achieve near-unity NA in photon collection using thin membrane structures.[311] As illustrated in Fig. 16(e), which shows a schematic of a metalens coupled to spin defects, flat meta-optical architectures such as monolithically fabricated diamond metalenses have been developed. These structures consist of nanopillar arrays engineered to mimic discretized Fresnel phase profiles.[300] In this work, a brightness enhancement of 3.5 times was reported at a collimation NA of 0.75.

A key strength of this approach lies in the ability to fabricate these meta-optics architectures as ultra-thin membranes, as shown in Fig. 16(f). By harnessing this thin membrane design, hybrid integration of silicon dioxide (SiO_2) metalens membranes onto NV centers in bulk diamond has been demonstrated, achieving a 34-fold enhancement in photon collection compared to pristine bulk media.[312] Moreover, their ultra-thin nature allows metalenses to interface with diverse photonic platforms, such as the facets of an optical fiber.[313,314] In addition, metalenses offer tunable focusing depth[315] and exhibit chiral functionality,[316,317] enabling applications across a wide range of use cases—from addressing spin defects at varying depths to generating distinct optical responses to circularly polarized light. Therefore, metalenses represent a lightweight, customizable, and high-performance optical interface with transformative potential for quantum sensing.

3.3 Cavity-Enhanced Light–Matter Interaction

Enhancing the brightness of spin defects with optical lenses is a useful way to improve sensing sensitivity. Beyond such passive optical interfaces, photonic cavities offer an active approach to tailoring light–matter interactions, enabling precise modification of the optical properties of coupled defects. These modifications include spectrally selective enhancement at a ZPL, increased spontaneous decay rates, and optimized optical propagation modes. To illustrate the effect of photonic cavities on promoting light–matter interaction between spin defects and cavity photons, we can refer to a quantum optical framework. In this context, the enhancement of spontaneous radiative emission is characterized by the Purcell factor $F_P \sim Q/V$,[318] where $Q \sim \lambda/\Delta\lambda$ is the quality factor of the cavity mode and V is the mode volume.

High-Q cavities, such as dielectric photonic crystals where $\Delta\lambda$ is extremely small, exhibit ultra-narrow spectral enhancement and reduced dispersion. These features make them especially advantageous for integrated sensing platforms.[319] By contrast, cavities with small V, such as plasmonic antennas, are well suited for enhancing spatial resolution by confining spin defect emission within a tightly localized optical mode. These effects contribute to both improved SNR through enhanced radiative decay rates and optimized far-field emission patterns, and higher spatial resolution via confined mode volumes.

In the strong coupling regime, interactions between cavity photons and spin defects lead to the formation of new hybridized states. These states enable coherent transfer of information between spin and photonic degrees of freedom, forming the basis for spin-photon interfaces.[320] Such modifications to light–matter interaction via photonic cavities have been explored across a variety of platforms and coupling regimes.

3.3.1 Dielectric photonic cavity

The fabrication of dielectric photonic cavities on host media has been extensively developed across various fields of nanophotonics. Representative examples include photonic crystals [Fig. 17(a)][282] and circular Bragg gratings [Fig. 17(b)],[325] which have been successfully integrated with NV centers in diamond. These monolithic dielectric photonic cavity structures are also compatible with a wide range of host materials, including the aforementioned crystals. By leveraging such dielectric photonic crystal cavities, enhanced spin sensitivity has been demonstrated through cavity-coupled spin defects, as in the case of the L3 photonic crystal cavity in SiC [Fig. 17(e)].[321] The cavity-coupled emission enables enhanced optical signal readout, resulting in improved contrast in spin characterization.

Importantly, these dielectric photonic cavities can selectively enhance specific optical frequencies, allowing suppression of background fluorescence and the generation of low-dispersion modes in integrated photonic platforms. For instance, Fig. 17(f) shows selective enhancement of the NV center's ZPL at 637 nm in diamond photonic crystal cavities.[322] Beyond enhancing the radiative decay rate, the cavity's diffractive structure can also modulate the far-field propagation profile. As shown in Fig. 17(g), a monolithic circular Bragg grating cavity in hBN exhibits a strong vertical emission pattern.[323]

For coupling photons in optical fibers or photonic integrated circuits, tapered nanobeam cavities[324] and photonic crystal waveguides[326,327] are employed, as shown in Figs. 17(c) and 17(d). These lateral photon-routing configurations enable efficient coupling, for example, a tapered photonic crystal nanobeam achieves >90% coupling efficiency to the facet of a tapered silica fiber, as shown in Fig. 17(h).[324] As a result, single-mode fibers can collect ~38 kcps of single-photon emission from the SiV in diamond. In summary, the integration of dielectric micro- and nano-cavities enables simultaneous enhancement of radiative decay rates, reduction of optical dispersion, and improved photon collection along desired optical pathways. These advantages collectively facilitate the realization of highly sensitive and efficiently integrated quantum sensing platforms.

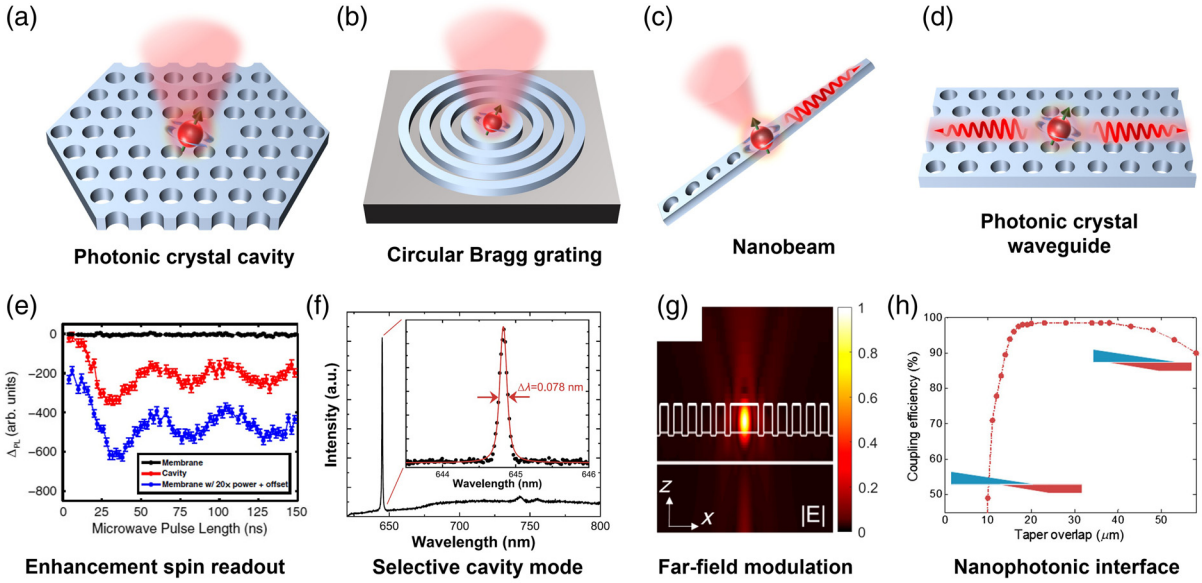

Fig. 17 Examples of dielectric photonic cavities. Schematics of (a) photonic crystal cavity, (b) circular Bragg grating, (c) photonic crystal nanobeam, and (d) photonic crystal waveguide. Nanophotonic architectures offer several distinct advantages: (e) enhanced spin readout contrast in ODMR spectra, (f) selective cavity-enhanced PL emission with significant Purcell enhancement, (g) far-field engineering to narrow the emission angle for improving PL collection efficiency, and (h) the provision of an efficient nanophotonic interface with exceptionally high coupling efficiency to integrated photonic platforms. Images are adapted and modified with permission from Refs. 321–324.

3.3.2 Plasmonic antenna and cavity

Plasmonic cavities offer significant advantages due to their broadband optical coupling modes and ultra-small mode volumes, making them highly compatible with randomly distributed, phonon-broadened emission from spin defects. Their extremely small mode volumes enable very high Purcell enhancements. One of the simplest methods to induce plasmonic interactions between spin defects and localized plasmons involves positioning metal nanoparticles, such as gold or silver, around the spin defects.[328–330] Figure 18(a) shows schematics of metal nanoparticles placed close to diamond NV centers.[328] Due to the broadband spectral response of plasmonic enhancement, the brightness of NV center emission is enhanced across a wide wavelength range, unlike high-Q dielectric photonic cavities, as shown in Fig. 18(d).

Another approach involves coupling shallow-embedded spin defects to surface plasmons on a metal thin film [Fig. 18(b)]. As shown in Fig. 18(e), the enhancement in brightness due to surface plasmonic interactions is evident in confocal PL images comparing SiC regions on Au coplanar waveguides with pristine regions.[331] This configuration demonstrated a brightness enhancement of ∼7-fold and a ∼14-fold improvement in spin manipulation sensitivity, highlighting the strong performance of plasmonic cavity effects. Similarly, shallow V_B^- centers in hBN, when coupled to surface plasmons, achieve magnetic field sensitivity of sub-10 $\mu T/Hz^{1/2}$ even under continuous-wave ODMR measurement, a regime where typical sensitivities are around 100 $\mu T/Hz^{1/2}$.[333]

Recent developments have focused on low-loss plasmonic nanocavity structures to further optimize plasmonic enhancement. For example, Fig. 18(c) illustrates an advanced nanopatch antenna consisting of a metallic naocube sandwiched with a metal substrate, yielding an extremely confined optical mode. Spin defects in hBN embedded between such a nanocube and a thin metallic film have demonstrated PL enhancement of up to ∼250-fold without compromising ODMR contrast. Figure 18(f) shows simulation results indicating the dependence of brightness enhancement on the distance between shallow spin defects and the metallic substrate, with optimal enhancement observed at distances below 10 nm.

Similar approaches have also been demonstrated using Au nanotrenches,[334] metasurfaces,[335] nanogaps,[336] and other nanostructures.[337] Importantly, plasmonic cavities are relatively simple to fabricate[338] and can even be integrated with dielectric nanophotonic cavities,[339,340] enabling hybrid metal-dielectric platforms. Such configurations offer promising pathways toward chip-integrated optical quantum sensing platforms with enhanced performance and scalability.

3.3.3 External optical cavity

External optical cavities typically consist of two or more optical mirrors that trap light between them, enabling sustained photon confinement.[341] A key advantage of such cavities is the tunability of their resonant modes, which can be readily adjusted to match the emission spectrum of target spin defects. By varying the distance between the mirrors, the cavity's optical path length can be controlled, thereby tuning the steady-state photonic density and enhancing light–matter interactions when spin defects are positioned within the cavity.

Figure 19(a) illustrates the schematic of an optical setup for optical cavity-enhanced room temperature magnetometry. It consists of a 532 nm pump laser, a 1042 nm probe laser, and

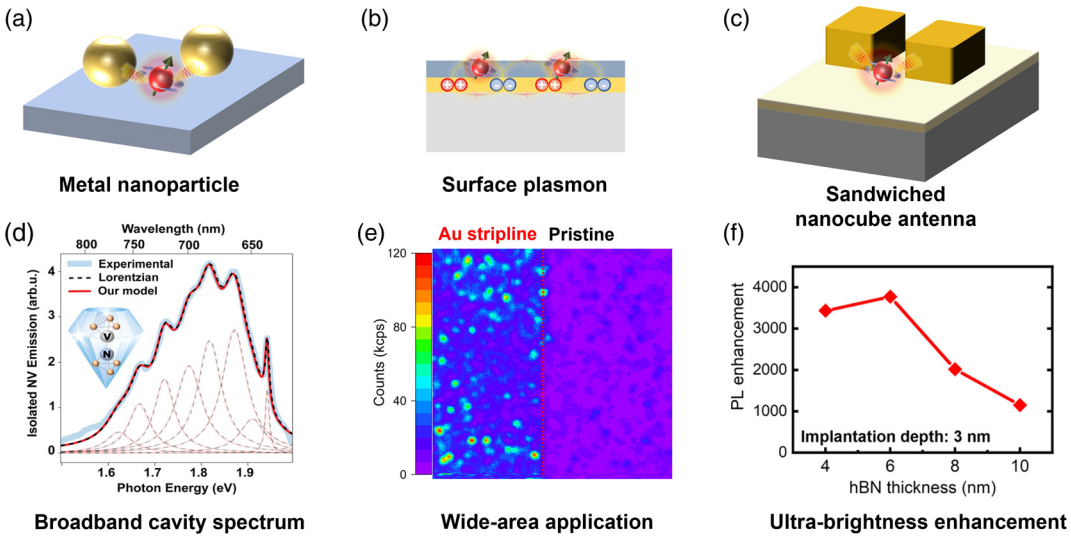

Fig. 18 Examples of plasmonic cavities and antennas. Schematics of (a) plasmonic nanoparticles, (b) surface plasmon resonance, and (c) plasmonic nanoantenna. Plasmonic cavities offer unique advantages including: (d) a broadband cavity mode spectrum of plasmonic nanoparticles interacting with diamond NV centers. Adapted and modified with permission from Ref. 328 under CC-BY license. (e) Large-area applicability with substantial brightness enhancement, as demonstrated in the confocal PL mapping of spin defects in SiC interacting with Au coplanar lines. Adapted and modified with permission from Ref. 331; © 2023, American Chemical Society. (f) Simulated PL enhancement as a function of the distance between the plasmonic antenna and spin defects. Adapted and modified with permission from Ref. 332; © 2023, American Chemical Society.

two spherical mirrors forming a cavity around diamond NV centers. The probing laser is resonant with the metastable singlet transition of the NV center and is used to acquire the ODMR transmission spectrum.[335,341] To enable miniaturization, one study implemented a packaged cavity structure by bonding a bulk diamond with an integrated planar mirror to a piezoelectric transducer, paired with a spherical mirror.[342] This configuration demonstrated magnetic field sensitivity near the photon shot-noise limit, confirming the sensitivity enhancement enabled by cavity-assisted detection [Fig. 19(b)].

A similar approach has been used to explore collective effects in cavity-coupled NV centers. Figure 19(c) shows a photograph of a device comprising a spherical micromirror aligned with a diamond membrane on a planar mirror.[343] This configuration significantly enhances ZPL emission from the NV centers, as observed in the cavity mode spectrum [Fig. 19(d)]. Second-order correlation measurements at the filtered ZPL reveal photon bunching behavior, indicative of superradiance among the coupled emitters [Figs. 19(e) and 19(f)]. These collective emissions enable access to the quantum-enhanced sensing regime.[343,344]

Importantly, cavity-mediated interactions among spin defects not only support enhanced sensing via superradiance but can also be used to explore subradiant states for potential quantum storage applications,[345] which may further contribute to improving sensitivity.[114] Therefore, photonic cavities provide a powerful platform for engineering photon-mediated interaction between spins, offering significant promise for advanced quantum sensing.

4 Practical Application of Defect-Based Quantum Sensors

So far, we have discussed the fundamental principles and recent advancements in quantum sensing, particularly efforts to enhance sensitivity and optical properties. Alongside fundamental research, there is growing interest in utilizing quantum sensors for practical, real-world applications. Defect-based quantum sensors, with their unique advantages, are proving to be highly versatile and well-suited for use across a wide range of fields, including biomedical,[52,57,85,346–354] industrial,[193,355–363] and military sectors.[29,65,364–368] For these sensors to be practical in real-world applications, they must meet certain conditions, such as the ability to function at ambient room temperature and the development of miniaturized, integrated sensor systems.

In this context, defect-based quantum sensors offer several compelling benefits. Their qubits are highly sensitive to various physical properties, including magnetic,[13,14] electric,[32] and strain fields,[369] as well as temperature,[25] inertial,[29] and rotational motion.[368] They also can function across a wide range of temperatures, including room temperature,[78] provide high-resolution imaging with both spatial[38] and temporal precision,[52] and can be integrated into compact, portable devices.[193,359–361] Although challenges remain, particularly in reducing costs and enhancing sensitivity to compete with existing classical sensor technologies, defect-based quantum sensors, especially those based on diamond NV centers, have made significant progress and show potential across numerous applications, as outlined in Tables 2 and 3.

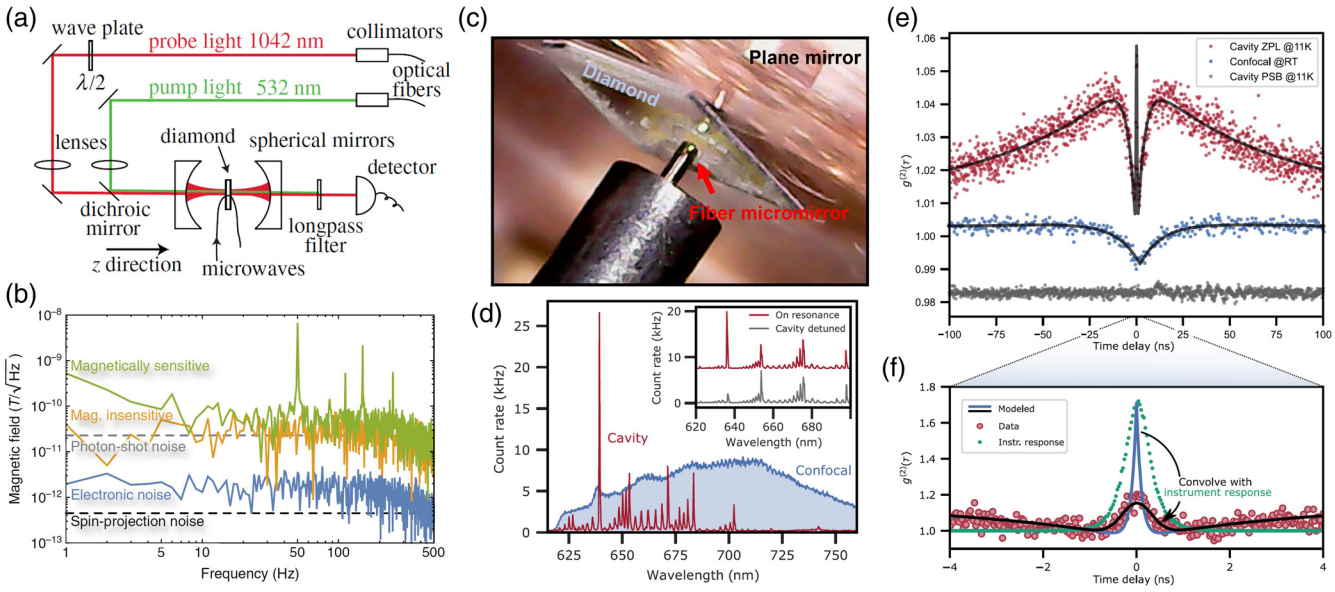

Fig. 19 Examples of external optical cavities. (a) Schematic of the optical setup used for diamond NV centers embedded in an optical cavity, with excitation and probing lasers. Adapted and modified with permission from Ref. 341; © 2014 American Physical Society. (b) Measured magnetic field sensitivity of the cavity-coupled diamond NV center approaches the photon-shot noise limit, achieving 22 pT/Hz$^{1/2}$. Adapted and modified with permission from Ref. 342; © 2017 American Physical Society. (c) Photograph of the optical cavity setup, consisting of a fiber-based micromirror aligned with a diamond membrane on a planar mirror. (d) Observed cavity mode spectrum corresponding to the setup in panel (c) shows significant PL enhancement at the ZPL of the NV center. (e) Second-order autocorrelation measurement revealing collective photon bunching characteristics for the cavity-coupled ZPL emission, with a pronounced bunching at zero-time delay on a sub-nanosecond timescale. By contrast, confocal imaging without spectral filtering at the same sample location exhibits photon anti-bunching, whereas filtering only the phonon sidebands shows neither bunching nor anti-bunching. (f) Enlarged view of $g^{(2)}(\tau)$ from (e) near-zero time delay. Images in panels (c)–(f) are adapted and modified with permission from Ref. 343 under CC-BY license.

Table 2 Diamond NV centers' sensitivities to various physical properties.

Physical property	Sensitivity
Magnetic field	~1 nT/Hz$^{1/2}$ (single NV)[13]
	<1 pT/Hz$^{1/2}$ (ensemble)[14]
Electric field	~200 V cm^{-1}/Hz$^{1/2}$ [Ref. 33]
Strain field	~10^{-7}/Hz$^{1/2}$ [Ref. 369]
Temperature	~76 μK/Hz$^{1/2}$ [Ref. 370]
Inertial motion	~10 to 100 pN/Hz$^{1/2}$ [Ref. 29]
Rotational motion	~1 deg /s/Hz$^{1/2}$ [Ref. 65]

Table 3 Diamond NV centers' unique advantages for quantum sensing applications.

Property	Performance
Spatial resolution	~10 nm (single NV)[38]
Operating temperature	Sub-kelvin to over room temperature
Diamond fabrication	Various nanostructures and devices can be fabricated
Spectral resolution	<1 mHz[52]
Detection bandwidth	DC – GHz
Compact sensor design	~10 cm^3 [Ref. 359]
Others	Optically stable (free from photobleaching); chemically stable, non-toxic, and bio-friendly; robust against harsh environments, e.g., temperature, pressure, high-voltage/current

In this section, we highlight recent advancements in defect-based quantum sensors, focusing on their use in various fields, including biomedical diagnostics, semiconductor manufacturing device inspection, portable sensors for harsh industrial environments, and aerospace and military applications. Although other types of defects are still largely in the realm of basic research, diamond NV centers have already made substantial progress toward practical, real-world applications.

4.1 Biomedical Diagnostics

Biomedical applications are among the fastest-growing fields leveraging NV-based quantum sensors. NV centers have been

employed to probe local temperature and magnetic fields within individual cells, tissues, and neurons, offering several key advantages for biomedical use. They cover a wide frequency range, from DC to GHz, enabling the detection of static magnetic fields from magnetic nanoparticles (MNPs),[85,162,349,351,371] sub-millisecond transient signals from action potentials,[85,346,348] and GHz-frequency signals from ions used in magnetic resonance.[85,353,354,372,373] NV centers also serve as highly effective fluorescence markers, especially when embedded in nanodiamonds.[85,353,354] Compared with quantum dot-based markers, NV centers are more resistant to photobleaching, enhancing their durability and reliability in long-term imaging.[77] In addition, the host material, diamond, is nontoxic and biocompatible, making it ideal for biological applications.[77] When combined with imaging techniques such as scanning magnetometry and wide-field quantum microscopy, both single NV centers and ensembles provide powerful tools for biomedical diagnostics, providing resolution from the nanometer to micrometer scale.[50,52,347–349,351,373–376] In this section, we explore various topics in biomedical applications, including nano- and micro-NMR, magnetic resonance imaging (MRI), cell detection, virus diagnostics, neuron activity monitoring, and magnetocardiography, highlighting the broad potential of NV centers in advancing biomedical science.

4.1.1 NMR and MRI: nanometer, micrometer scales, and microfluidics

As discussed in Sec. 2, various sensing protocols have been developed to enhance sensitivity, spatial and spectral resolutions in NMR measurements. These protocols include pulsed and continuous dynamical decoupling, as well as coherently averaged synchronized readout, as discussed in Sec. 2. Individual proton spins have been detected within 1 s of integration using two-qubit quantum systems consisting of a single NV center and a neighboring ^{15}N nuclear spin.[57] In addition, proton spins in a volume of ten picoliters have been detected using ensemble NV centers, with a sensitivity of 30 pT/Hz$^{1/2}$.[52] Alongside efforts to increase sensitivity, various methods to amplify the signal itself have been explored, such as polarizing nuclear spins beyond their thermal populations using techniques such as dynamic nuclear polarization and parahydrogen-based signal amplification by reversible exchange.[377–379] High spectral resolution is crucial for identifying different nuclear spins and chemical shifts resulting from interactions with the local chemical environment. Using nuclear memory qubits or synchronized readout techniques, high spectral resolution on the order of one part per million or sub-mHz has been demonstrated.[52,57]

For spatially resolved NMR, the imaging techniques described in Sec. 2.3 are combined with single or ensemble NV centers to achieve MRI at nanometer and micrometer scales. For nanometer-scale MRI, the NMR sample is mounted on a scanning probe microscope, e.g., an atomic force microscope, and scanned over a single NV center embedded in a diamond plate.[50,374] This configuration is advantageous because the NV center is positioned in a fixed position, providing stability during the scanning process. As a result, sensitive NMR protocols, such as XY8-N, can be applied over prolonged periods. Early experiments have successfully demonstrated 2D NMR images of ^{1}H nuclear spins in poly-methyl methacrylate[50] and ^{19}F nuclear spins in Teflon microspheres [Fig. 20(a)],[374] with spatial resolution of $\sim$12 nm and 29 ± 2 nm, respectively. As the NV's sensing volume is fixed, the scanned image provides a laterally resolved NMR image, limiting it to 2D MRI. To extend this technique to full three-dimensional (3D) MRI, large magnetic field gradients are required to differentiate nuclear spins along the vertical direction. Recent experiments have demonstrated 3D NMR spectroscopy of neighboring nuclear spins in diamond by utilizing strong local magnetic field gradients, either from the intrinsic magnetic dipole field of the NV center[380,381] or from externally fabricated microwire structures.[382] Applying similar techniques to achieve 3D MRI on external samples remains an area for further research.

Although scanning probe-based MRI offers nanometer-scale resolution, its small imaging area and slow scanning process limit both the image size and acquisition time. This limitation can be overcome using wide-field quantum microscopy, which provides a larger field of view ($\sim$100 μm^2 to mm^2) and spatial resolution on the order of several hundred nanometers. Early experiments using ensemble NV centers with wide-field quantum microscopy demonstrated 2D MRI of ^{19}F nuclear spins in CaF_2 islands[375] and fluorinated samples,[49] achieving lateral resolutions of $\sim$40 and $\sim$500 nm, respectively. Recently, this technique has been integrated with microfluidic platforms.[352,353,372,376,383] Microfluidic channels offer several advantages: biomolecular samples can be continuously supplied and maintained in a bio-friendly, *in vivo* environment with constant temperature and pH. In addition, samples can be polarized and detected at various points along the channels, providing flexibility in setup design and reducing the need for large-scale equipment.[352] Furthermore, microfluidic systems enable precise control over sample flow, volume, biochemical reactions, and real-time monitoring.[352,353,372,376,383] As a result, combining micro-MRI with microfluidic channels enhances the technique's suitability for biomedical applications.

4.1.2 Cell detections and virus diagnostics

NV centers are also utilized for the detection of individual cells and viruses, offering a novel diagnostic tool for the quantitative analysis of various biological samples. These samples range from naturally existing magnetic species, such as magnetic chains in magnetotactic bacteria[162] and malarial hemozoin paramagnetic crystals,[384] to magnetically labeled samples, including SKBR3 cancer cells,[351] human lung tumor tissues,[349] and mammalian cells and tissues.[371]

MNPs are commonly used as magnetic tags, which are incorporated into living cells and tissues to generate localized magnetic fields.[349,351,371] Figure 21(a) illustrates the concept of magnetic tagging: MNPs are selectively bound to SKBR3 cancer cells, allowing magnetic imaging to differentiate between MNP-labeled cancer cells and nonlabeled healthy cells, which are not identifiable under optical microscopy.[351] Figure 21(b) demonstrates immunomagnetic microscopy, a technique that quantitatively identifies the density of MNPs and reconstructs magnetic images using deep learning algorithms.[349]

Although MNPs serve as magnetic tags for DC field sensing, magnetic ions such as Gd^{3+}, Cu^{2+}, Mn^{2+}, and Fe^{3+} are employed as spin labels for AC field sensing.[353,372,373,385] These ions are commonly used as contrast agents in magnetic resonance imaging or naturally occur in ferritin protein cells. Their ESR occurs at GHz frequencies, influencing the NV T_1 relaxation time. T_1 relaxometry measures this GHz magnetic noise from the ions by tracking changes in T_1 time. Imaging ions has been demonstrated at both nanometer and micrometer scales using scanning magnetometry and wide-field quantum microscopy. For instance, ferritin proteins in Hep G2 cells [Fig. 21(c)] and

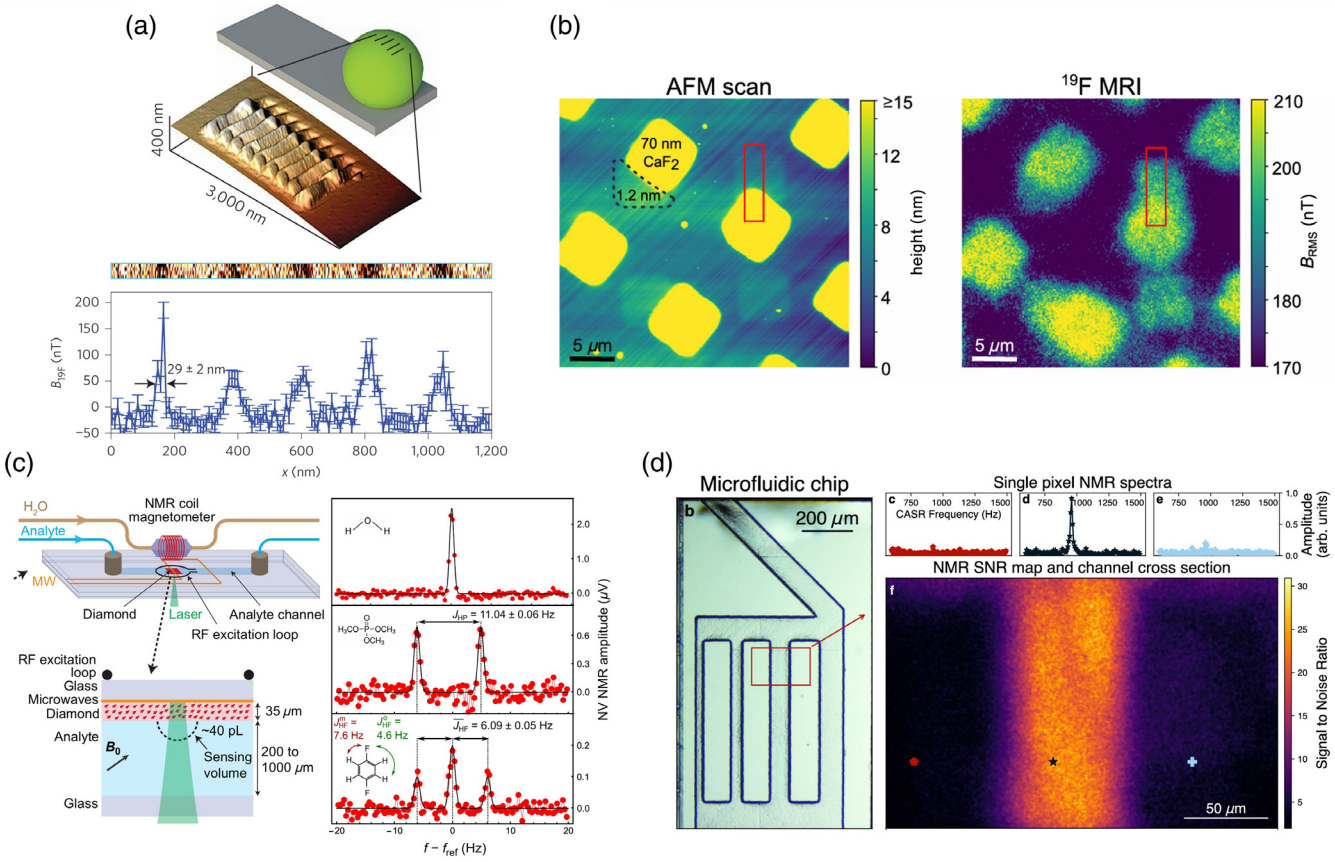

Fig. 20 NMR and MRI with diamond NV centers. Examples of 2D MRI images at nanometer (a) and micrometer (b) scales. (a) NMR signals of ^{19}F-rich Teflon microspheres, mounted at the tip apex of an atomic force microscope, are recorded and imaged by a single NV center located beneath the tip. Nano-indented grating patterns on the sample are captured in the scanning MRI experiment, demonstrating a spatial resolution of 29 ± 2 nm. Adapted and modified with permission from Ref. 374; © 2015 Springer Nature Limited. (b) 2D MRI image of ^{19}F nuclear spins in CaF_2 islands measured by wide-field diamond microscopy, achieving a spatial resolution of ∼40 nm. Adapted and modified with permission from Ref. 175 under CC-BY license. Examples of 2D NMR spectroscopy (c) and imaging (d) based on microfluidic platforms. (c) The polarization and detection sites are separated using a microfluid channel, enabling NMR spectroscopy on water, trimethyl phosphate (TMP), and 1,4-difluorobenzene (DFB) samples, with a spectral resolution of 0.65 ± 0.05 Hz. Adapted and modified with permission from Ref. 352; © 2019 The Authors, some rights reserved; exclusive licensee American Association for the Advancement of Science. (d) Overhauser dynamic nuclear polarization (ODNP) and coherently averaged synchronized readout (CASR) techniques are employed to convert ^{1}H NMR signals in a microfluidic chip into optical signals, which are then imaged using wide-field diamond microscopy. Adapted and modified with permission from Ref. 376; © 2025 The Authors.

Cu^{2+} ions [Fig. 21(d)] have been imaged with spatial resolutions of ∼10 and ∼300 nm, respectively.[372,385]

Functionalized nanodiamonds have also been studied for rapid point-of-care diagnostic tests for contagious viruses, such as SARS-CoV-2 and HIV.[353,354] Figure 21(e) illustrates the use of T_1 relaxometry to detect the SARS-CoV-2 virus with Gd^{3+} ions.[353] In this setup, the surface of the nanodiamond is functionalized with *c*-DNA linked to Gd^{3+} complex molecules. When viral RNA binds to the *c*-DNA on the nanodiamond surface, the Gd^{3+} ions detach, reducing magnetic noise detected by the NV centers, which results in the recovery of the T_1 time. This method demonstrates sensitivity down to several hundred viral RNA copies, with a false-negative rate of less than 1%.[353]

In addition to T_1 relaxometry, a novel fluorescence detection method has been employed for *in vitro* biosensing.[354] To separate the fluorescence signal from the NV center in nanodiamonds from background autofluorescence, an amplitude-modulated MW field is applied to the functionalized nanodiamonds, modulating the NV's fluorescence emission, which is then detected by lock-in measurement. This technique provides a detection limit of 8.2×10^{-19} mol for a biotin–avidin model and enables single-copy detection of HIV-1 RNA [Fig. 21(f)].[354]

4.1.3 Toward clinical applications: MCG and MEG

Two potential clinical applications of NV-based magnetic sensors are magnetocardiography (MCG) and magnetoencephalography

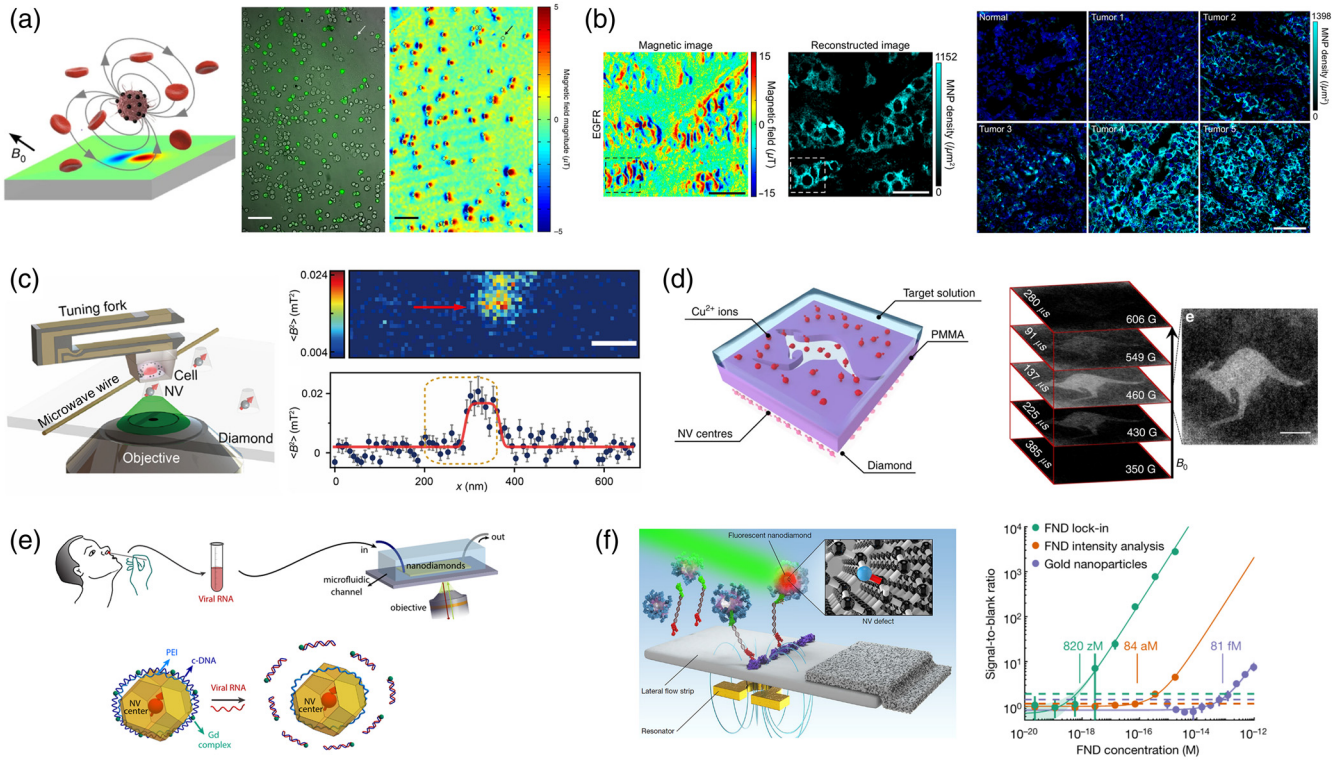

Fig. 21 Cell detections and virus diagnostics with diamond NV centers. (a), (b) DC magnetic imaging of magnetic nanoparticles (MNPs). (a) SKBR3 cancer cells. Adapted and modified with permission from Ref. 351; © 2015 Springer Nature America, Inc. (b) Human lung tumor tissues. Adapted and modified with permission from Ref. 349; © 2022 The Authors. (c), (d) AC magnetic imaging of Cu^{2+} and Fe^{3+} ions. (c) At the nanometer scale using scanning probe microscopy. Adapted and modified with permission from Ref. 372; © 2024 The Authors. (d) At the micrometer scale using wide-field quantum microscopy. Adapted and modified with permission from Ref. 385; © 2017 The Authors. (e), (f) Diagnostic measurements using functionalized nanodiamonds. (e) SARS-CoV-2 viruses. Adapted and modified with permission from Ref. 353; © 2021 American Chemical Society. (f) HIV viruses. Adapted and modified with permission from Ref. 354; © 2020 The Authors.

(MEG), which are used to detect cardiac and neural signals.[346,347,386,387] MCG measures stray magnetic fields induced by electrical currents flowing through the heart, whereas MEG detects magnetic signals generated by action potentials in neural networks. MEG requires sensitivity at the $\mathrm{fT/Hz^{1/2}}$ level, but cardiac magnetic signals are typically several orders of magnitude stronger than neural signals, making them detectable by NV magnetic sensors. In addition, many heart diseases, such as atrial flutter and atrial fibrillation, are characterized by irregular current flow in the heart at the millimeter scale, necessitating miniaturized magnetic sensors. Diamond sensors based on ensemble NV centers can be compact ($\sim$10 $\mathrm{cm^3}$) and offer sensitivities in the 1 to 100 $\mathrm{pT/Hz^{1/2}}$ range, making them well suited for MCG applications in diagnosing cardiovascular diseases. Recent experiments with diamond magnetic sensors have successfully measured magnetic cardiac signals from anesthetized and thoracotomized rats. For instance, Fig. 22(a) demonstrates the detection of magnetic cardiac signals from a living rat with a sensitivity of 9 $\mathrm{pT/Hz^{1/2}}$ using a 5 mm-sized sensor.[347] The results of NV-based MCG are consistent with conventional electrocardiography (ECG) measurements, underscoring the potential of NV-based MCG sensors for clinical use.

For MEG applications, NV centers still require further improvements in sensitivity. Early proof-of-principle experiments have demonstrated the ability to detect magnetic fields generated by ionic currents propagating through marine worm axons and mouse corpus callosum axons, as shown in Fig. 22(b). With a sensitivity range of 10 to 50 $\mathrm{pT/Hz^{1/2}}$ and sub-microsecond temporal resolution, these experiments enable the measurement of magnetic field traces from transient action potentials occurring on the millisecond time scale.[346]

Recent theoretical calculations, shown in Fig. 22(c), suggest that neural network imaging will soon be possible with an improved wide-field quantum microscope setup. This setup could achieve an area-normalized sensitivity of $\sim$10 $\mathrm{nT/\mu m}$, with $\sim$100 μm spatial resolution and $\sim$1 ms temporal resolution, averaged over 10^2 to 10^3 repetitions.[387] However, single-shot imaging of neural activity still requires significant improvements in sensitivity by several orders of magnitude. This could be achieved by optimizing diamond treatment and enhancing T_2^*.

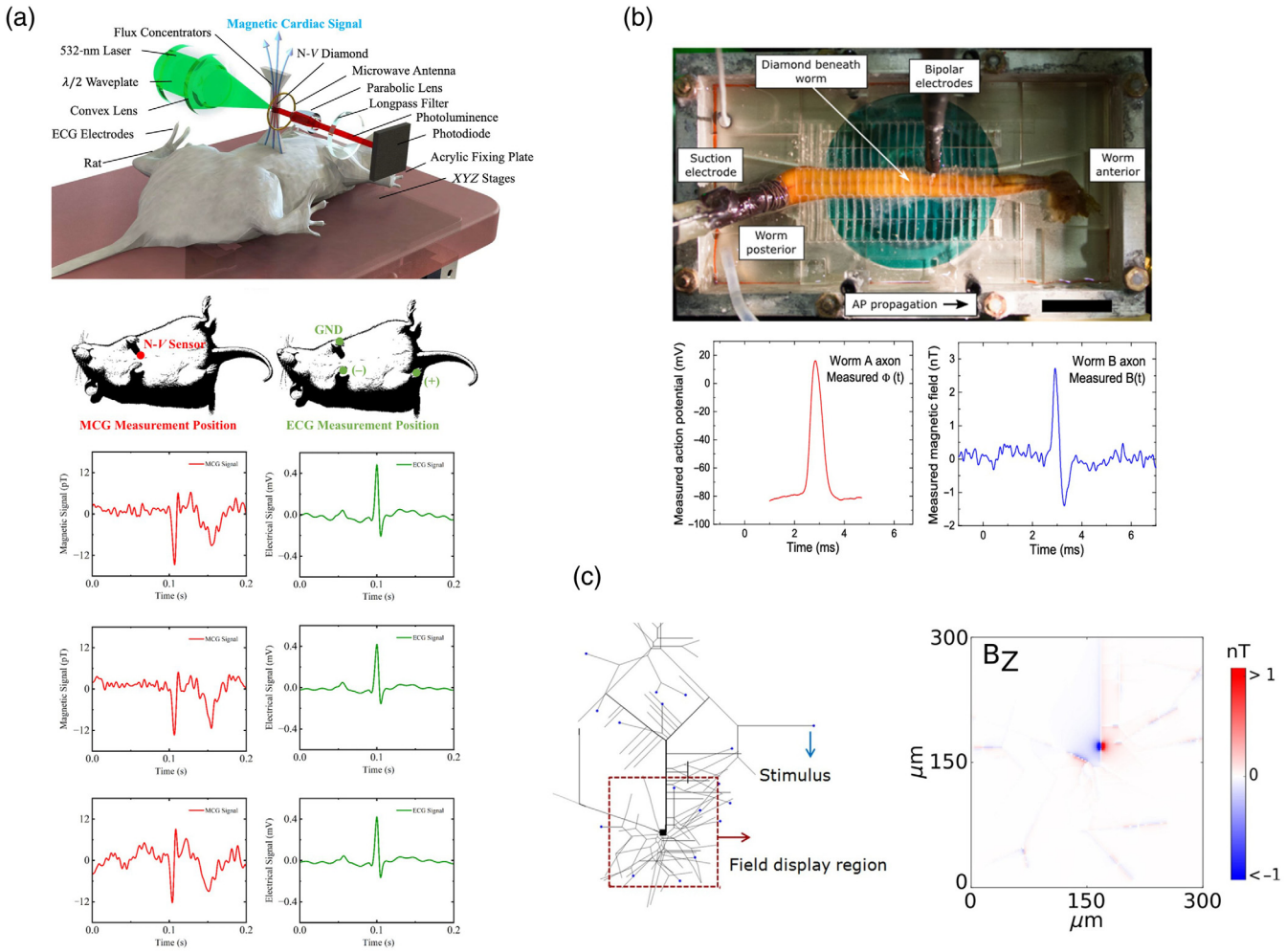

Fig. 22 Magnetocardiography (MCG) and magnetoencephalography (MEG) sensors based on diamond NV centers. (a) Detection of magnetic cardiac signals from a living rat. Adapted and modified with permission from Ref. 347; © 2024 American Physical Society. (b) Measuring transient magnetic signals due to action potentials propagating through marine worm axons. Adapted and modified with permission from Ref. 346. (c) Simulated results of magnetic images in neural networks. Adapted and modified with permission from Ref. 387; © 2018 The Authors.

4.2 Semiconductor Device Inspection

The continuous advancement of semiconductor technology and the miniaturization of electronic components have led to the development of complex circuitries and sub-micrometer devices with high density and 3D compound structures. As these devices become more intricate and densely packed, there is an increasing demand for new methods to characterize device performance and detect manufacturing flaws at the microscopic level. With their high field sensitivity and spatial resolution, diamond NV centers provide powerful, noninvasive tools for investigating the magnetic and electronic properties of semiconductor devices. In this section, we explore recent efforts in semiconductor device inspection and diagnostics, focusing on applications such as individual bit detection in magnetic random access memory (MRAM) and current flow analysis in integrated circuit (IC) devices.[356–358]

4.2.1 Individual magnetic bits in MRAM

Diamond scanning magnetometry has proven to be an invaluable technique for characterizing MRAM devices at the nanometer scale.[356] MRAM is a nonvolatile memory that stores information in magnetic bits. It relies on arrays of magnetic tunnel junctions (MTJs), which consist of two magnetic layers separated by a tunnel barrier. Magnetic information is stored based on the relative magnetization orientations of these layers: a parallel alignment represents "1," whereas an anti-parallel alignment represents "0." External magnetic fields can switch the magnetization direction of one of the layers, enabling data writing. As the MTJ pillars in MRAM devices are typically smaller than several tens of nanometers, analyzing device performance and identifying manufacturing flaws at the individual bit level requires both high field sensitivity and nanometer spatial resolution. Therefore, diamond scanning magnetometry serves as a novel tool for investigating MRAM devices.

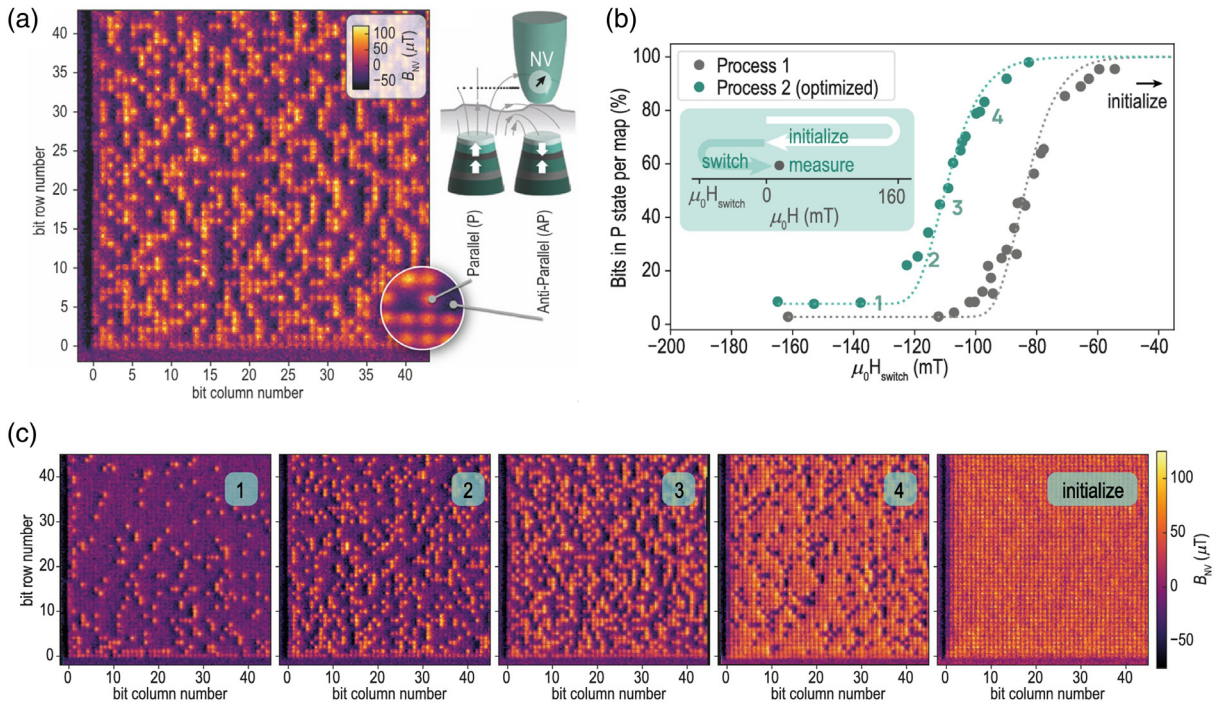

Fig. 23 Nanometer-scale inspection of MRAM performance. (a) A magnetic image of STT-MRAM array of 45 × 45 bits. Percentage of the parallel bits as a function of an external magnetic field (b) and corresponding magnetic images (c). Images are adapted and modified with permission from Ref. 356; © 2024 The Authors.

For instance, Fig. 23 presents magnetic images of a spin transfer torque-MRAM (STT-MRAM) array consisting of 45×45 bits.[356] The NV center probes the distinct magnetic fields from the parallel and anti-parallel states of individual MTJ pillars, providing valuable insights into the switching behavior. These magnetic images offer a comprehensive overview of the bit switching process, allowing the characterization of key device properties such as magnetic characteristics, switching statistics, and uniformity across the magnetic bits. Figures 23(b) and 23(c) show the percentage of parallel bits as a function of the external magnetic field. By analyzing the bit-switching data, Borràs et al. were able to extract critical magnetic properties, including retention values (Δ) and anisotropy fields (H_k).[356] This novel nanoscale magnetic imaging technique holds significant potential for the MRAM industry, providing a method to characterize MRAM performance and screen device imperfections during the early stages of the manufacturing process.

4.2.2 IC devices

In addition to characterizing magnetic devices such as MRAM, NV centers can also be used to image current profiles in electronic devices by measuring the Oersted magnetic fields generated by currents in the DC to GHz frequency range. For instance, wide-field diamond microscopy has been successfully applied to image current flow in printed circuit board traces, MW devices,[143] and photovoltaic devices.[388] By measuring the Oersted stray field, a 2D current density map (J_{2D}) can be reconstructed using the Biot–Savart law:

$$B(r) = \frac{\mu_0}{4\pi} \int d^3 r \frac{J(r) \times (r - r_0)}{|r - r_0|^3}. \quad (5)$$

Recent research has also focused on expanding the capabilities of current flow imaging to more complex electronic circuits, such as ICs.[357,358] Nanodiamond-based NV centers and wide-field quantum microscopy have been utilized to study IC microchips.[357,358,389] For instance, nanodiamonds distributed over GaN HEMT junctions enable the simultaneous mapping of magnetic fields and temperature changes induced by current flows.[389] On the other hand, wide-field quantum microscopy has been used to image magnetic fields generated by complex current paths in IC devices, facilitating the visualization of current profiles in multilayered devices and enabling the identification of malicious circuitry or Trojans.[357]

For example, Fig. 24(a) shows an experiment on a commercial FPGA designed to image current flow within ring oscillator clusters.[357] These clusters, which consist of multiple ring oscillators, allow the control of current flow in different regions of the FPGA, switching between active and idle states. The magnetic field profiles measured by NV centers are overlaid on high-resolution optical images of the circuit die. Although most of the magnetic images align with the device's designed structure, some features in the images reveal sub-surface structures or discontinuities in current flow. These hidden features, such as disconnected traces, are not easily detected in optical images, highlighting how magnetic imaging can offer a new approach to characterizing IC devices. In addition, quantitative analysis using machine learning techniques has been shown to identify the pre-programmed active states of the FPGA, paving the way for detecting hardware attacks such as malicious circuitry or Trojans and preventing counterfeiting during the manufacturing and distribution stages.

A key challenge in applying diamond microscopy at an industrial level is extending nearly 2D images into three

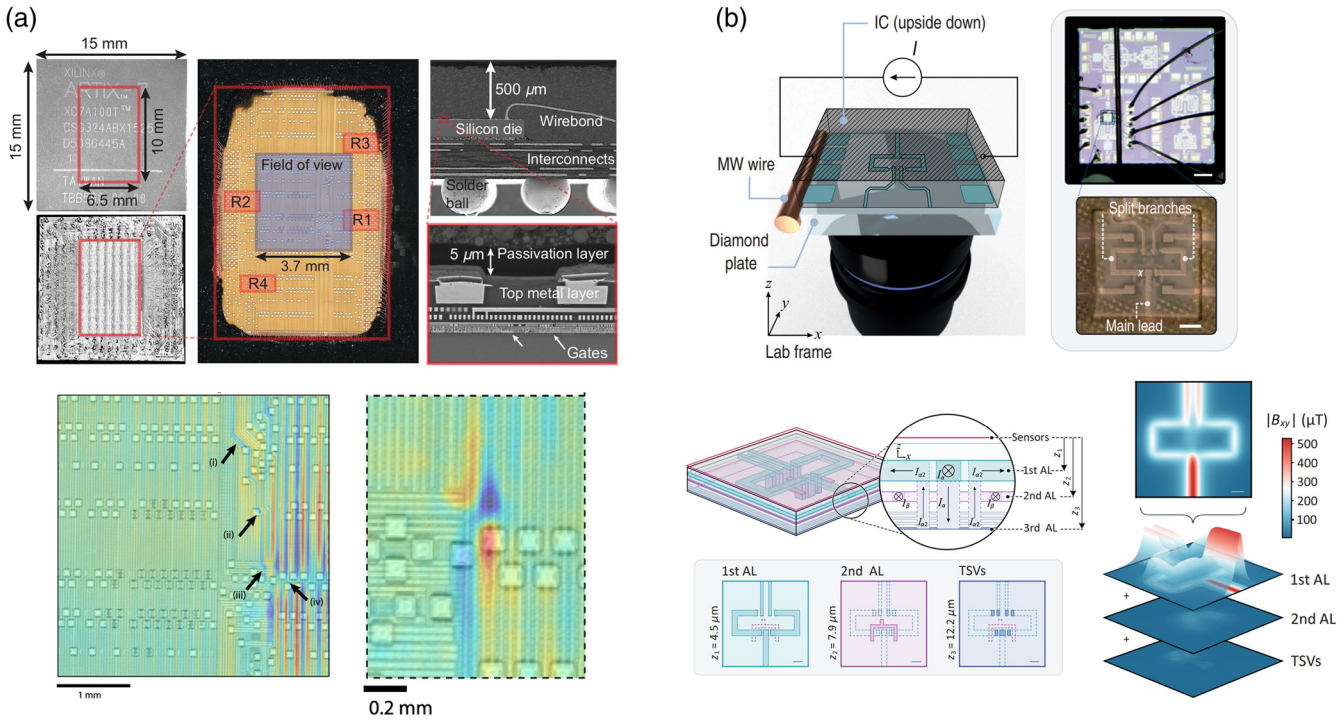

Fig. 24 Imaging current flows in integrated circuits (ICs). (a) Optical and magnetic images of an FPGA device. Magnetic images due to the current flows in the device are overlaid with optical images of the device. Adapted and modified with permission from Ref. 357; © 2020 American Physical Society. (b) 3D magnetic images due to the current flows in multilayered IC devices. Adapted and modified with permission from Ref. 358; © 2024 American Physical Society.

dimensions. As the Oersted magnetic field induced by current flows in wires decays rapidly with distance (e.g., 1/distance), imaging sub-surface current flows at greater depths becomes challenging. Recent work, shown in Fig. 24(b), has demonstrated 3D current imaging up to ∼12 μm in the vertical direction within multilayered IC devices.[358] By modeling magnetic field profiles in three dimensions (x, y, z) using the Biot–Savart law, Garsi et al.[358] were able to isolate Oersted fields from different layers of the device. However, this method requires prior knowledge of the device's structure and layout. Extending this technique to deeper layers of a chip will require further improvements in sensitivity and spatial resolution. In addition, the practical application of diamond microscopy in the semiconductor industry faces challenges due to the complex architectures of multilayer IC devices, which consist of billions of transistors, metal layers, and wire networks. This complexity makes image analysis challenging and necessitates further research to refine these techniques for more efficient and accurate device characterization.

4.3 Industrial Applications

In addition to the high field sensitivity and broad dynamic range, diamond quantum sensors offer several other significant advantages for industrial applications. One of the key strengths is their ability to function across a wide range of temperature and pressure conditions, including room temperature and ambient environments. The host material, diamond, provides exceptional resilience to extreme temperatures, high radiation levels, and aggressive chemical conditions, ensuring the sensors remain durable and reliable even in harsh environments. Moreover, the sensor head, which houses a diamond plate with an ensemble of NV centers, can be integrated into compact, miniaturized sensor systems.[11,12,359,360,390–393] This is particularly beneficial in industries where space is limited or where multiple sensors need to be deployed in close proximity. This section highlights some of the pioneering efforts in the development of compact, portable diamond quantum sensors, as well as their emerging industrial applications, including magnetic detection of elevator motion, measurement of metal sheet thickness, real-time monitoring of current flows in electric vehicle (EV) batteries, and high-voltage current measurements in power network systems.[193,361–363]

4.3.1 Compact and portable sensors

In laboratory-scale experiments, diamond magnetometers based on ensembles of NV centers have demonstrated magnetic sensitivity, reaching as low as $\mathrm{pT/Hz^{1/2}}$.[14] However, there has been a growing effort to extend these advancements beyond the laboratory environment and develop compact magnetometers suitable for real-world industrial applications. Achieving this requires integrating essential sensor components, such as light sources, MW circuits, detectors, and the diamond sensor head, while ensuring that the high sensitivity observed in controlled lab environments is maintained.

Figure 25 showcases recent advancements in miniaturized diamond magnetometers, typically ranging in size from a few $\mathrm{cm^3}$ to several tens of $\mathrm{cm^3}$.[11,359,360,390,392–394] The diamond plate itself is small, typically in the millimeter scale, and contains NV centers with densities ranging from 10^{13} to 10^{17} per $\mathrm{cm^3}$.

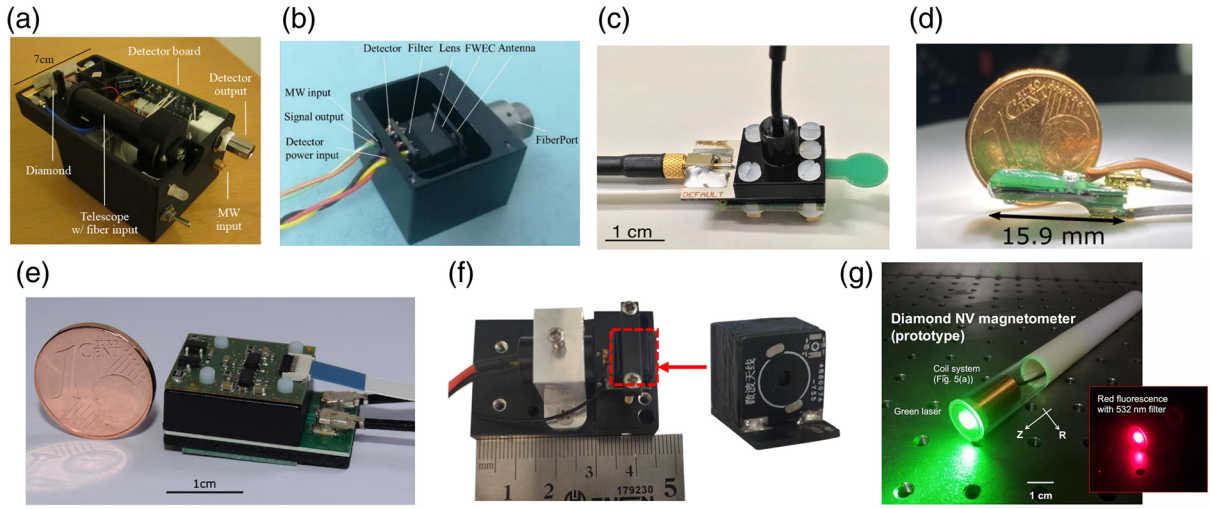

Fig. 25 Examples of miniaturized diamond quantum magnetometers with various configurations. (a)–(c) Photodetector-integrated designs using optical fibers for light delivery. (a) Adapted and modified with permission from Ref. 354; © 2020 The Authors. (b) Adapted and modified with permission from Ref. 11; © 2019 The Authors. (c) Adapted and modified with permission from Ref. 394; © 2020 IOP Publishing Ltd. (d), (f) Designs with both light source and detector integrated into the sensor head. (d) Adapted and modified with permission from Ref. 392; © 2024 The Authors. (e) Adapted and modified with permission from Ref. 360; © 2022 Elsevier B.V. (f) Adapted and modified with permission from Ref. 393; © 2022 IEEE. (g) A fiber-coupled design in which both the light source and detector are located outside the sensor head. Adapted and modified with permission from Ref. 390; © 2020 The Authors.

The diamond plate is then integrated with various commercial or custom-designed components, such as LEDs, MW circuit boards, optical elements (e.g., lenses and filters), and photodetectors.[11,360,392,393] To further reduce the sensor's overall size and minimize potential spurious coupling between MW sources and the detector, some designs use external lasers and photodetectors connected to the sensor head via optical fibers.[12,359,390,391,394] The reported sensitivities from these compact sensors range from a few hundred $\mathrm{pT/Hz^{1/2}}$ to $\mathrm{nT/Hz^{1/2}}$, representing a significant step toward realizing practical, portable diamond magnetometers for industrial applications.

Figure 26 illustrates examples of portable diamond sensors for industrial applications, such as detecting elevator movement and measuring the thickness of steel sheets. The diamond sensor shown in Fig. 26(a) demonstrates real-time detection of magnetic fields induced by the movement of an elevator.[361] The sensor successfully monitors changes in magnetic fields as the elevator approaches the second level of the building where the sensor is located. In addition, the sensor detects the magnetic field change in real time when the elevator doors open. On the other hand, Fig. 26(b) presents a fiber-integrated hBN sensor used to measure the thickness of metal sheets by assessing the amount of magnetic field shielding caused by the sheet.[193] This compact fiber-based sensor is realized by integrating an hBN circular Bragg grating cavity, which contains V_B^- spin defects, with an optical fiber. In this experiment, the steel sheet acts as a magnetic shield, and the sensor measures the suppression of the external magnetic field with varying sheet thicknesses, ranging from 0 to 9 mm.

For broader industrial applications of portable magnetometers, further development is necessary to make the entire sensor system even more compact, including the integration of external controllers and data analysis units, while maintaining high magnetic field sensitivity over a wide dynamic range. These advancements are crucial to enhancing the versatility and usability of portable sensors in diverse industrial environments.

4.3.2 Battery monitor in electrical vehicles

Compact diamond sensors are also applied for monitoring EV battery systems. As the electric automobile market grows and concerns about battery safety become more prominent, accurate current sensors are critical for assessing the state of charge (SOC) of EV batteries. These sensors help predict remaining battery lifetime and drive range, and identify potential hazards in battery operations.

Figure 27 demonstrates how compact diamond sensors are used to monitor current flows in the busbar of an EV battery module.[362,395] These sensors can detect magnetic fields generated by a busbar current of 20 mA, even when external magnetic noise is as high as 80 μT. The system employs two separate diamond sensors placed on opposite sides of the battery busbar, measuring magnetic fields from opposing currents. By performing a differential measurement between the two sensors, the system effectively cancels out external magnetic noise, which is common in real driving situations. This approach significantly improves the accuracy of SOC estimation, suggesting that the EV's driving range could be increased by 10%.[362,395] Despite these advancements, further research and optimization are necessary to improve the sensor's versatility for different charging situations. With ongoing development, these sensors will be better equipped to monitor EV battery performance reliably under real driving conditions.

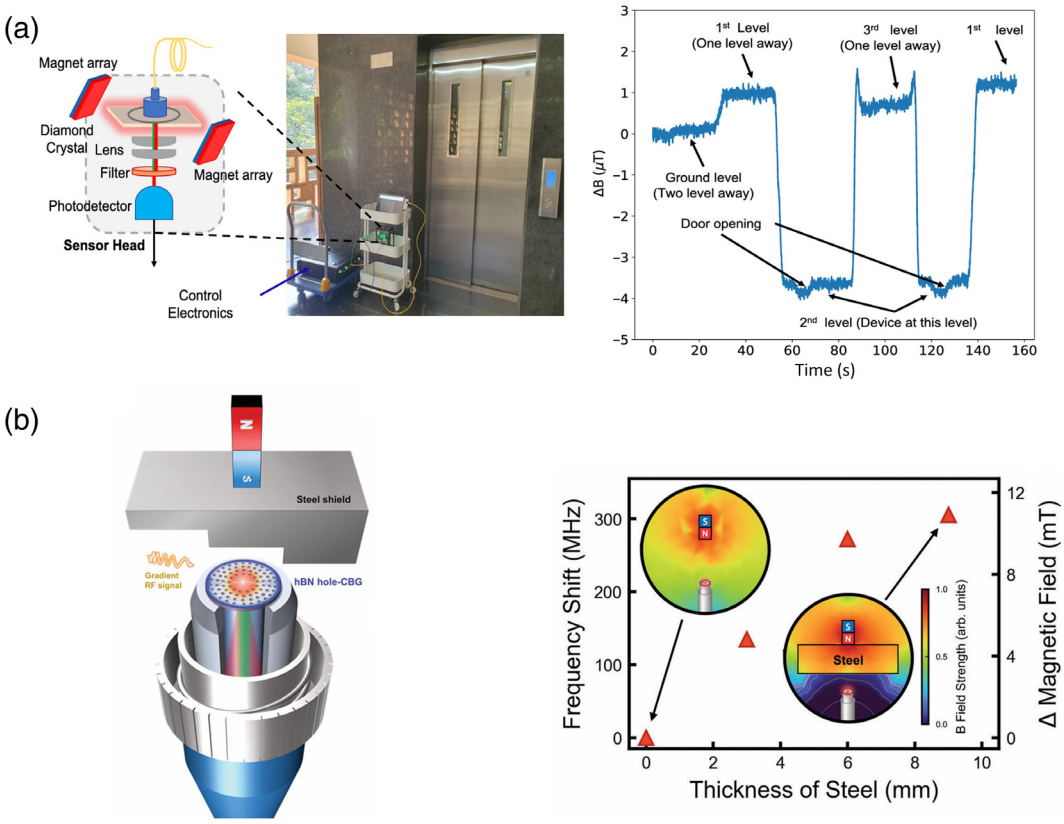

Fig. 26 Examples of industrial applications using compact, portable defects-based magnetometers. (a) Real-time detection of magnetic fields induced by the movement of an elevator. Adapted and modified with permission from Ref. 361; © 2024 The Authors. (b) Measurements of the thickness of metal sheets by monitoring the amount of field shielding by the sheets. Adapted and modified with permission from Ref. 193; © 2024 The Authors.

4.3.3 Harsh environment: high-voltage grids in power network systems

In high-voltage power grid systems, accurate current measurement is critical for minimizing energy losses and preventing hazards such as overheating of cables and equipment. As power network systems require current sensors capable of measuring large currents (several kA) within confined spaces, diamond sensors present a significant solution for monitoring currents in these environments.[363]

Figure 28 illustrates an example of how diamond sensors can be implemented in electrical power systems. Liu et al.[363] proposed a design that separates the diamond sensor head from the control units for practical reasons, such as limited space near the high-voltage side and challenges associated with delivering MW signals through coaxial cables in high-voltage areas. The compact diamond sensor is placed on the high-voltage side, whereas the control units (including laser, MW circuits, detectors, and power supplies) are positioned on the low-voltage side. Optical excitation and readout of the NV centers are achieved using optical fibers, and MW drives are transmitted with directional antennas. In proof-of-principle experiments, this remote sensor system, positioned 11 m apart, successfully measured currents with high accuracy, showing only a 0.4% error over 1000 A.[363] This demonstrates the potential of diamond sensors for high-voltage power grid applications. However, for practical implementation in the power grid, further improvements are needed to enhance the sensor's sensitivity and the efficiency of the directional antenna system.

4.4 Military and Navigation Applications

Diamond sensors are becoming increasingly valuable in the aerospace and military sectors due to their unique capabilities in providing self-reliant navigation systems that operate without dependence on Global Navigation Satellite Systems (GNSS) such as GPS.[29,65,364–368] These systems are crucial in environments where GNSS signals are unavailable, unreliable, or deliberately compromised, such as underground tunnels, underwater, or during wartime. Navigation sensors, or inertial measurement units (IMUs), typically combine accelerometers, gyroscopes, and magnetometers to track motion, orientation, and position relative to Earth's magnetic field. Diamond NV centers can serve as a quantum platform for these applications, offering extraordinary sensitivity to a wide range of physical properties, including magnetic fields, temperature, inertial, and rotational motion. The exceptional precision of these sensors allows for the detection of minute variations in the environment, such as slight changes in magnetic fields or tiny shifts in rotational motion. Therefore, diamond sensors can also be applied in mine detection, submarine navigation, and other security-related applications.

This section highlights recent advancements in the integration of diamond quantum sensors into aerospace and military

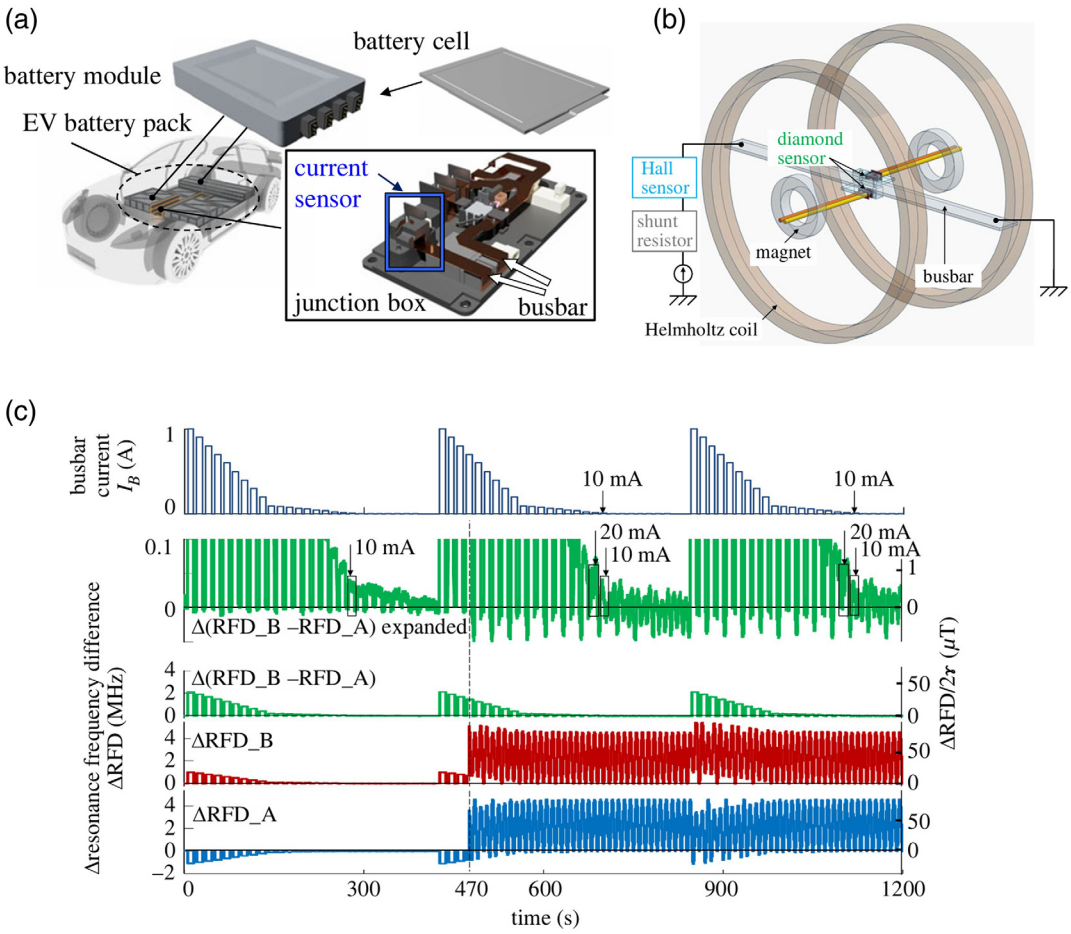

Fig. 27 Battery monitoring in electric vehicles (EVs) using compact diamond sensors. (a), (b) Schematics of compact diamond sensors mounted in the busbar of an EV battery module. (a) Adapted and modified with permission from Ref. 395; © 2022 The Authors. (b) Adapted and modified with permission from Ref. 362; © 2023 The Authors. (c) Busbar current and differential measurements of magnetic fields detected by two diamond sensors. Adapted and modified with permission from Ref. 362; © 2023 The Authors.

technologies. These innovations encompass inertial sensors that measure time-varying magnetic or strain fields induced by mechanical motion, gyroscopes capable of detecting rotational pseudo-magnetic fields generated by rotating nuclear spins, and magnetometers used for mapping magnetic fields in complex outdoor environments or detecting hidden magnetic objects.

4.4.1 Inertial sensors

Inertial sensing involves the measurement of force, acceleration, or displacement. Two primary methods for sensing inertial motion with diamond NV centers are detecting external magnetic fields or internal strain fields induced by the motion of mechanical oscillators. For example, the oscillatory motion of a magnetized AFM tip generates a time-varying magnetic field.[396] This magnetic field drives spin transitions in the NV centers, which can be detected using NV's AC sensing protocols. In this approach, both driven and Brownian motions of the AFM resonator have been detected with a precision of less than 6 picometers under ambient room temperature conditions.[396]

On the other hand, NV centers are also sensitive to strain fields through spin-lattice interaction. For instance, Ovartchaiyapong et al.[31] demonstrated strain-mediated coupling between a diamond cantilever and an embedded NV center, quantitatively characterizing both axial and transverse strain sensitivities. With a strain sensitivity of 3×10^{-6} strain/$\mathrm{Hz}^{1/2}$, they were able to detect ~7 nm motion within a 1-s measurement. These measurements highlight the potential of inertial sensing, whether through spin coupling to time-varying external magnetic fields or by detecting internal strain fields.

Figure 29(a) illustrates a concept for force sensing using diamond nanopillars with NV centers positioned at two different locations: one at the tip of the nanopillar and the other at the base.[29] The NV center at the tip measures the spin-magnetic response caused by the nanopillar's motion under a strong transverse magnetic field gradient, whereas the NV center at the base measures the stress and strain induced by the same mechanical motion. Each method offers distinct advantages and limitations. Magnetic sensitivity is significantly higher than strain sensitivity as evidenced by the measured displacements in the picometer and nanometer range.[31] However, calculations from Ref. 29 suggest that spin-magnetic coupling requires large field gradients (e.g., $\gtrsim$30 mT/μm), presenting practical challenges, such as the need to position nanoferromagnetic structures close to the tip, which limits the range of mechanical motion. Consequently,

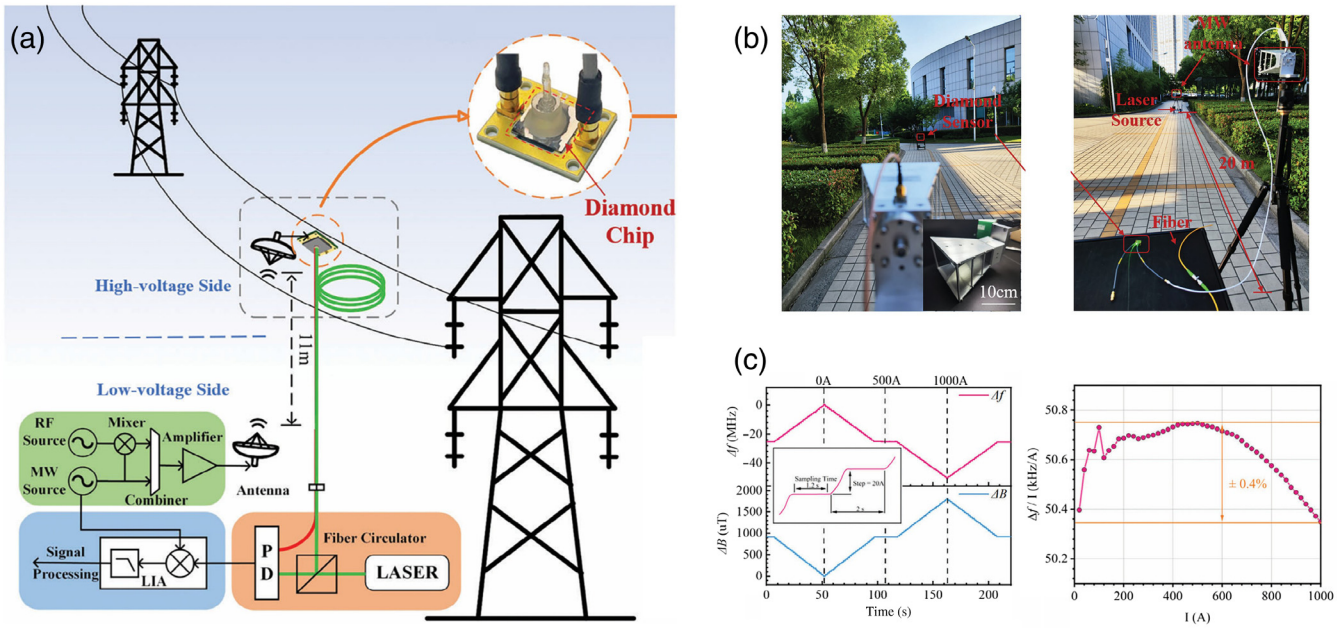

Fig. 28 Current sensors in the high-voltage grids of power network systems. (a) Schematic of diamond sensors for high-voltage grids in power network systems. (b) Photographs of remote diamond sensor system. Directional antennas are used to transmit microwave drive for the sensor. (c) Current measurements with controlling the cable current. Images are adapted and modified with permission from Ref. 363; © 2024 The Authors.

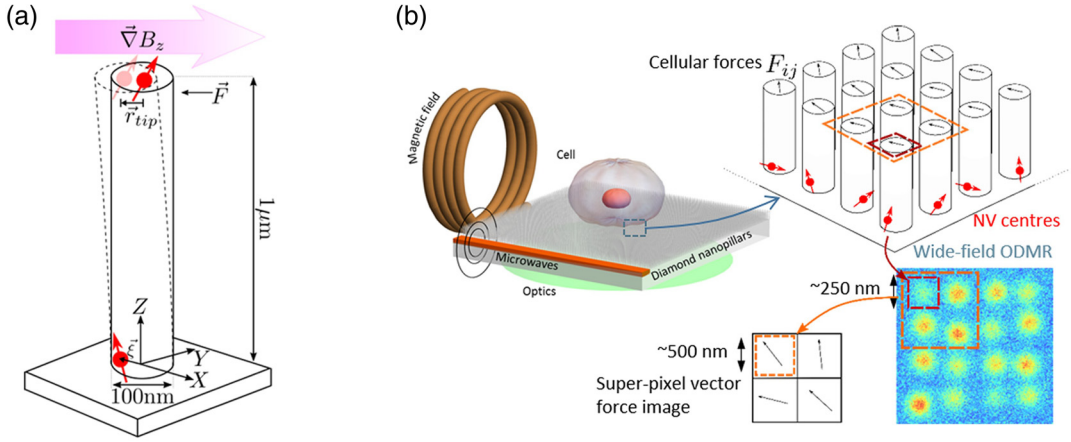

Fig. 29 Inertial sensors based on diamond NV centers. (a) Schematic of a diamond nanopillar with two NV centers located at the tip and base of the nanopillar. The former NV is used to detect inertial force via magnetic field gradient, while the latter probes strain field induced by the internal force. (b) Schematic of inertial force sensor using an array of diamond nanopillars. Images are adapted and modified with permission from Ref. 29; © 2017 American Chemical Society.

both methods may need to be employed together to obtain complementary inertial data, depending on the scale of the motion.

Figure 29(b) presents a concept for force sensing based on arrays of diamond nanopillars, capable of detecting forces induced by biological cells through spin–strain coupling.[29] This approach can also be adapted for navigation applications. Recent advancements in diamond nanofabrication have enabled the development of various diamond nanomechanical structures with high mechanical quality factors. By combining nanofabrication techniques with advanced sensing protocols, the inertial sensitivity of these devices can be significantly enhanced.

4.4.2 Rotation sensors: gyroscope

Alongside inertial sensing, rotation sensing or gyroscopes are essential components for navigation and IMU systems. The fundamental mechanisms of rotation sensing based on NV centers can

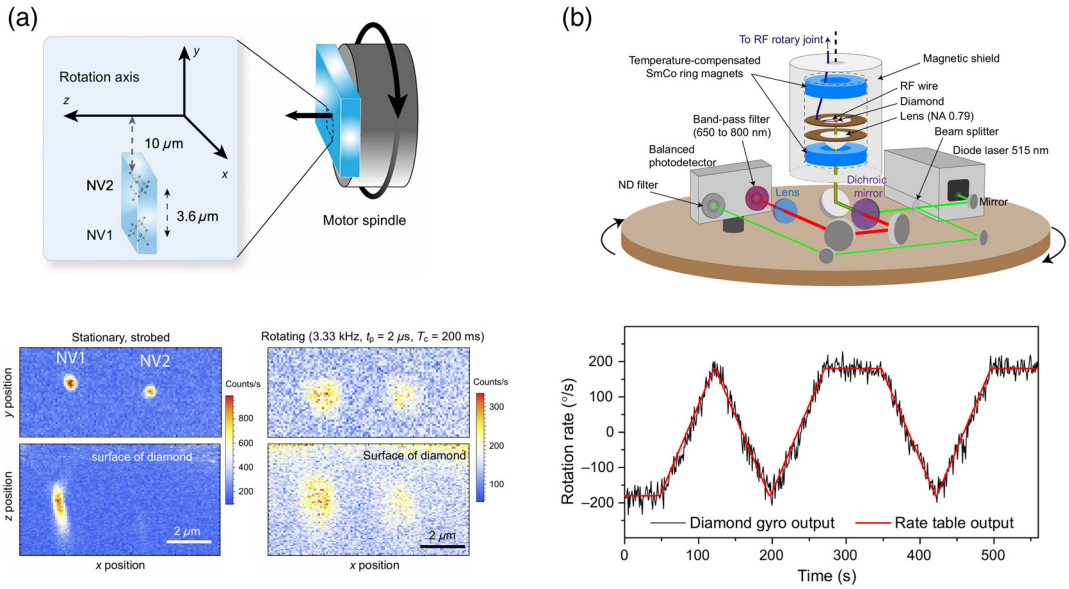

Fig. 30 Gyroscopes using electron and nuclear spins in diamond. (a) Stroboscopic imaging of NV centers in a rotating diamond. Adapted and modified with permission from Ref. 367; © 2018 The Authors. (b) Rotation detection with NV centers using rotational pseudo-magnetic fields generated by rotating nuclear spins. Adapted and modified with permission from Ref. 65; © 2021 The Authors.

be categorized into two main approaches: directly monitoring the rotational motion of the NV electron spin or sensing the effective magnetic field generated by rotating nuclear spins.[64–67,397] For instance, Fig. 30(a) demonstrates stroboscopic imaging of NV centers in a rotating diamond, where the laser and MW fields are relatively stationary.[367] The fluorescence from a rotating NV center is collected by applying synchronized laser and MW pulses that match the rotational period of a spindle driven by an electric motor. This technique enables the detection of rapid rotations, e.g., 200,000 r/min, using a single NV center. Further experiments show that the phase shift of the NV center, induced by the relative motion between a fixed external MW field and the rotating NV spin, can be precisely measured.[397] The external MW field, in combination with the rotating NV center, generates geometric or Berry phases in the NV's Bloch sphere. The accumulated phase can then be detected using spin Hahn echo protocols.

Another approach leverages nuclear spins near the NV center. This method exploits nuclear spins as effective generators of magnetic fields due to rotation, known as rotational pseudo-fields.[368] The NV center serves as a sensing qubit to probe these magnetic fields using AC sensing protocols. In a rotating frame, a precessing nuclear spin generates an effective magnetic field, B, which is determined by the precession frequency, Ω, and the spin gyromagnetic ratio, γ, such that $B = \Omega/\gamma$. As the gyromagnetic ratio of nuclear spins is ~1000 times smaller than that of electron spins, nuclear spins can generate significantly larger rotational pseudo-fields.[368] The ^{14}N and ^{15}N nuclear spins associated with NV centers are utilized for nuclear spin gyroscopes, with an example system illustrated in Fig. 30(b).[65] In this system, both the diamond sensor and control components (including laser, MW source, and detector) are mounted on the spindle and rotate together. Double quantum (DQ) pulse protocols, such as DQ Ramsey and DQ echo, are employed to monitor nuclear spin precession while minimizing the effects of temperature fluctuations. Recent experiments have demonstrated sensitivities in the range of 1 to 1000 deg/(s Hz$^{1/2}$), with the best sensitivity being 4.7 deg/(s Hz$^{1/2}$) and a bias stability of 0.4 deg/s.[65]

4.4.3 Mapping magnetic fields and detecting hidden targets

One important military application of diamond quantum sensors is the mapping of Earth's magnetic fields, which is vital for navigation, geophysical surveillance, and detecting concealed targets.[364] Mapping the Earth's magnetic field or identifying magnetic anomalies caused by underground magnetic compositions or hidden objects holds significant potential for military use. Miniaturized, portable sensors with high magnetic field sensitivity can be integrated into unmanned aerial vehicles for remote detection of magnetic fields from both the Earth's surface and hidden magnetic objects. This provides a highly effective tool for surveillance and reconnaissance.

Figure 31 illustrates examples of using diamond magnetometers to map magnetic fields from road surfaces and detect concealed magnetic objects.[365,366] The sensor systems are mounted on a vehicle to probe changes in magnetic fields in both indoor and outdoor environments [Fig. 31(a)].[365] In outdoor environments, several factors contribute to the total magnetic field, including Earth's magnetic field, as well as permanent or induced fields from the vehicle and its control units. Using two magnetometers fixed to the vehicle and measuring the vector magnetic fields along 3D coordinates, Graham et al. effectively canceled out the permanent magnetic fields from the vehicle itself, enabling them to measure variations in the Earth's core magnetic field along the vehicle's track.[365]

On the other hand, miniaturized diamond sensors, integrated with a 2D scanning stage, are used to image stray magnetic fields from various sizes of magnets embedded in a toy diorama, as shown in Fig. 31(b).[366] This setup emulates a scenario in

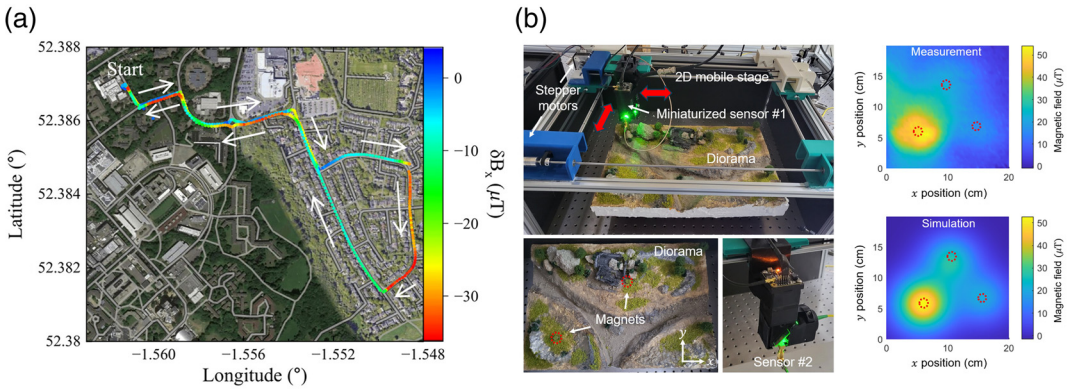

Fig. 31 Mapping magnetic fields from road surfaces and concealed objects. (a) Mapping magnetic fields from road surfaces using diamond sensors mounted in a vehicle. Adapted and modified with permission from Ref. 365; © 2025 Elsevier B.V. (b) Detecting hidden magnetic objects from magnetic images measured by miniaturized diamond sensors mounted in a 2D scanning stage. Adapted and modified with permission from Ref. 366; © 2025 The Authors.

which remote detection of landmines on a battlefield or concealed objects at construction sites is required. By comparing the measured data with simulations, Choi et al.[366] were able to accurately estimate the location and size of the magnets. In addition, vector magnetometry was proposed to compensate for any relative tilt between the sensor and the target, reducing the uncertainty in determining the target's location from several centimeters to tenths of millimeters.[366]

5 Conclusion

In this review, we provide a comprehensive overview of quantum sensing based on solid-state spin defects, covering the fundamental principles as well as recent progress toward realizing practical use cases. We discussed both basic and advanced sensing protocols, imaging applications at two different length scales, the integration with optical devices to enhance optical properties, and ongoing efforts toward practical applications for real-world use.

Solid-state spin defects have emerged as a promising quantum platform for enhanced metrology tools in various fields, offering several advantages, including sensitivity, robustness, and compactness. The unique ability to engineer spin defects significantly enhances their performance and versatility. The challenges posed by spin defects from the surrounding solid-state environment can be tailored through advanced quantum control techniques that decouple environmental noises from spin defects, as well as by interfacing with micro- and nano-photonic structures that improve optical properties. These efforts to optimize sensitivity, coherence time, and integration with optics further extend the utility of spin defects as quantum sensors.

Although natural atoms or superconductor-based sensors also provide high quantum sensing performances, the ability of spin defects to operate under ambient conditions at room temperature offers an incomparable level of control and scalability for practical sensor applications. Along with NV centers in diamond, which lead defect-based quantum sensing research, alternative materials such as SiC, hBN, GaN, and Si show great promise in expanding quantum sensing capabilities. These materials open new opportunities for applications in CMOS, bio-compatible platforms, and integrated photonic circuits. However, further exploration is necessary to fully characterize their spin properties and optimize quantum coherence to unlock their full potential.

Efforts to advance the practical implementation of quantum sensing in industrial, military, and biomedical applications continue to improve sensing performance, device robustness, and real-time data processing techniques. In the future, the development of miniaturized and portable quantum sensors, fiber-based devices, and chip-integrated systems will be crucial in bridging the gap between experimental research and field-ready systems, facilitated by close interdisciplinary collaboration.[395,398]

Given their maturity and near-term applicability, quantum sensors based on spin defects are expected to be the first widely adopted quantum technology, benefiting our daily lives before large-scale quantum computing and communication technologies arrive.

Disclosures

The authors declare no competing financial interest.

Code and Data Availability

Figures generated in this paper are available upon request from the corresponding author. The other cited data and figures for this review article are available in the corresponding cited publications.

Author Contributions

All the authors contributed to the writing, editing, and review of the paper. In Sec. 2, K.K. mainly wrote the paper, and J.S.M. and J.H.L. wrote Sec. 2.5. J.S.M. mainly wrote Sec. 3, and J.-H.K. edited the section. D.L. (Dongkwon Lee) and D.L. (Donghun Lee) mainly wrote and edited Sec. 4. Y.L., C.P., and J.C. reviewed and contributed to the writing of Secs. 2 and 4. D.L. (Donghun Lee) and J.-H.K. supervised and edited the paper.

Acknowledgments

K.K., D.L. (Dongkwon Lee), Y.L., C.P., J.C., and D.L. (Donghun Lee) acknowledge support from the National Research Foundation of Korea (Grant No. NRF-2022M3K4A1094777), the Institute for Information & Communication Technology

Planning & Evaluation (IITP) grant (Grant No. RS-2023-00230717), the Information Technology Research Center (ITRC) support program (Grant No. IITP-2024-2020-0-01606), and the Creation of the Quantum Information Science R&D Ecosystem (Grant No. 2022M3H3A106307411) through the National Research Foundation of Korea, funded by the Korean government (Ministry of Science and ICT). J.S.M. acknowledges support from the IITP, funded by the Korean government (MSIT) (Grant No. RS-2022-II220897, "Development of quantum imaging system for sub-shot-noise microscopy"); J.H.L. and J.-H.K. acknowledge support from the National Research Foundation of Korea (Grant Nos. NRF-2022R1A2C2003176 and 2022M3H4A1A04096396), the ITRC support program (Grant Nos. IITP-2025-RS-2020-II201606 and RS-2023-00259676), and the UNIST 2025 Research Fund (Grant No. 1.250007.01).

References

1. C. L. Degen, F. Reinhard, and P. Cappellaro, "Quantum sensing," *Rev. Mod. Phys.* **89**(3), 035002 (2017).
2. L. Davidovich, "Quantum sensing: beyond the classical limits of precision," arXiv:2401.13658v1 (2024).
3. G. Wolfowicz et al., "Quantum guidelines for solid-state spin defects," *Nat. Rev. Mater.* **6**(10), 906–925 (2021).
4. L. Du Preez, *Electron Paramagnetic Resonance and Optical Investigations of Defect Centres in Diamond*, University of the Witwatersrand, Johannesburg (1965).
5. J. H. N. Loubser and J. A. van Wyk, "Electron spin resonance in the study of diamond," *Rep. Prog. Phys.* **41**(8), 1201 (1978).
6. K. Iakoubovskii, G. J. Adriaenssens, and M. Nesladek, "Photochromism of vacancy-related centres in diamond," *J. Phys. Condens. Matter* **12**(2), 189 (2000).
7. L. C. Bassett et al., "Quantum defects by design," *Nanophotonics* **8**(11), 1867–1888 (2019).
8. M. Atatüre et al., "Material platforms for spin-based photonic quantum technologies," *Nat. Rev. Mater.* **3**(5), 38–51 (2018).
9. S. Danilin and M. Weides, "Quantum sensing with superconducting circuits," arXiv:2103.11022v1 (2021).
10. P. Dutta et al., "A decade of advancement of quantum sensing and metrology in India using cold atoms and ions," *J. Indian Inst. Sci.* **103**(2), 609–632 (2023).
11. J. L. Webb et al., "Nanotesla sensitivity magnetic field sensing using a compact diamond nitrogen-vacancy magnetometer," *Appl. Phys. Lett.* **114**(23), 231103 (2019).
12. Y. Kainuma et al., "Compact and stable diamond quantum sensors for wide applications," *Adv. Quantum Technol.* **7**, 2300456 (2024).
13. J. M. Taylor et al., "High-sensitivity diamond magnetometer with nanoscale resolution," *Nat. Phys.* **4**(10), 810–816 (2008).
14. T. Wolf et al., "Subpicotesla diamond magnetometry," *Phys. Rev. X* **5**(4), 041001 (2015).
15. S. Zhang, K. Bian, and Y. Jiang, "Perspective: nanoscale electric sensing and imaging based on quantum sensors," *Quantum Front.* **2**(1), 19 (2023).
16. P. Maletinsky et al., "A robust scanning diamond sensor for nanoscale imaging with single nitrogen-vacancy centres," *Nat. Nanotechnol.* **7**(5), 320–324 (2012).
17. Y. Xu, W. Zhang, and C. Tian, "Recent advances on applications of NV—magnetometry in condensed matter physics," *Photonics Res.* **11**(3), 393–412 (2023).
18. S. Esmaeili et al., "Evolution of quantum spin sensing: from bench-scale ODMR to compact integrations," *APL Mater.* **12**(4), 040901 (2024).
19. L. Rondin et al., "Magnetometry with nitrogen-vacancy defects in diamond," *Rep. Prog. Phys.* **77**(5), 056503 (2014).
20. J. Wrachtrup et al., "Optical detection of magnetic resonance in a single molecule," *Nature* **363**(6426), 244–245 (1993).
21. V. M. Acosta et al., "Temperature dependence of the nitrogen-vacancy magnetic resonance in diamond," *Phys. Rev. Lett.* **104**(7), 070801 (2010).
22. V. M. Acosta et al., "Erratum: Temperature dependence of the nitrogen-vacancy magnetic resonance in diamond [Phys. Rev. Lett. 104, 070801 (2010)]," *Phys. Rev. Lett.* **106**(20), 209901 (2011).
23. M. W. Doherty et al., "Temperature shifts of the resonances of the NV^- center in diamond," *Phys. Rev. B* **90**(4), 041201 (2014).
24. M. Fujiwara et al., "Real-time nanodiamond thermometry probing in vivo thermogenic responses," *Sci. Adv.* **6**(37), eaba9636c (2020).
25. G. Kucsko et al., "Nanometre-scale thermometry in a living cell," *Nature* **500**(7460), 54–58 (2013).
26. P. Neumann et al., "High-precision nanoscale temperature sensing using single defects in diamond," *Nano Lett.* **13**(6), 2738–2742 (2013).
27. D. M. Toyli et al., "Fluorescence thermometry enhanced by the quantum coherence of single spins in diamond," *Proc. Natl. Acad. Sci. U. S. A.* **110**(21), 8417–8421 (2013).
28. D. A. Simpson et al., "Non-neurotoxic nanodiamond probes for intraneuronal temperature mapping," *ACS Nano* **11**(12), 12077–12086 (2017).
29. M. S. J. Barson et al., "Nanomechanical sensing using spins in diamond," *Nano Lett.* **17**(3), 1496–1503 (2017).
30. D. A. Broadway et al., "Microscopic imaging of the stress tensor in diamond using in situ quantum sensors," *Nano Lett.* **19**(7), 4543–4550 (2019).
31. P. Ovartchaiyapong et al., "Dynamic strain-mediated coupling of a single diamond spin to a mechanical resonator," *Nat. Commun.* **5**, 4429 (2014).
32. F. Dolde et al., "Nanoscale detection of a single fundamental charge in ambient conditions using the NV^- center in diamond," *Phys. Rev. Lett.* **112**(9), 097603 (2014).
33. F. Dolde et al., "Electric-field sensing using single diamond spins," *Nat. Phys.* **7**(6), 459–463 (2011).
34. Z. Qiu et al., "Nanoscale electric field imaging with an ambient scanning quantum sensor microscope," *NPJ Quantum Inf.* **8**(1), 107 (2022).
35. J. R. Maze et al., "Nanoscale magnetic sensing with an individual electronic spin in diamond," *Nature* **455**(7213), 644–647 (2008).
36. L. Rondin et al., "Stray-field imaging of magnetic vortices with a single diamond spin," *Nat. Commun.* **4**, 2279 (2013).
37. J. P. Tetienne et al., "Nanoscale imaging and control of domain-wall hopping with a nitrogen-vacancy center microscope," *Science* **344**(6190), 1366–1369 (2014).
38. M. Pelliccione et al., "Scanned probe imaging of nanoscale magnetism at cryogenic temperatures with a single-spin quantum sensor," *Nat. Nanotechnol.* **11**(8), 700–705 (2016).
39. L. Thiel et al., "Quantitative nanoscale vortex imaging using a cryogenic quantum magnetometer," *Nat. Nanotechnol.* **11**(8), 677–681 (2016).
40. B. J. Maertz et al., "Vector magnetic field microscopy using nitrogen vacancy centers in diamond," *Appl. Phys. Lett.* **96**(9), 092504 (2010).
41. J. D. A. Wood et al., "Microwave-free nuclear magnetic resonance at molecular scales," *Nat. Commun.* **8**(1), 15950 (2017).
42. L. M. Pham et al., "Magnetic field imaging with nitrogen-vacancy ensembles," *New J. Phys.* **13**, 045021 (2011).
43. G. Q. Wang et al., "Nanoscale vector AC magnetometry with a single nitrogen-vacancy center in diamond," *Nano Lett.* **21**(12), 5143–5150 (2021).
44. N. Zhao et al., "Atomic-scale magnetometry of distant nuclear spin clusters via nitrogen-vacancy spin in diamond," *Nat. Nanotechnol.* **6**(4), 242–246 (2011).

45. N. Zhao et al., "Sensing single remote nuclear spins," *Nat. Nanotechnol.* **7**(10), 657–662 (2012).
46. T. H. Taminiau et al., "Detection and control of individual nuclear spins using a weakly coupled electron spin," *Phys. Rev. Lett.* **109**(13), 137602 (2012).
47. M. Loretz et al., "Nanoscale nuclear magnetic resonance with a 1.9-nm-deep nitrogen-vacancy sensor," *Appl. Phys. Lett.* **104**(3), 033102 (2014).
48. A. O. Sushkov et al., "Magnetic resonance detection of individual proton spins using quantum reporters," *Phys. Rev. Lett.* **113**(19), 197601 (2014).
49. S. J. DeVience et al., "Nanoscale NMR spectroscopy and imaging of multiple nuclear species," *Nat. Nanotechnol.* **10**(2), 129–134 (2015).
50. D. Rugar et al., "Proton magnetic resonance imaging using a nitrogen-vacancy spin sensor," *Nat. Nanotechnol.* **10**(2), 120–124 (2015).
51. P. Kehayias et al., "Solution nuclear magnetic resonance spectroscopy on a nanostructured diamond chip," *Nat. Commun.* **8**, 188 (2017).
52. D. R. Glenn et al., "High-resolution magnetic resonance spectroscopy using a solid-state spin sensor," *Nature* **555**(7696), 351–354 (2018).
53. R. D. Allert, K. D. Briegel, and D. B. Bucher, "Advances in nano- and microscale NMR spectroscopy using diamond quantum sensors," *Chem. Commun.* **58**, 8165–8181 (2022).
54. A. Laraoui et al., "High-resolution correlation spectroscopy of ^{13}C spins near a nitrogen-vacancy centre in diamond," *Nat. Commun.* **4**, 1651 (2013).
55. H. J. Mamin et al., "Nanoscale nuclear magnetic resonance with a nitrogen-vacancy spin sensor," *Science* **339**(6119), 557–560 (2013).
56. L. M. Pham et al., "NMR technique for determining the depth of shallow nitrogen-vacancy centers in diamond," *Phys. Rev. B* **93**(4), 045425 (2016).
57. I. Lovchinsky et al., "Nuclear magnetic resonance detection and spectroscopy of single proteins using quantum logic," *Science* **351**(6275), 836–841 (2016).
58. T. Staudacher et al., "Nuclear magnetic resonance spectroscopy on a $(5\text{-nanometer})^3$ sample volume," *Science* **339**(6119), 561–563 (2013).
59. T. Staudacher et al., "Probing molecular dynamics at the nanoscale via an individual paramagnetic centre," *Nat. Commun.* **6**, 8527 (2015).
60. F. Z. Shi et al., "Single-protein spin resonance spectroscopy under ambient conditions," *Science* **347**(6226), 1135–1138 (2015).
61. K. S. Liu et al., "Surface NMR using quantum sensors in diamond," *Proc. Natl. Acad. Sci. U. S. A.* **119**(5), e2111607119 (2022).
62. S. Kolkowitz et al., "Sensing distant nuclear spins with a single electron spin," *Phys. Rev. Lett.* **109**(13), 137601 (2012).
63. M. W. Doherty et al., "Electronic properties and metrology applications of the diamond NV^- center under pressure," *Phys. Rev. Lett.* **112**(4), 047601 (2014).
64. A. Ajoy and P. Cappellaro, "Stable three-axis nuclear-spin gyroscope in diamond," *Phys. Rev. A* **86**(6), 062104 (2012).
65. A. Jarmola et al., "Demonstration of diamond nuclear spin gyroscope," *Sci. Adv.* **7**(43), eabl3840 (2021).
66. G. Wang et al., "Emulated nuclear spin gyroscope with ^{15}N-V centers in diamond," *Phys. Rev. Appl.* **22**(4), 044016 (2024).
67. V. V. Soshenko et al., "Nuclear spin gyroscope based on the nitrogen vacancy center in diamond," *Phys. Rev. Lett.* **126**(19), 197702 (2021).
68. J. Happacher et al., "Temperature-dependent photophysics of single NV centers in diamond," *Phys. Rev. Lett.* **131**(8), 086904 (2023).
69. G. Q. Liu et al., "Coherent quantum control of nitrogen-vacancy center spins near 1000 kelvin," *Nat. Commun.* **10**, 1344 (2019).
70. P. J. Scheidegger et al., "Scanning nitrogen-vacancy magnetometry down to 350 mK," *Appl. Phys. Lett.* **120**(22), 224001 (2022).
71. D. M. Toyli et al., "Measurement and control of single nitrogen-vacancy center spins above 600 K," *Phys. Rev. X* **2**(3), 031001 (2012).
72. P. Bhattacharyya et al., "Imaging the Meissner effect in hydride superconductors using quantum sensors," *Nature* **627**, 73–79 (2024).
73. A. Hilberer et al., "Enabling quantum sensing under extreme pressure: nitrogen-vacancy magnetometry up to 130 GPa," *Phys. Rev. B* **107**(22), L220102 (2023).
74. S. Hsieh et al., "Imaging stress and magnetism at high pressures using a nanoscale quantum sensor," *Science* **366**(6471), 1349–1354 (2019).
75. M. Lesik et al., "Magnetic measurements on micrometer-sized samples under high pressure using designed NV centers," *Science* **366**(6471), 1359–1362 (2019).
76. M. Q. Wang et al., "Imaging magnetic transition of magnetite to megabar pressures using quantum sensors in diamond anvil cell," *Nat. Commun.* **15**(1), 8843 (2024).
77. R. Schirhagl et al., "Nitrogen-vacancy centers in diamond: nanoscale sensors for physics and biology," *Annu. Rev. Phys. Chem.* **65**, 83–105 (2014).
78. M. W. Doherty et al., "The nitrogen-vacancy colour centre in diamond," *Phys. Rep.* **528**(1), 1–45 (2013).
79. J.-P. Tetienne et al., "Magnetic-field-dependent photodynamics of single NV defects in diamond: an application to qualitative all-optical magnetic imaging," *New J. Phys.* **14**(10), 103033 (2012).
80. K. Y. Han et al., "Dark state photophysics of nitrogen–vacancy centres in diamond," *New J. Phys.* **14**(12), 123002 (2012).
81. B. J. M. Hausmann et al., "Single-color centers implanted in diamond nanostructures," *New J. Phys.* **13**(4), 045004 (2011).
82. J. F. Barry et al., "Sensitivity optimization for NV-diamond magnetometry," *Rev. Mod. Phys.* **92**(1), 015004 (2020).
83. M. Lee et al., "Atomic scale magnetic sensing and imaging based on diamond NV centers," in *Magnetometers - Fundamentals and Applications of Magnetism*, S. Curilef, Ed., IntechOpen (2019).
84. A. Dréau et al., "Avoiding power broadening in optically detected magnetic resonance of single NV defects for enhanced DC magnetic field sensitivity," *Phys. Rev. B* **84**(19), 195204 (2011).
85. N. Aslam et al., "Quantum sensors for biomedical applications," *Nat. Rev. Phys.* **5**(3), 157–169 (2023).
86. J. P. Tetienne et al., "Spin relaxometry of single nitrogen-vacancy defects in diamond nanocrystals for magnetic noise sensing," *Phys. Rev. B* **87**(23), 235436 (2013).
87. A. Jarmola et al., "Temperature- and magnetic-field-dependent longitudinal spin relaxation in nitrogen-vacancy ensembles in diamond," *Phys. Rev. Lett.* **108**(19), 197601 (2012).
88. G. Q. Yan et al., "Coherent driving of a single nitrogen vacancy center by a resonant magnetic tunnel junction," *Nano Lett.* **24**(45), 14273–14278 (2024).
89. I. Bertelli et al., "Magnetic resonance imaging of spin-wave transport and interference in a magnetic insulator," *Sci. Adv.* **6**(46), eabd3556 (2020).
90. M. Loretz, T. Rosskopf, and C. L. Degen, "Radio-frequency magnetometry using a single electron spin," *Phys. Rev. Lett.* **110**(1), 017602 (2013).
91. D. H. Slichter et al., "Measurement-induced qubit state mixing in circuit QED from up-converted dephasing noise," *Phys. Rev. Lett.* **109**(15), 153601 (2012).
92. P. London et al., "Detecting and polarizing nuclear spins with double resonance on a single electron spin," *Phys. Rev. Lett.* **111**(6), 067601 (2013).
93. F. Kong et al., "Kilohertz electron paramagnetic resonance spectroscopy of single nitrogen centers at zero magnetic field," *Sci. Adv.* **6**(22), eaaz8244 (2020).
94. F. Kong et al., "Nanoscale zero-field electron spin resonance spectroscopy," *Nat. Commun.* **9**(1), 1563 (2018).

95. K. Kim et al., "Suppression of spin-bath and low-frequency noise for submegahertz ac magnetometry based on a doubly dressed spin qubit in diamond," *Phys. Rev. Appl.* **23**(6), 064004 (2025).
96. A. Stark et al., "Narrow-bandwidth sensing of high-frequency fields with continuous dynamical decoupling," *Nat. Commun.* **8**, 1105 (2017).
97. Z. Y. Hu et al., "Four-order power reduction in nanoscale electron-nuclear double resonance with a nitrogen-vacancy center in diamonds," *Nano Lett.* **24**(9), 2846–2852 (2024).
98. E. L. Hahn, "Spin echoes," *Phys. Rev.* **80**(4), 580–594 (1950).
99. M. A. Ali Ahmed, G. A. Álvarez, and D. Suter, "Robustness of dynamical decoupling sequences," *Phys. Rev. A* **87**(4), 042309 (2013).
100. A. M. Souza, G. A. Álvarez, and D. Suter, "Effects of time-reversal symmetry in dynamical decoupling," *Phys. Rev. A* **85**(3), 032306 (2012).
101. J. Choi et al., "Robust dynamic Hamiltonian engineering of many-body spin systems," *Phys. Rev. X* **10**(3), 031002 (2020).
102. N. Bar-Gill et al., "Solid-state electronic spin coherence time approaching one second," *Nat. Commun.* **4**, 1743 (2013).
103. G. de Lange et al., "Single-spin magnetometry with multipulse sensing sequences," *Phys. Rev. Lett.* **106**(8), 080802 (2011).
104. J. Yoon et al., "Characterization and correction of the pulse width effects on quantum sensing experiments using solid-state spin qubits," *Curr. Appl. Phys.* **50**, 140–144 (2023).
105. Z. Kazi et al., "Direct measurement of DNA bending by quantum magnetic imaging of a nanomechanical torque balance," *Phys. Rev. Appl.* **22**(6), 064044 (2024).
106. M. H. Levitt, "Composite pulses," *Prog. Nucl. Magn. Reson. Spectrosc.* **18**(2), 61–122 (1986).
107. Y. Zhang et al., "Robust quantum control for the manipulation of solid-state spins," *Phys. Rev. Appl.* **19**(3), 034068 (2023).
108. M. Loretz et al., "Spurious harmonic response of multipulse quantum sensing sequences," *Phys. Rev. X* **5**(2), 021009 (2015).
109. Z. Y. Wang, J. Casanova, and M. B. Plenio, "Enhancing the robustness of dynamical decoupling sequences with correlated random phases," *Symmetry* **12**(5), 730 (2020).
110. N. Aslam et al., "Nanoscale nuclear magnetic resonance with chemical resolution," *Science* **357**(6346), 67–71 (2017).
111. M. Pfender et al., "Nonvolatile nuclear spin memory enables sensor-unlimited nanoscale spectroscopy of small spin clusters," *Nat. Commun.* **8**, 834 (2017).
112. J. M. Boss et al., "Quantum sensing with arbitrary frequency resolution," *Science* **356**(6340), 837–840 (2017).
113. S. Schmitt et al., "Submillihertz magnetic spectroscopy performed with a nanoscale quantum sensor," *Science* **356**(6340), 832–837 (2017).
114. S. Zaiser et al., "Enhancing quantum sensing sensitivity by a quantum memory," *Nat. Commun.* **7**, 12279 (2016).
115. J. Meinel et al., "High-resolution nanoscale NMR for arbitrary magnetic fields," *Commun. Phys.* **6**(1), 302 (2023).
116. C. Munuera-Javaloy, A. Tobalina, and J. Casanova, "High-resolution NMR spectroscopy at large fields with nitrogen vacancy centers," *Phys. Rev. Lett.* **130**(13), 133603 (2023).
117. K. S. Cujia et al., "Tracking the precession of single nuclear spins by weak measurements," *Nature* **571**(7764), 230–233 (2019).
118. J. P. Dowling, "Correlated input-port, matter-wave interferometer: quantum-noise limits to the atom-laser gyroscope," *Phys. Rev. A* **57**(6), 4736–4746 (1998).
119. V. Giovannetti, S. Lloyd, and L. Maccone, "Quantum-enhanced measurements: beating the standard quantum limit," *Science* **306**(5700), 1330–1336 (2004).
120. V. Giovannetti, S. Lloyd, and L. Maccone, "Quantum metrology," *Phys. Rev. Lett.* **96**(1), 010401 (2006).
121. H. Lee, P. Kok, and J. P. Dowling, "A quantum Rosetta stone for interferometry," *J. Mod. Opt.* **49**(14–15), 2325–2338 (2002).
122. M. Napolitano et al., "Interaction-based quantum metrology showing scaling beyond the Heisenberg limit," *Nature* **471**(7339), 486–489 (2011).
123. M. Napolitano and M. W. Mitchell, "Nonlinear metrology with a quantum interface," *New J. Phys.* **12**, 093016 (2010).
124. V. Vorobyov et al., "Quantum Fourier transform for nanoscale quantum sensing," *NPJ Quantum Inf.* **7**(1), 124 (2021).
125. B. A. Myers, A. Ariyaratne, and A. C. B. Jayich, "Double-quantum spin-relaxation limits to coherence of near-surface nitrogen-vacancy centers," *Phys. Rev. Lett.* **118**(19), 197201 (2017).
126. I. Fujisaki et al., "Extension of spin dephasing time of continuously excited ensemble nitrogen vacancy centers by double-quantum ramsey magnetometry with spin bath driving," *Phys. Status Solidi A* **221**(8), 2300333 (2024).
127. D. Bluvstein et al., "Extending the quantum coherence of a near-surface qubit by coherently driving the paramagnetic surface environment," *Phys. Rev. Lett.* **123**(14), 146804 (2019).
128. F. A. Freire-Moschovitis et al., "The role of electrolytes in the relaxation of near-surface spin defects in diamond," *ACS Nano* **17**(11), 10474–10485 (2023).
129. C. A. Hart et al., "N-V-diamond magnetic microscopy using a double quantum 4-Ramsey protocol," *Phys. Rev. Appl.* **15**(4), 044020 (2021).
130. H. J. Mamin et al., "Multipulse double-quantum magnetometry with near-surface nitrogen-vacancy centers," *Phys. Rev. Lett.* **113**(3), 030803 (2014).
131. Y. Shen et al., "Detection of quantum signals free of classical noise via quantum correlation," *Phys. Rev. Lett.* **130**(7), 070802 (2023).
132. J. Meinel et al., "Quantum nonlinear spectroscopy of single nuclear spins," *Nat. Commun.* **13**(1), 5318 (2022).
133. B. G. Simon et al., "Filtering and imaging of frequency-degenerate spin waves using nanopositioning of a single-spin sensor," *Nano Lett.* **22**(22), 9198–9204 (2022).
134. B. G. Simon et al., "Directional excitation of a high-density magnon gas using coherently driven spin waves," *Nano Lett.* **21**(19), 8213–8219 (2021).
135. T. X. Zhou et al., "A magnon scattering platform," *Proc. Natl. Acad. Sci. U. S. A.* **118**(25), e2019473118 (2021).
136. F. Casola, T. van der Sar, and A. Yacoby, "Probing condensed matter physics with magnetometry based on nitrogen-vacancy centres in diamond," *Nat. Rev. Mater.* **3**(1), 17088 (2018).
137. S. M. Oliver et al., "Vector magnetic current imaging of an 8 nm process node chip and 3D current distributions using the quantum diamond microscope," in *ISTFA 2021*, pp. 96–107, ASM International (2021).
138. J. Yoon et al., "Exploring the magnetic properties of individual barcode nanowires using wide-field diamond microscopy," *Small* **19**(40), 2304129 (2023).
139. F. Xu et al., "Super-resolution enabled widefield quantum diamond microscopy," *ACS Photonics* **11**(1), 121–127 (2023).
140. H. F. Wen et al., "Imaging electromagnetic boundary of microdevice using a wide field quantum microscope," *Opt. Express* **32**(7), 10829–10840 (2024).
141. P. Welter et al., "Fast scanning nitrogen-vacancy magnetometry by spectrum demodulation," *Phys. Rev. Appl.* **19**(3), 034003 (2023).
142. J. L. Webb et al., "High-speed wide-field imaging of microcircuitry using nitrogen vacancies in diamond," *Phys. Rev. Appl.* **17**(6), 064051 (2022).
143. A. Horsley et al., "Microwave device characterization using a widefield diamond microscope," *Phys. Rev. Appl.* **10**(4), 044039 (2018).
144. G. Balasubramanian et al., "Nanoscale imaging magnetometry with diamond spins under ambient conditions," *Nature* **455**(7213), 648–651 (2008).
145. K. Chang et al., "Nanoscale imaging of current density with a single-spin magnetometer," *Nano Lett.* **17**(4), 2367–2373 (2017).

146. L. Rondin et al., "Nanoscale magnetic field mapping with a single spin scanning probe magnetometer," *Appl. Phys. Lett.* **100**(15), 153118 (2012).
147. U. Celano et al., "Probing magnetic defects in ultra-scaled nanowires with optically detected spin resonance in nitrogen-vacancy center in diamond," *Nano Lett.* **21**(24), 10409–10415 (2021).
148. L. Thiel et al., "Probing magnetism in 2D materials at the nanoscale with single-spin microscopy," *Science* **364**(6444), 973–976 (2019).
149. J.-P. Tetienne et al., "Quantum imaging of current flow in graphene," *Sci. Adv.* **3**(4), e1602429 (2017).
150. I. Gross et al., "Real-space imaging of non-collinear antiferromagnetic order with a single-spin magnetometer," *Nature* **549**(7671), 252–256 (2017).
151. Y. Chen et al., "Simultaneous imaging of magnetic field and temperature using a wide-field quantum diamond microscope," *EPJ Quantum Technol.* **8**(1), 8 (2021).
152. M. Parashar et al., "Sub-second temporal magnetic field microscopy using quantum defects in diamond," *Sci. Rep.* **12**(1), 8743 (2022).
153. L. Basso et al., "Wide-field microwave magnetic field imaging with nitrogen-vacancy centers in diamond," arXiv:2409.16528v1 (2024).
154. L. Shao et al., "Wide-field optical microscopy of microwave fields using nitrogen-vacancy centers in diamonds," *Adv. Opt. Mater.* **4**(7), 1075–1080 (2016).
155. M. Lee et al., "Mapping current profiles of point-contacted graphene devices using single-spin scanning magnetometer," *Appl. Phys. Lett.* **118**(3), 033101 (2021).
156. S. Chen et al., "Current induced hidden states in Josephson junctions," *Nat. Commun.* **15**(1), 8059 (2024).
157. N. Hedrich et al., "Parabolic diamond scanning probes for single-spin magnetic field imaging," *Phys. Rev. Appl.* **14**(6), 064007 (2020).
158. W. S. Huxter et al., "Scanning gradiometry with a single spin quantum magnetometer," *Nat. Commun.* **13**(1), 3761 (2022).
159. W. S. Huxter, F. Dalmagioni, and C. L. Degen, "Multiplexed scanning microscopy with dual-qubit spin sensors," arXiv:2407.19576 (2024).
160. D. R. Glenn et al., "Micrometer-scale magnetic imaging of geological samples using a quantum diamond microscope," *Geochem. Geophys. Geosyst.* **18**(8), 3254–3267 (2017).
161. Z. Y. Du et al., "Widefield diamond quantum sensing with neuromorphic vision sensors," *Adv. Sci.* **11**(2), 2304355 (2024).
162. D. Le Sage et al., "Optical magnetic imaging of living cells," *Nature* **496**(7446), 486–489 (2013).
163. K. Ogawa et al., "Wideband wide-field imaging of spin-wave propagation using diamond quantum sensors," arXiv:2411.17344v2 (2024).
164. J. Yoon et al., "Magnetic steganography based on wide-field diamond quantum microscopy," *Adv. Opt. Mater.* **13**, 2501161 (2025).
165. M. Pfender et al., "Single-spin stochastic optical reconstruction microscopy," *Proc. Natl. Acad. Sci. U. S. A.* **111**(41), 14669–14674 (2014).
166. L.-K. Shan et al., "Super-resolution wide-field quantum sensing," *Appl. Phys. Lett.* **125**(24), 244001 (2024).
167. S. C. Scholten et al., "Aberration control in quantitative wide-field quantum microscopy," *AVS Quantum Sci.* **4**(3), 034404 (2022).
168. K. Arai et al., "Fourier magnetic imaging with nanoscale resolution and compressed sensing speed-up using electronic spins in diamond," *Nat. Nanotechnol.* **10**(10), 859–864 (2015).
169. Z. Z. Guo et al., "Wide-field Fourier magnetic imaging with electron spins in diamond," *NPJ Quantum Inf.* **10**(1), 24 (2024).
170. D. J. McCloskey et al., "Enhanced widefield quantum sensing with nitrogen-vacancy ensembles using diamond nanopillar arrays," *ACS Appl. Mater. Interfaces* **12**(11), 13421–13427 (2020).
171. T. Zhu et al., "Multicone diamond waveguides for nanoscale quantum sensing," *Nano Lett.* **23**(22), 10110–10117 (2023).
172. J. N. Becker et al., "All-optical control of the silicon-vacancy spin in diamond at millikelvin temperatures," *Phys. Rev. Lett.* **120**(5), 053603 (2018).
173. M. Wagner et al., "Electronic structure of the neutral silicon vacancy in 4H and 6H SiC," *Phys. Rev. B* **62**(24), 16555–16560 (2000).
174. S. A. Zargaleh et al., "Evidence for near-infrared photoluminescence of nitrogen vacancy centers in 4H-SiC," *Phys. Rev. B* **94**(6), 060102 (2016).
175. D. J. Christle et al., "Isolated spin qubits in SiC with a high-fidelity infrared spin-to-photon interface," *Phys. Rev. X* **7**(2), 021046 (2017).
176. S. A. Zargaleh et al., "Nitrogen vacancy center in cubic silicon carbide: a promising qubit in the 1.5 μm spectral range for photonic quantum networks," *Phys. Rev. B* **98**(16), 165203 (2018).
177. W. F. Koehl et al., "Room temperature coherent control of defect spin qubits in silicon carbide," *Nature* **479**(7371), 84–87 (2011).
178. D. Simin et al., "All-optical DC nanotesla magnetometry using silicon vacancy fine structure in isotopically purified silicon carbide," *Phys. Rev. X* **6**(3), 031014 (2016).
179. I. Lekavicius et al., "Magnetometry based on silicon-vacancy centers in isotopically purified 4H-SiC," *Phys. Rev. Appl.* **19**(4), 044086 (2023).
180. Q.-Y. Luo et al., "High-sensitivity silicon carbide divacancy-based temperature sensing," *Nanoscale* **15**(18), 8432–8436 (2023).
181. Z. Jiang et al., "Quantum sensing of radio-frequency signal with NV centers in SiC," *Sci. Adv.* **9**(20), eadg2080 (2023).
182. W.-K. Quan et al., "Fiber-integrated silicon carbide silicon-vacancy-based magnetometer," *Opt. Lett.* **48**(6), 1423–1426 (2023).
183. W.-K. Quan et al., "Fiber-coupled silicon carbide divacancy magnetometer and thermometer," *Opt. Express* **31**(10), 15592–15598 (2023).
184. A. B. D. Shaik and P. Palla, "Strain tunable quantum emission from atomic defects in hexagonal boron nitride for telecom-bands," *Sci. Rep.* **12**(1), 21673 (2022).
185. A. Castellanos-Gomez et al., "Deterministic transfer of two-dimensional materials by all-dry viscoelastic stamping," *2D Mater.* **1**(1), 011002 (2014).
186. J. E. Fröch et al., "Photonic nanostructures from hexagonal boron nitride," *Adv. Opt. Mater.* **7**(4), 1801344 (2019).
187. A. Gottscholl et al., "Initialization and read-out of intrinsic spin defects in a van der Waals crystal at room temperature," *Nat. Mater.* **19**(5), 540–545 (2020).
188. R. Gong et al., "Coherent dynamics of strongly interacting electronic spin defects in hexagonal boron nitride," *Nat. Commun.* **14**(1), 3299 (2023).
189. A. Gottscholl et al., "Room temperature coherent control of spin defects in hexagonal boron nitride," *Sci. Adv.* **7**(14), eabf3630 (2021).
190. H. L. Stern et al., "Room-temperature optically detected magnetic resonance of single defects in hexagonal boron nitride," *Nat. Commun.* **13**(1), 618 (2022).
191. H. L. Stern et al., "A quantum coherent spin in hexagonal boron nitride at ambient conditions," *Nat. Mater.* **23**(10), 1379–1385 (2024).
192. A. W. Elshaari et al., "Deterministic integration of hBN emitter in silicon nitride photonic waveguide," *Adv. Quantum Technol.* **4**(6), 2100032 (2021).
193. J. S. Moon et al., "Fiber-integrated van der Waals quantum sensor with an optimal cavity interface," *Adv. Opt. Mater.* **12**(32), 2401987 (2024).
194. M. Huang et al., "Wide field imaging of van der Waals ferromagnet Fe_3GeTe_2 by spin defects in hexagonal boron nitride," *Nat. Commun.* **13**(1), 5369 (2022).

195. A. J. Healey et al., "Quantum microscopy with van der Waals heterostructures," *Nat. Phys.* **19**(1), 87–91 (2023).
196. X. Lyu et al., "Strain quantum sensing with spin defects in hexagonal boron nitride," *Nano Lett.* **22**(16), 6553–6559 (2022).
197. T. Yang et al., "Spin defects in hexagonal boron nitride for strain sensing on nanopillar arrays," *Nanoscale* **14**(13), 5239–5244 (2022).
198. J. Luo et al., "Room temperature optically detected magnetic resonance of single spins in GaN," *Nat. Mater.* **23**(4), 512–518 (2024).
199. J. J. H. Eng et al., "Room-temperature optically detected magnetic resonance of telecom single-photon emitters in GaN," *Phys. Rev. Lett.* **134**(8), 083602 (2025).
200. M. Hollenbach et al., "Wafer-scale nanofabrication of telecom single-photon emitters in silicon," *Nat. Commun.* **13**(1), 7683 (2022).
201. L. Bergeron et al., "Silicon-integrated telecommunications photon-spin interface," *PRX Quantum* **1**(2), 020301 (2020).
202. A. Gruber et al., "Scanning confocal optical microscopy and magnetic resonance on single defect centers," *Science* **276**(5321), 2012–2014 (1997).
203. X. Zhu et al., "Coherent coupling of a superconducting flux qubit to an electron spin ensemble in diamond," *Nature* **478**(7368), 221–224 (2011).
204. S. Johnson et al., "Tunable cavity coupling of the zero phonon line of a nitrogen-vacancy defect in diamond," *New J. Phys.* **17**(12), 122003 (2015).
205. M. H. Abobeih et al., "One-second coherence for a single electron spin coupled to a multi-qubit nuclear-spin environment," *Nat. Commun.* **9**(1), 2552 (2018).
206. P. Neumann et al., "Excited-state spectroscopy of single NV defects in diamond using optically detected magnetic resonance," *New J. Phys.* **11**(1), 013017 (2009).
207. P. C. Maurer et al., "Room-temperature quantum bit memory exceeding one second," *Science* **336**(6086), 1283–1286 (2012).
208. E. Neu et al., "Single photon emission from silicon-vacancy colour centres in chemical vapour deposition nano-diamonds on iridium," *New J. Phys.* **13**(2), 025012 (2011).
209. A. M. Edmonds et al., "Electron paramagnetic resonance studies of silicon-related defects in diamond," *Phys. Rev. B* **77**(24), 245205 (2008).
210. L. J. Rogers et al., "Multiple intrinsically identical single-photon emitters in the solid state," *Nat. Commun.* **5**(1), 4739 (2014).
211. C. Wang et al., "Single photon emission from SiV centres in diamond produced by ion implantation," *J. Phys. B At. Mol. Opt. Phys.* **39**(1), 37 (2005).
212. B. Pingault et al., "Coherent control of the silicon-vacancy spin in diamond," *Nat. Commun.* **8**(1), 15579 (2017).
213. U. F. S. D'Haenens-Johansson et al., "Optical properties of the neutral silicon split-vacancy center in diamond," *Phys. Rev. B* **84**(24), 245208 (2011).
214. B. C. Rose et al., "Observation of an environmentally insensitive solid-state spin defect in diamond," *Science* **361**(6397), 60–63 (2018).
215. Y. Herrmann et al., "Coherent coupling of a diamond tin-vacancy center to a tunable open microcavity," *Phys. Rev. X* **14**(4), 041013 (2024).
216. T. Iwasaki et al., "Tin-vacancy quantum emitters in diamond," *Phys. Rev. Lett.* **119**(25), 253601 (2017).
217. J. Görlitz et al., "Spectroscopic investigations of negatively charged tin-vacancy centres in diamond," *New J. Phys.* **22**(1), 013048 (2020).
218. I. Karapatzakis et al., "Microwave control of the tin-vacancy spin qubit in diamond with a superconducting waveguide," *Phys. Rev. X* **14**(3), 031036 (2024).
219. J. Görlitz et al., "Coherence of a charge stabilised tin-vacancy spin in diamond," *NPJ Quantum Inf.* **8**(1), 45 (2022).
220. T. Iwasaki et al., "Germanium-vacancy single color centers in diamond," *Sci. Rep.* **5**(1), 12882 (2015).
221. R. Høy Jensen et al., "Cavity-enhanced photon emission from a single germanium-vacancy center in a diamond membrane," *Phys. Rev. Appl.* **13**(6), 064016 (2020).
222. M. K. Bhaskar et al., "Quantum nonlinear optics with a germanium-vacancy color center in a nanoscale diamond waveguide," *Phys. Rev. Lett.* **118**(22), 223603 (2017).
223. K. Senkalla et al., "Germanium vacancy in diamond quantum memory exceeding 20 ms," *Phys. Rev. Lett.* **132**(2), 026901 (2024).
224. D. Liu et al., "The silicon vacancy centers in SiC: determination of intrinsic spin dynamics for integrated quantum photonics," *NPJ Quantum Inf.* **10**(1), 72 (2024).
225. P. Udvarhelyi et al., "Vibronic states and their effect on the temperature and strain dependence of silicon-vacancy qubits in 4H-SiC," *Phys. Rev. Appl.* **13**(5), 054017 (2020).
226. N. Morioka et al., "Spin-optical dynamics and quantum efficiency of a single V1 center in silicon carbide," *Phys. Rev. Appl.* **17**(5), 054005 (2022).
227. R. Nagy et al., "High-fidelity spin and optical control of single silicon-vacancy centres in silicon carbide," *Nat. Commun.* **10**(1), 1954 (2019).
228. R. Nagy et al., "Quantum properties of dichroic silicon vacancies in silicon carbide," *Phys. Rev. Appl.* **9**(3), 034022 (2018).
229. C. Babin et al., "Fabrication and nanophotonic waveguide integration of silicon carbide colour centres with preserved spin-optical coherence," *Nat. Mater.* **21**(1), 67–73 (2022).
230. C. Qian et al., "Unveiling the zero-phonon line of the boron vacancy center by cavity-enhanced emission," *Nano Lett.* **22**(13), 5137–5142 (2022).
231. H. Liang et al., "High sensitivity spin defects in hBN created by high-energy He beam irradiation," *Adv. Opt. Mater.* **11**(1), 2201941 (2023).
232. A. Gottscholl et al., "Spin defects in hBN as promising temperature, pressure and magnetic field quantum sensors," *Nat. Commun.* **12**(1), 4480 (2021).
233. D. Zhong et al., "Carbon-related quantum emitter in hexagonal boron nitride with homogeneous energy and 3-fold polarization," *Nano Lett.* **24**(4), 1106–1113 (2024).
234. X. Gao et al., "Nanotube spin defects for omnidirectional magnetic field sensing," *Nat. Commun.* **15**(1), 7697 (2024).
235. N.-J. Guo et al., "Coherent control of an ultrabright single spin in hexagonal boron nitride at room temperature," *Nat. Commun.* **14**(1), 2893 (2023).
236. Y. Chen et al., "Bottom-up synthesis of hexagonal boron nitride nanoparticles with intensity-stabilized quantum emitters," *Small* **17**(17), 2008062 (2021).
237. S. Hong et al., "Nanoscale magnetometry with NV centers in diamond," *MRS Bull.* **38**(2), 155–161 (2013).
238. Y. Chen et al., "Nanodiamond-based optical-fiber quantum probe for magnetic field and biological sensing," *ACS Sens.* **7**(12), 3660–3670 (2022).
239. M. Fujiwara et al., "Highly efficient coupling of photons from nanoemitters into single-mode optical fibers," *Nano Lett.* **11**(10), 4362–4365 (2011).
240. X. Liu et al., "Fiber-integrated diamond-based magnetometer," *Appl. Phys. Lett.* **103**(14), 143105 (2013).
241. S. Maayani et al., "Distributed quantum fiber magnetometry," *Laser Photonics Rev.* **13**(7), 1900075 (2019).
242. M. Fujiwara, "Diamond quantum sensors in microfluidics technology," *Biomicrofluidics* **17**(5), 054107 (2023).
243. M. Barth et al., "Controlled coupling of a single-diamond nanocrystal to a photonic crystal cavity," *Opt. Lett.* **34**(7), 1108–1110 (2009).
244. M. Radulaski et al., "Nanodiamond integration with photonic devices," *Laser Photonics Rev.* **13**(8), 1800316 (2019).
245. K. Ngan et al., "Quantum photonic circuits integrated with color centers in designer nanodiamonds," *Nano Lett.* **23**(20), 9360–9366 (2023).

246. L. W. Russell et al., "Optimizing optical tweezers experiments for magnetic resonance sensing with nanodiamonds," *ACS Photonics* **8**(4), 1214–1221 (2021).
247. S. Kim et al., "Photonic crystal cavities from hexagonal boron nitride," *Nat. Commun.* **9**(1), 2623 (2018).
248. T. Van Der Sar et al., "Nanopositioning of a diamond nanocrystal containing a single nitrogen-vacancy defect center," *Appl. Phys. Lett.* **94**(17), 173104 (2009).
249. A. Stewart et al., "Optical tweezers assembled nanodiamond quantum sensors," *Nano Lett.* **24**(39), 12188–12195 (2024).
250. C. Laube et al., "Controlling the fluorescence properties of nitrogen vacancy centers in nanodiamonds," *Nanoscale* **11**(4), 1770–1783 (2019).
251. W. W.-W. Hsiao et al., "Fluorescent nanodiamond: a versatile tool for long-term cell tracking, super-resolution imaging, and nanoscale temperature sensing," *Acc. Chem. Res.* **49**(3), 400–407 (2016).
252. D. Beke et al., "Room-temperature defect qubits in ultrasmall nanocrystals," *J. Phys. Chem. Lett.* **11**(5), 1675–1681 (2020).
253. Y. A. Alzahrani and M. Alkahtani, "Negatively charged boron-vacancy defect in hexagonal boron nitride nanoparticles," *Appl. Phys. Lett.* **124**(17), 173701 (2024).
254. P. Han et al., "Surface-bound states in nanodiamonds," *Phys. Rev. B* **95**(19), 195428 (2017).
255. S. Stehlik et al., "Size and purity control of HPHT nanodiamonds down to 1 nm," *J. Phys. Chem. C* **119**(49), 27708–27720 (2015).
256. M. Alkahtani et al., "Growth of high-purity low-strain fluorescent nanodiamonds," *ACS Photonics* **6**(5), 1266–1271 (2019).
257. M. E. Trusheim et al., "Scalable fabrication of high purity diamond nanocrystals with long-spin-coherence nitrogen vacancy centers," *Nano Lett.* **14**(1), 32–36 (2014).
258. J. E. March et al., "Long spin coherence and relaxation times in nanodiamonds milled from polycrystalline ^{12}C diamond," *Phys. Rev. Appl.* **20**(4), 044045 (2023).
259. B. D. Wood et al., "Long spin coherence times of nitrogen vacancy centers in milled nanodiamonds," *Phys. Rev. B* **105**(20), 205401 (2022).
260. R. Tsukahara et al., "Removing non-size-dependent electron spin decoherence of nanodiamond quantum sensors by aerobic oxidation," *ACS Appl. Nano Mater.* **2**(6), 3701–3710 (2019).
261. B. R. Smith, D. Gruber, and T. Plakhotnik, "The effects of surface oxidation on luminescence of nano diamonds," *Diam. Relat. Mater.* **19**(4), 314–318 (2010).
262. N. Nunn et al., "Optical and electronic spin properties of fluorescent micro- and nanodiamonds upon prolonged ultrahigh-temperature annealing," *J. Vac. Sci. Technol. B* **41**(4), 042206 (2023).
263. L. Marseglia et al., "Bright nanowire single photon source based on SiV centers in diamond," *Opt. Express* **26**(1), 80–89 (2018).
264. T. M. Babinec et al., "A diamond nanowire single-photon source," *Nat. Nanotechnol.* **5**(3), 195–199 (2010).
265. S. A. Momenzadeh et al., "Nanoengineered diamond waveguide as a robust bright platform for nanomagnetometry using shallow nitrogen vacancy centers," *Nano Lett.* **15**(1), 165–169 (2015).
266. F. Fogliano et al., "Mapping the cavity optomechanical interaction with subwavelength-sized ultrasensitive nanomechanical force sensors," *Phys. Rev. X* **11**(2), 021009 (2021).
267. F. Fogliano et al., "Ultrasensitive nano-optomechanical force sensor operated at dilution temperatures," *Nat. Commun.* **12**(1), 4124 (2021).
268. B. Pigeau et al., "Observation of a phononic Mollow triplet in a multimode hybrid spin-nanomechanical system," *Nat. Commun.* **6**(1), 8603 (2015).
269. S. Meesala et al., "Enhanced strain coupling of nitrogen-vacancy spins to nanoscale diamond cantilevers," *Phys. Rev. Appl.* **5**(3), 034010 (2016).
270. Y.-I. Sohn et al., "Controlling the coherence of a diamond spin qubit through its strain environment," *Nat. Commun.* **9**(1), 2012 (2018).
271. L. T. Sun et al., "Diamond nanorods from carbon nanotubes," *Adv. Mater.* **16**(20), 1849–1853 (2004).
272. Y. Yu, L. Wu, and J. Zhi, "Diamond nanowires: fabrication, structure, properties, and applications," *Angew. Chem. Int. Ed.* **53**(52), 14326–14351 (2014).
273. J. H. Lee et al., "Strong zero-phonon transition from point defect-stacking fault complexes in silicon carbide nanowires," *Nano Lett.* **21**(21), 9187–9194 (2021).
274. K. Zhang et al., "Two dimensional hexagonal boron nitride (2D-hBN): synthesis, properties and applications," *J. Mater. Chem. C* **5**(46), 11992–12022 (2017).
275. J. Fernandes et al., "Room-temperature emitters in wafer-scale few-layer hBN by atmospheric pressure CVD," *FlatChem* **33**, 100366 (2022).
276. H. Anma et al., "Low temperature deposition of SiC thin films on polymer surface by plasma CVD," *Appl. Surf. Sci.* **175–176**, 484–489 (2001).
277. W. C. Hughes et al., "Molecular beam epitaxy growth and properties of GaN films on GaN/SiC substrates," *J. Vac. Sci. Technol. B* **13**(4), 1571–1577 (1995).
278. P. Liaw and R. F. Davis, "Epitaxial growth and characterization of β-SiC thin films," *J. Electrochem. Soc.* **132**(3), 642 (1985).
279. G. Ma et al., "A review on precision polishing technology of single-crystal SiC," *Crystals* **12**(1), 101 (2022).
280. Y. Zhu et al., "Effect and mechanism of oxidant on alkaline chemical mechanical polishing of gallium nitride thin films," *Mater. Sci. Semicond. Process.* **138**, 106272 (2022).
281. S. Hayashi, T. Koga, and M. S. Goorsky, "Chemical mechanical polishing of GaN," *J. Electrochem. Soc.* **155**(2), H113 (2007).
282. A. Faraon et al., "Coupling of nitrogen-vacancy centers to photonic crystal cavities in monocrystalline diamond," *Phys. Rev. Lett.* **109**(3), 033604 (2012).
283. J. Tisler et al., "Fluorescence and spin properties of defects in single digit nanodiamonds," *ACS Nano* **3**(7), 1959–1965 (2009).
284. C. Bradac et al., "Observation and control of blinking nitrogen-vacancy centres in discrete nanodiamonds," *Nat. Nanotechnol.* **5**(5), 345–349 (2010).
285. Q. Wu et al., "Realization of numerical aperture 2.0 using a gallium phosphide solid immersion lens," *Appl. Phys. Lett.* **75**(26), 4064–4066 (1999).
286. E. Ramsay, "Solid immersion lens applications for nanophotonic devices," *J. Nanophotonics* **2**(1), 021854 (2008).
287. L. Hüser et al., "Microsphere assistance in interference microscopy with high numerical aperture objective lenses," *J. Opt. Microsyst.* **2**(04), 044501 (2022).
288. A. Darafsheh, "Microsphere-assisted microscopy," *J. Appl. Phys.* **131**(3), 031102 (2022).
289. H. Yang et al., "Super-resolution imaging of a dielectric microsphere is governed by the waist of its photonic nanojet," *Nano Lett.* **16**(8), 4862–4870 (2016).
290. A. Darafsheh et al., "Advantages of microsphere-assisted super-resolution imaging technique over solid immersion lens and confocal microscopies," *Appl. Phys. Lett.* **104**(6), 061117 (2014).
291. L. Li et al., "Label-free super-resolution imaging of adenoviruses by submerged microsphere optical nanoscopy," *Light Sci. Appl.* **2**(9), e104 (2013).
292. M. Jamali et al., "Microscopic diamond solid-immersion-lenses fabricated around single defect centers by focused ion beam milling," *Rev. Sci. Instrum.* **85**(12), 123703 (2014).
293. L. Marseglia et al., "Nanofabricated solid immersion lenses registered to single emitters in diamond," *Appl. Phys. Lett.* **98**(13), 133107 (2011).

294. F. Sardi et al., "Scalable production of solid-immersion lenses for quantum emitters in silicon carbide," *Appl. Phys. Lett.* **117**(2), 022105 (2020).
295. J. P. Hadden et al., "Strongly enhanced photon collection from diamond defect centers under microfabricated integrated solid immersion lenses," *Appl. Phys. Lett.* **97**(24), 241901 (2010).
296. J. S. Moon et al., "High-resolution, high-contrast optical interface for defect qubits," *ACS Photonics* **8**(9), 2642–2649 (2021).
297. X.-J. Wang et al., "Enhanced brightness of quantum emitters via in situ coupling to the dielectric microsphere," *Appl. Phys. Lett.* **123**(13), 133106 (2023).
298. X. Cheng et al., "Additive GaN solid immersion lenses for enhanced photon extraction efficiency from diamond color centers," *ACS Photonics* **10**(9), 3374–3383 (2023).
299. S.-H. Wu, I. Lekavicius, and H. Wang, "Microsphere-enhanced fluorescence collection for nitrogen vacancy centers in diamond," *Appl. Phys. Lett.* **125**(17), 171109 (2024).
300. T.-Y. Huang et al., "A monolithic immersion metalens for imaging solid-state quantum emitters," *Nat. Commun.* **10**(1), 2392 (2019).
301. F. Yang et al., "A hybrid coupler for directing quantum light emission with high radiative Purcell enhancement to a dielectric metasurface lens," *J. Appl. Phys.* **130**(16), 163103 (2021).
302. Y. Kan and S. I. Bozhevolnyi, "Advances in metaphotonics empowered single photon emission," *Adv. Opt. Mater.* **11**(10), 2202759 (2023).
303. C. Li et al., "Arbitrarily structured quantum emission with a multifunctional metalens," *eLight* **3**(1), 19 (2023).
304. J. Ma et al., "Engineering quantum light sources with flat optics," *Adv. Mater.* **36**(23), 2313589 (2024).
305. T. Schröder et al., "Ultrabright and efficient single-photon generation based on nitrogen-vacancy centres in nanodiamonds on a solid immersion lens," *New J. Phys.* **13**(5), 055017 (2011).
306. S. Park et al., "Fresnel-type solid immersion lens for efficient light collection from quantum defects in diamond," *Opt. Express* **31**(12), 20586–20594 (2023).
307. J. Zhu and L. L. Goddard, "All-dielectric concentration of electromagnetic fields at the nanoscale: the role of photonic nanojets," *Nanoscale Adv.* **1**(12), 4615–4643 (2019).
308. A. Darafsheh et al., "Optical super-resolution by high-index liquid-immersed microspheres," *Appl. Phys. Lett.* **101**(14), 141128 (2012).
309. P. K. Upputuri and M. Pramanik, "Microsphere-aided optical microscopy and its applications for super-resolution imaging," *Opt. Commun.* **404**, 32–41 (2017).
310. L. A. Krivitsky et al., "Locomotion of microspheres for super-resolution imaging," *Sci. Rep.* **3**(1), 3501 (2013).
311. R. Paniagua-Domínguez et al., "A metalens with a near-unity numerical aperture," *Nano Lett.* **18**(3), 2124–2132 (2018).
312. M. Kim et al., "Improving photon gathering efficiency in nitrogen-vacancy centers using transferred metalenses," in *Conf. Lasers and Electro-Opt. Pac. Rim (CLEO-PR)*, Technical Digest Series, Optica Publishing Group (2024).
313. M. Kim et al., "Multilayer all-polymer metasurface stacked on optical fiber via sequential micro-punching process," *Nanophotonics* **12**(13), 2359–2369 (2023).
314. H. Zhang and Z. Guo, "Single mode-fiber scale based square solid immersion metalens for single quantum emitters," *Opt. Mater.* **105**, 109850 (2020).
315. E. Bayati et al., "Inverse designed metalenses with extended depth of focus," *ACS Photonics* **7**(4), 873–878 (2020).
316. M. Khorasaninejad et al., "Multispectral chiral imaging with a metalens," *Nano Lett.* **16**(7), 4595–4600 (2016).
317. C. He et al., "Chiral metalens of circular polarization dichroism with helical surface arrays in mid-infrared region," *Adv. Opt. Mater.* **7**(24), 1901129 (2019).
318. E. M. Purcell, H. C. Torrey, and R. V. Pound, "Resonance absorption by nuclear magnetic moments in a solid," *Phys. Rev.* **69**(1–2), 37–38 (1946).
319. J. Xavier et al., "Quantum nanophotonic and nanoplasmonic sensing: towards quantum optical bioscience laboratories on chip," *Nanophotonics* **10**(5), 1387–1435 (2021).
320. M. K. Bhaskar et al., "Experimental demonstration of memory-enhanced quantum communication," *Nature* **580**(7801), 60–64 (2020).
321. G. Calusine, A. Politi, and D. D. Awschalom, "Cavity-enhanced measurements of defect spins in silicon carbide," *Phys. Rev. Appl.* **6**(1), 014019 (2016).
322. T. Jung et al., "Spin measurements of NV centers coupled to a photonic crystal cavity," *APL Photonics* **4**(12), 120803 (2019).
323. J. E. Fröch et al., "Coupling spin defects in hexagonal boron nitride to monolithic bullseye cavities," *Nano Lett.* **21**(15), 6549–6555 (2021).
324. M. J. Burek et al., "Fiber-coupled diamond quantum nanophotonic interface," *Phys. Rev. Appl.* **8**(2), 024026 (2017).
325. L. Li et al., "Efficient photon collection from a nitrogen vacancy center in a circular bullseye grating," *Nano Lett.* **15**(3), 1493–1497 (2015).
326. N. H. Wan, S. Mouradian, and D. Englund, "Two-dimensional photonic crystal slab nanocavities on bulk single-crystal diamond," *Appl. Phys. Lett.* **112**(14), 141102 (2018).
327. S. W. Ding et al., "Purcell-enhanced emissions from diamond color centers in slow light photonic crystal waveguides," arXiv:2503.01149v1 (2025).
328. H. Hapuarachchi, F. Campaioli, and J. H. Cole, "NV-plasmonics: modifying optical emission of an NV^- center via plasmonic metal nanoparticles," *Nanophotonics* **11**(21), 4919–4927 (2022).
329. H. Hapuarachchi et al., "Plasmonically engineered nitrogen-vacancy spin readout," *Opt. Express* **32**(13), 22352–22361 (2024).
330. H. Guo et al., "Plasmon-enhanced sensitivity of spin-based sensors based on a diamond ensemble of nitrogen vacancy color centers," *Opt. Lett.* **42**(3), 403–406 (2017).
331. J.-Y. Zhou et al., "Plasmonic-enhanced bright single spin defects in silicon carbide membranes," *Nano Lett.* **23**(10), 4334–4343 (2023).
332. X. Xu et al., "Greatly enhanced emission from spin defects in hexagonal boron nitride enabled by a low-loss plasmonic nanocavity," *Nano Lett.* **23**(1), 25–33 (2023).
333. X. Gao et al., "High-contrast plasmonic-enhanced shallow spin defects in hexagonal boron nitride for quantum sensing," *Nano Lett.* **21**(18), 7708–7714 (2021).
334. H. Cai et al., "Spin defects in hBN assisted by metallic nanotrenches for quantum sensing," *Nano Lett.* **23**(11), 4991–4996 (2023).
335. L. Kim et al., "Absorption-based diamond spin microscopy on a plasmonic quantum metasurface," *ACS Photonics* **8**(11), 3218–3225 (2021).
336. S. Kumar, S. K. H. Andersen, and S. I. Bozhevolnyi, "Extremely confined gap-plasmon waveguide modes excited by nitrogen-vacancy centers in diamonds," *ACS Photonics* **6**(1), 23–29 (2019).
337. A. W. Schell et al., "Single defect centers in diamond nanocrystals as quantum probes for plasmonic nanostructures," *Opt. Express* **19**(8), 7914–7920 (2011).
338. J.-P. So et al., "Purcell enhancement and spin spectroscopy of silicon vacancy centers in silicon carbide using an ultrasmall mode-volume plasmonic cavity," *Nano Lett.* **24**(37), 11669–11675 (2024).
339. H. Siampour, S. Kumar, and S. I. Bozhevolnyi, "Chip-integrated plasmonic cavity-enhanced single nitrogen-vacancy center emission," *Nanoscale* **9**(45), 17902–17908 (2017).
340. S. Cui et al., "Hybrid plasmonic photonic crystal cavity for enhancing emission from near-surface nitrogen vacancy centers in diamond," *ACS Photonics* **2**(4), 465–469 (2015).
341. K. Jensen et al., "Cavity-enhanced room-temperature magnetometry using absorption by nitrogen-vacancy centers in diamond," *Phys. Rev. Lett.* **112**(16), 160802 (2014).

342. G. Chatzidrosos et al., "Miniature cavity-enhanced diamond magnetometer," *Phys. Rev. Appl.* **8**(4), 044019 (2017).
343. M. Pallmann et al., "Cavity-mediated collective emission from few emitters in a diamond membrane," *Phys. Rev. X* **14**(4), 041055 (2024).
344. M. Koppenhöfer et al., "Dissipative superradiant spin amplifier for enhanced quantum sensing," *PRX Quantum* **3**(3), 030330 (2022).
345. K.-Y. Kim et al., "Cavity-mediated collective emission from steady-state subradiance," *Nat. Commun.* **16**(1), 6346 (2025).
346. J. F. Barry et al., "Optical magnetic detection of single-neuron action potentials using quantum defects in diamond," *Proc. Natl. Acad. Sci. U. S. A.* **113**(49), 14133–14138 (2016).
347. Z. Y. Yu et al., "Noninvasive magnetocardiography of a living rat based on a diamond quantum sensor," *Phys. Rev. Appl.* **21**(6), 064028 (2024).
348. N. W. Hansen et al., "Microscopic-scale magnetic recording of brain neuronal electrical activity using a diamond quantum sensor," *Sci. Rep.* **13**(1), 12407 (2023).
349. S. Chen et al., "Immunomagnetic microscopy of tumor tissues using quantum sensors in diamond," *Proc. Natl. Acad. Sci. U. S. A.* **119**(5), e2118876119 (2022).
350. T. F. Segawa and R. Igarashi, "Nanoscale quantum sensing with nitrogen-vacancy centers in nanodiamonds—a magnetic resonance perspective," *Prog. Nucl. Magn. Reson. Spectrosc.* **134–135**, 20–38 (2023).
351. D. R. Glenn et al., "Single-cell magnetic imaging using a quantum diamond microscope," *Nat. Methods* **12**(8), 736–738 (2015).
352. J. Smits et al., "Two-dimensional nuclear magnetic resonance spectroscopy with a microfluidic diamond quantum sensor," *Sci. Adv.* **5**(7), eaaw7895 (2019).
353. C. Li et al., "SARS-CoV-2 quantum sensor based on nitrogen-vacancy centers in diamond," *Nano Lett.* **22**(1), 43–49 (2022).
354. B. S. Miller et al., "Spin-enhanced nanodiamond biosensing for ultrasensitive diagnostics," *Nature* **587**(7835), 588–593 (2020).
355. S. E. Crawford et al., "Quantum sensing for energy applications: review and perspective," *Adv. Quantum Technol.* **4**(8), 2100049 (2021).
356. V. J. Borràs et al., "A quantum sensing metrology for magnetic memories," *NPJ Spintron.* **2**(1), 14 (2024).
357. M. J. Turner et al., "Magnetic field fingerprinting of integrated-circuit activity with a quantum diamond microscope," *Phys. Rev. Appl.* **14**(1), 014097 (2020).
358. M. Garsi et al., "Three-dimensional imaging of integrated-circuit activity using quantum defects in diamond," *Phys. Rev. Appl.* **21**(1), 014055 (2024).
359. F. M. Stürner et al., "Integrated and portable magnetometer based on nitrogen-vacancy ensembles in diamond," *Adv. Quantum Technol.* **4**(4), 2000111 (2021).
360. F. M. Stürner et al., "Compact integrated magnetometer based on nitrogen-vacancy centres in diamond," *Diam. Relat. Mater.* **93**, 59–65 (2019).
361. H. Kumar et al., "High dynamic-range and portable magnetometer using ensemble nitrogen-vacancy centers in diamond," *Rev. Sci. Instrum.* **95**(7), 075002 (2024).
362. Y. Hatano et al., "A wide dynamic range diamond quantum sensor as an electric vehicle battery monitor," *Philos. Trans. R. Soc. Math. Phys. Eng. Sci.* **382**(2265), 20220312 (2023).
363. Q. Liu et al., "Fiber-integrated diamond quantum sensor for high-voltage current measurements," *Adv. Sens. Res.* **4**(1), 2400106 (2025).
364. M. Krelina, "Quantum technology for military applications," *EPJ Quantum Technol.* **8**(1), 24 (2021).
365. S. M. Graham et al., "On the road with a diamond magnetometer," *Diam. Relat. Mater.* **152**, 111945 (2025).
366. W. Choi et al., "Scanning miniaturized magnetometer based on diamond quantum sensors and its potential application for hidden target detection," *Sensors* **25**(6), 1866 (2025).
367. A. A. Wood et al., "Quantum measurement of a rapidly rotating spin qubit in diamond," *Sci. Adv.* **4**(5), eaar7691 (2018).
368. A. A. Wood et al., "Magnetic pseudo-fields in a rotating electron–nuclear spin system," *Nat. Phys.* **13**(11), 1070–1073 (2017).
369. D. Lee et al., "Topical review: spins and mechanics in diamond," *J. Opt.* **19**(3), 033001 (2017).
370. C.-F. Liu et al., "Ultra-sensitive hybrid diamond nanothermometer," *Natl. Sci. Rev.* **8**(5), nwaa194 (2021).
371. H. C. Davis et al., "Mapping the microscale origins of magnetic resonance image contrast with subcellular diamond magnetometry," *Nat. Commun.* **9**(1), 131 (2018).
372. J. Zalieckas et al., "Quantum sensing of microRNAs with nitrogen-vacancy centers in diamond," *Commun. Chem.* **7**(1), 101 (2024).
373. P. Wang et al., "Nanoscale magnetic imaging of ferritins in a single cell," *Sci. Adv.* **5**(4), eaau8038 (2019).
374. T. Häberle et al., "Nanoscale nuclear magnetic imaging with chemical contrast," *Nat. Nanotechnol.* **10**(2), 125–128 (2015).
375. F. Ziem et al., "Quantitative nanoscale MRI with a wide field of view," *Sci. Rep.* **9**(1), 12166 (2019).
376. K. D. Briegel et al., "Optical widefield nuclear magnetic resonance microscopy," *Nat. Commun.* **16**(1), 1281 (2025).
377. R. Fischer et al., "Bulk nuclear polarization enhanced at room temperature by optical pumping," *Phys. Rev. Lett.* **111**(5), 057601 (2013).
378. A. Ajoy et al., "Orientation-independent room temperature optical ^{13}C hyperpolarization in powdered diamond," *Sci. Adv.* **4**(5), eaar5492 (2018).
379. N. Arunkumar et al., "Micron-scale NV-NMR spectroscopy with signal amplification by reversible exchange," *PRX Quantum* **2**(1), 010305 (2021).
380. M. H. Abobeih et al., "Atomic-scale imaging of a 27-nuclear-spin cluster using a quantum sensor," *Nature* **576**(7787), 411–415 (2019).
381. J. Zopes et al., "Three-dimensional localization spectroscopy of individual nuclear spins with sub-Angstrom resolution," *Nat. Commun.* **9**(1), 4678 (2018).
382. M. T. Amawi et al., "Three-dimensional magnetic resonance tomography with sub-10 nanometer resolution," *NPJ Quantum Inf.* **10**(1), 16 (2024).
383. F. Bruckmaier et al., "Imaging local diffusion in microstructures using NV-based pulsed field gradient NMR," *Sci. Adv.* **9**(33), eadh3484 (2023).
384. I. Fescenko et al., "Diamond magnetic microscopy of malarial hemozoin nanocrystals," *Phys. Rev. Appl.* **11**(3), 034029 (2019).
385. D. A. Simpson et al., "Electron paramagnetic resonance microscopy using spins in diamond under ambient conditions," *Nat. Commun.* **8**(1), 458 (2017).
386. K. Arai et al., "Millimetre-scale magnetocardiography of living rats with thoracotomy," *Commun. Phys.* **5**(1), 200 (2022).
387. M. Karadas et al., "Feasibility and resolution limits of opto-magnetic imaging of neural network activity in brain slices using color centers in diamond," *Sci. Rep.* **8**(1), 4503 (2018).
388. S. C. Scholten et al., "Imaging current paths in silicon photovoltaic devices with a quantum diamond microscope," *Phys. Rev. Appl.* **18**(1), 014041 (2022).
389. C. Foy et al., "Wide-field magnetic field and temperature imaging using nanoscale quantum sensors," *ACS Appl. Mater. Interfaces* **12**(23), 26525–26533 (2020).
390. A. Kuwahata et al., "Magnetometer with nitrogen-vacancy center in a bulk diamond for detecting magnetic nanoparticles in biomedical applications," *Sci. Rep.* **10**(1), 2483 (2020).
391. R. L. Patel et al., "Subnanotesla magnetometry with a fiber-coupled diamond sensor," *Phys. Rev. Appl.* **14**(4), 044058 (2020).
392. J. Pogorzelski et al., "Compact and fully integrated LED quantum sensor based on NV centers in diamond," *Sensors* **24**(3), 743 (2024).

393. X. Wang et al., "Portable diamond NV magnetometer head integrated with 520 nm diode laser," *IEEE Sens. J.* **22**(6), 5580–5587 (2022).
394. D. Zheng et al., "A hand-held magnetometer based on an ensemble of nitrogen-vacancy centers in diamond," *J. Phys. Appl. Phys.* **53**(15), 155004 (2020).
395. Y. Hatano et al., "High-precision robust monitoring of charge/discharge current over a wide dynamic range for electric vehicle batteries using diamond quantum sensors," *Sci. Rep.* **12**(1), 13991 (2022).
396. S. Kolkowitz et al., "Coherent sensing of a mechanical resonator with a single-spin qubit," *Science* **335**(6076), 1603–1606 (2012).
397. A. A. Wood et al., "Observation of a quantum phase from classical rotation of a single spin," *Phys. Rev. Lett.* **124**(2), 020401 (2020).
398. B. Carmans et al., "OSCAR-QUBE: student made diamond based quantum magnetic field sensor for space applications," in *4th Symp. Space Educ. Activities*, Universitat Politècnica de Catalunya (2022).

Kihwan Kim is a PhD candidate in the Department of Physics at Korea University in Seoul, Republic of Korea. He received his BS degree in physics from Korea University in 2019. His research focuses on developing hybrid quantum registers based on diamond NV centers and nuclear spins, as well as on quantum sensing, particularly NMR spectroscopy using NV centers.

Jong Sung Moon is currently a researcher at the Quantum Technology Research Division in Electronics and Telecommunications Research Institute. He received his PhD from the Department of Physics at Ulsan National Institute of Science and Technology in 2024. His current research interests include the design and fabrication of quantum photonic devices based on solid-state quantum emitters.

Dongkwon Lee is a PhD candidate in the Department of Physics at Korea University in Seoul, Republic of Korea. He received his BS degree in physics from Korea University in 2018. His research interests include nano-mechanics, diamond nanostructure fabrication, magnetic device fabrication, and the development of hybrid quantum systems using bosonic qubits and NV centers.

Jin Hee Lee received his PhD in physics from the Ulsan National Institute of Science and Technology (UNIST), Ulsan, Republic of Korea, in 2025. His current research focuses on GaN defect-based quantum emitters, particularly the realization of high-efficiency single-photon sources in the telecom band through optical coupling with hole circular Bragg gratings.

Yuhan Lee is a PhD candidate in the Department of Physics at Korea University in Seoul, Republic of Korea. He received his BS degree in physics from Korea University in 2019. His research focuses on scanning magnetometry based on diamond NV centers and its application to the investigation of magnetic phenomena in nanoscale transport devices, 2D magnetic materials, spin textures, and spintronic systems.

Chanhu Park is a PhD candidate in the Department of Physics at Korea University in Seoul, Republic of Korea. He earned his BS in physics from Korea University in 2020. His research interests include magnetometry using NV ensembles in diamond, the development of practical devices based on NV ensembles, and the coupling of solid-state spin qubits to microwave cavities.

Jugyeong Chung is a PhD candidate in the Department of Physics at Korea University in Seoul, Republic of Korea. He received his BS degree in physics from Korea University in 2021. His research focuses on magnetometry using wide-field microscopy based on diamond NV centers, with applications including the investigation of magnetic phenomena in biologically derived magnetic materials and the imaging of current flow and magnetic structures in solid-state devices.

Donghun Lee is a professor in the Department of Physics at Korea University in Seoul, Republic of Korea. He received his PhD in physics from yhe Ohio State University in 2010. His research focuses on quantum sensing and imaging based on nitrogen-vacancy centers in diamond. He is a recipient of the Outstanding Young Researcher Award from the Association of Korean Physicists in America (2015) and the Minister of Science and ICT Award in Quantum Information Science from the Korean government (2023).

Je-Hyung Kim received his PhD in physics at the Korea Advanced Institute of Science and Technology (KAIST) in 2014. He was a postdoc researcher at the University of Maryland from 2014 to 2017. Since 2017, he has joined the Department of Physics at the UNIST, Republic of Korea, and is now an associate professor at UNIST. Major research topics of his group are fundamental studies of quantum light–matter interactions, advancing quantum photonic/spin devices, and their applications to quantum information science.